University of Glasgow

Hamilton, Alexander Andrew William (2023) *Analysis of adhesive joints with mechanically interlocking microstructured adherends.* PhD thesis.

http://theses.gla.ac.uk/83423/

Copyright and moral rights for this work are retained by the author

A copy can be downloaded for personal non-commercial research or study, without prior permission or charge

This work cannot be reproduced or quoted extensively from without first obtaining permission in writing from the author

The content must not be changed in any way or sold commercially in any format or medium without the formal permission of the author

When referring to this work, full bibliographic details including the author, title, awarding institution and date of the thesis must be given

Enlighten: Theses
https://theses.gla.ac.uk/
research-enlighten@glasgow.ac.uk

Analysis of Adhesive Joints with Mechanically Interlocking Microstructured Adherends

Alexander Andrew William Hamilton

A thesis submitted to the James Watt School of Engineering at the University of Glasgow in partial fulfilment of the requirements for the Degree of Doctor of Philosophy

Contents

List of Figures

List of Tables

List of Publications

1. **Alex Hamilton**, Yang Xu, Mehmet E. Kartal, Shanmugam Kumar, Nikolaj Gadegaard and Daniel M. Mulvihill (2022) "Optimisation of Interlocking Microstructured Adhesive Joints via Finite Element Modelling, Design of Experiments and 3D Printing, *International Journal of Adhesion and Adhesives*, Under Review.

2. **Alex Hamilton**, Yang Xu, Mehmet E. Kartal, Nikolaj Gadegaard, Daniel M. Mulvihill, (2021) "Enhancing Strength and Toughness of Adhesive Joints via Micro-Structured Mechanical Interlocking", *International Journal of Adhesion and Adhesives,* 105, 102775.

3. **Alex Hamilton**, Jack Perris, Neil Convery, Daniel M. Mulvihill, Nikolaj Gadegaard (2021) "Flexible inserts for injection moulding of complex micro-structured polymer components", *Macromolecular Materials and Engineering,* Vol 306(6), 2100223.

4. Saad Bin Jaber, **Alex Hamilton**, Yang Xu, Mehmet E. Kartal, Nikolaj Gadegaard, Daniel M. Mulvihill, (2021) "Friction of flat and micropatterned interfaces with nanoscale roughness", *Tribology International, Vol.* 153, 153, 106563.

Author's declaration

I declare that all the work presented in this thesis has been carried out by me unless otherwise acknowledged or referred to.

Alexander Andrew William Hamilton, September 2021

Acknowledgements

Firstly, I would like to thank my supervisors Dr Daniel Mulvihill and Professor Nikolaj Gadegaard for the continued support, guidance and encouragement throughout my academic research. They have shown a great degree of patience and provided invaluable insight throughout my time at Glasgow University. Additionally I would like to thank Dr Yang Xu, Dr Mehmet Kartal and Dr Kumar Shanmugam for the valuable assistance and discussions.

I would like to express my thanks to several of my fellow post-graduate colleagues who I have worked alongside during my time at Glasgow University. There are too many to name in full, but specific acknowledgement should be given to Neil Convery, Jack Perris, Saad Bin Jaber, Stylianos Sarrigianidis, Andrew Greer and Jonathan Stormonth-Darling. I will forever be grateful for your knowledge and continued friendship. I would also like to express my thanks to the technical staff of the James Watt Nanofabrication Centre, for the constant support and help in guiding my initial experimental work. Without your help this project would never have been possible.

I would also like to thank my girlfriend, Kate Fell for her steadfast support, during several difficult times your help has always been appreciated. Finally, I would like to dedicate my work and this thesis to my parents. You have offered unwavering support, providing a platform to pursue any of my goals in life; any success I achieve is testament to the help you have given me along the way.

Abstract

Limited understanding of surface behaviour relative to bulk properties makes interfaces a point of notable uncertainty and weakness within engineering structures. Although previous research has touched on the notion of improving the mechanical performance of adhesive interfaces via surface patterning, there is significant scope for further exploration. Moderate success has been achieved using laser-based techniques to produce structuring, but this approach lacks control over surface geometry and pattern morphology. The key feature of this work stems from the fact that accurate geometries at the sub-millimetre scale have not really been explored for adhesive bonding applications. Using the James Watt Nanofabrication Centre (JWNC) at the University of Glasgow, novel adhesive joints having interlocking micron sized features have been developed and analysed.

Various micro-fabrication strategies were studied with a micro-imprinting/injection moulding protocol identified as the optimal strategy. A new route to the fabrication of micro-structured surfaces using injection moulding has been established by developing a flexible mould insert produced by adopting a nanoimprint process. The approach is rapid and more versatile. For example, Bosch process produced masters having sidewall scalloping can even be used as the flexibility of the mould insert permits ejection of the parts even with scalloping. Utilising this fabrication approach, polycarbonate single lap joints were tested in tension using a custom test rig. Results indicate that the presence of the micro-structured features enables load carrying via localised feature bending yielding substantially greater mechanical strength (95.9%) and work-to-failure (162%) compared to the unstructured (planar roughened) adhesive joint baseline, although it should be noted that this testing setup largely mitigated Mode I peel stresses during testing. Finite element (FE) modelling was used to demonstrate that most of the load carrying capacity originates from bending of the interlocked features (rather than from the adhesive). This result even opens up the possibility of adhesive-less joints (as long as the joint can be held together). A statistically guided optimisation protocol was then performed (using the FE model) to ascertain the optimal micro-feature geometries.

The final part of the work centred on determining the viability of 3D-printing micro-structured joints as a more economical and versatile manufacturing approach. Investigations into maximum printing resolution were conducted as well as mechanical tests to elucidate the implications of micro-structuring on printed joints. The main focus within this research was the ability to tailor bond-line compliance as a means to alter the stress distribution within the single lap joint, with results demonstrating that a more optimum combination of joint mechanical properties is possible by tailoring to place more compliant features near the edges of the joints. A final proof-of-concept study was performed using tensile butt joints as the joint configuration. Here, micro-structured interfaces

again enabled greater joint strength through providing greater active bonding area as well as providing more load carrying resistance via the stronger shear mode (via the feature sidewalls).

Chapter 1 : Introduction

1.1 Advances in materials engineering and the drive for innovation

When the various achievements within the field of engineering are reviewed, it is apparent that obtaining a fundamental understanding of the underlying physics leads to the opportunity to revolutionise the world. An early example of materials engineering can be attributed to the people of modern-day Iran around 8000BC. They identified and extracted copper from within rock formations and subsequently created ornaments and tools that would assist in farming. The invention of metal casting around 4000BC was another seminal feat of engineering, with the production of the first alloy, bronze following in 3000BC [1].

Moving into the modern history of materials engineering, there has been a plethora of discoveries and advancements. In the early 20th century, the focus was on metallurgical advancement and significant attention was focused on the austenite–martensite–cementite phases found in the iron–carbon phase diagram that underlies steel production [2]. The achievement of understanding how temperature affects the atomic structure in metals, is an example of the substantial knowledge that has been accrued on bulk material properties. Under the industrial pressures of World War II, there was a concerted move towards the study of polymers as a cost-effective route for mass production with injection moulding, improved by the work of James Watson Hendry becoming a viable manufacturing route. The success of this work was illustrated when plastic production overtook steel production in 1979 [3].

Through a brief review of engineering history, the knowledge of bulk material properties and the routes utilised for the optimisation of these properties becomes evident. However, the study and knowledge associated with material surfaces is less rigorously researched. Advancements in surface properties are realised through the means of chemical modification and/or the utilisation of surface coatings (such as physical vapour deposition (PVD) or chemical vapour deposition (CVD)), often enabling surfaces to possess greater wear resistance through increasing hardness [4].

When reviewing the methods to enhance mechanical performance, an area that has been largely unvisited is the physical geometry of the interface. Manufacturing methods such as machining and milling lead to surface profiles possessing rough and variable surface topography with limited understanding of the performance implications associated with the variation [5]. This is highly pertinent to bonding and tribological applications where the engineering surfaces are used as the

points of contact with other material. A summary of the random profiles generated from conventional manufacturing techniques relative to a tailored geometry is given in Fig. 1-1.

It is hypothesised that the development of consistently structured interfaces with the critical dimensions on the micron scale (10-500 µm) will be of great benefit to the surface engineering community, with greater repeatability and tuneable frictional properties possible for tribological applications [6]. Furthermore, it is hypothesised that adhesive bonding performance could be greatly enhanced via the presence of repeating micro-structured features.

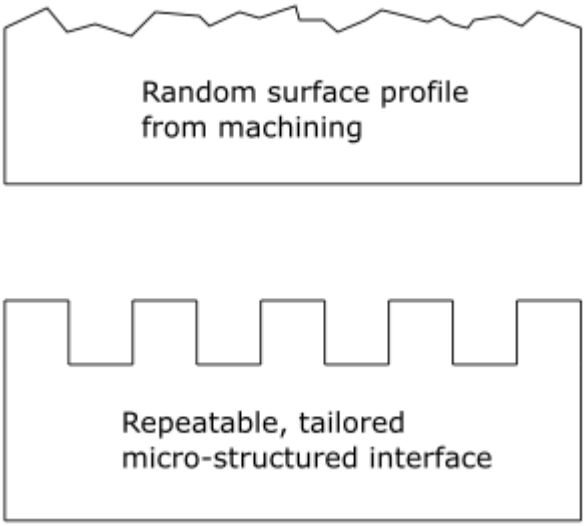

Figure 1-1: Schematic illustrating the differing micro-topographies associated with conventional machining (a) and a repeatable micro-structured interface (b) produced via cleanroom processing.

1.2: Surface structuring in nature

1.2.1 Structuring for hydrophobicity

Using nature as a motivational starting point, it becomes apparent that surface structuring can have a profound effect on material behaviour. An interesting example of the presence of nano-structuring in nature is the compound eyes of moths and butterflies, where nanometre structuring can interact with incident light such that they reduce the proportion reflected and enhance the proportion absorbed [7,8]. The presence of this feature is a protective measure, reducing visibility to predators whilst improving vision. This feature has served as motivation for the development of devices such as solar panels. One of the most commonly studied examples of surface structuring is the water repellent lotus

leaf. It was discovered that microscale mounds and nanoscale hairs on the surface of the lotus leaf result in a highly hydrophobic surface, an image of this is given in Fig.1-2 [9]. The hydrophobicity produced enables water to evacuate the leaf surface whilst simultaneously carrying away dirt [10].

This hydrophobic nature is quantified through the angle formed between a water droplet and the surface of interest. Large water contact angles illustrate high hydrophobicity, as the physical contact area of the water droplet decreases. Another example of non-adhesive surfaces is present on the skin of sharks, where water repulsion is a means of reducing drag whilst providing anti-fouling capabilities stopping the aggregation of harmful microbial species [11,12].

Figure 1-2: Water repulsion is realised on the lotus leaf due to micron scale mounds and nanoscale hairs on the surface, image from [9].

1.2.2: Structuring for adhesion, gecko feet

Through observing the movements of a Gecko, it is fascinating to observe the abilities to adhere to smooth surfaces, overcoming the forces of gravity. This innate ability stems from the highly developed surface structuring on the Gecko's foot. On the gecko's foot, hundreds of thousands of long hairs, known as setae form the large-scale unit of adhesive capability, with a size ranging from 30-130 µm. From these setae emanate hundreds of submicron structures known as spatulae. Fig.1-3 provides Scanning electron micrographs (SEMs) of setae and spatulae, respectively.

The exceptional levels of adhesion are thought to be achieved through a combination of mechanical interlocking at the interface, capillary forces and Van der Waal's intermolecular forces rather than

through a purely chemical avenue [13]. This seminal example illustrates the fundamental function of surface structuring as well as its potent impact on real-world physical properties. This work has served as inspiration for 'dry' adhesion-based research [14].

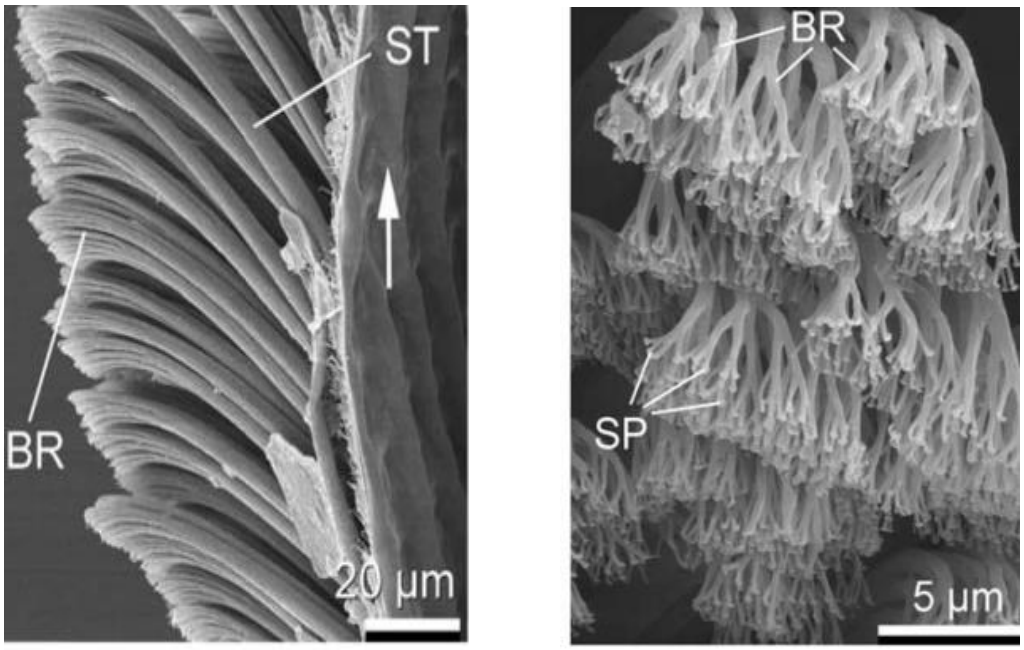

Figure 1-3: Scanning Electron Micrographs of Gecko foot structuring: larger setae (left); branches from setae and sub-micron sized spatulae (right), image from, image from [14]

1.3: Adhesive bonding as a joining method

1.3.1 Advantages and limitations of adhesive bonding

Adhesive joints have become increasingly prominent within modern engineering designs. Several decades ago, joining operations between materials was achieved predominantly through the mechanical fastening of bolts and pins, with adhesive bonding emerging in the early 20th century. Modern advancements in adhesive technology have enabled significant increase in the viability of adhesive joining as a replacement technology. Advantages of adhesive bonding include effective bonding of dissimilar materials, lightweight joints with no surface machining required and the absence of stress concentrations associated with the machining holes for pins [15]: this is particularly an advantage for economical assembly of parts. Adhesive joints have been used extensively in both the

automotive industry and the aerospace industry on account of the potential for lighter weight vehicles, fuel savings, and reduced carbon dioxide emissions [16, 17].

Although adhesive bonding has been successful in numerous applications, there are some notable drawbacks as an approach for joining materials. The use of adhesive bonding has been hampered by a lack of standardisation with regard to optimal bonding protocols as well as reduced knowledge on the strength of joints and their failure modes. Furthermore, the need for disassembly in engineering structures has posed limitations on the use of adhesive bonding [18]. The simplest configuration for an adhesive joint is illustrated in Fig. 1-4, this is known as the single lap joint (SLJ). The SLJ comprises of two solid components known as adherends bonded via an adhesive that enables load transmission. Although the single lap joint is a simple physical configuration, a highly complex stress state exists within the joint.

Ideally, when considering an adhesive joint subjected to a tensile load, the stress should be distributed evenly across the adhesive layer. However, this does not occur and high stresses generally occur at the edges of the overlap area. The high stresses experienced at the edge of the adhesive layer are a major factor that must be considered during the design and manufacture stage [19]. Although the SLJ is the most common in engineering applications, there are several other lap joint configurations used. When manufacturing adhesive joints, several factors must be considered to ensure that satisfactory strength is achieved at the joint interface, separated into material and geometric factors [20].

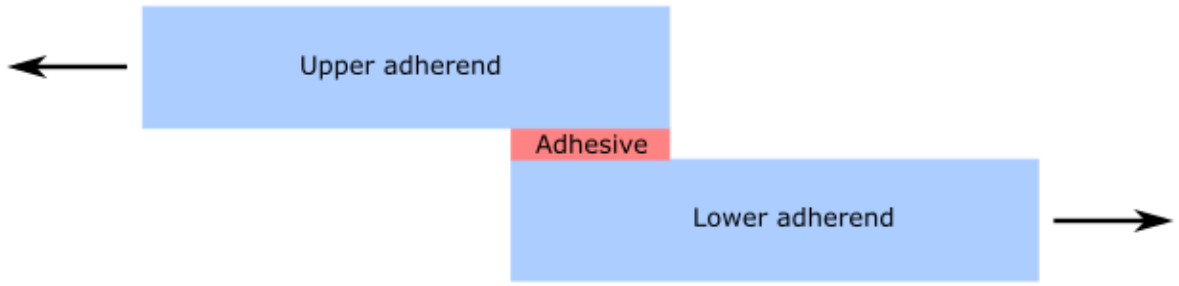

Figure 1-4: Single lap joint (SLJ) showing the adherend and adhesive components

1.4: Motivation for research

Reflecting on the use of adhesively bonded joints within engineering, it is apparent that the key advantages associated with versatility and light weight, efficient design are often outweighed by the lack of confidence in the mechanical performance, with varying failure modes and failure loads impacting on the confidence for use in high-end engineering applications. The high peak stresses at the outer edges of the joint can be seen as major risk locations for crack initiation with catastrophic

failure of joints less predictable than typical mechanically fastened alternatives especially under impact conditions.

The present research has been inspired by nature, whereby the use of micro-structuring and repeatable patterning of the adherend interfaces has been hypothesised to increase the overall repeatability of mechanical performance, through effectively standardising the bond thickness whilst introducing an additional means to transmit force (localised compressive forces at each discrete contact point) throughout the bond-line. Furthermore, the introduction of repeatable, square-wave features will appreciably enhance the available bonding surface area, with the potential to provide additional load-bearing capacity through modifying the peak stresses at the edges of the bond-line.

Chapter 2 : Adhesive Joint theory

This chapter covers the main principle underpinning adhesive joint theory, including the theories of adhesion, typical bonding preparation techniques to enhance adhesion strength and performance as well as exploring the unique stress-state within the single lap joint and the various analysis methodologies used to guide design.

2.1. Adhesive joints: Bonding theory and common preparation techniques

A key concept to consider when studying adhesive bonding is the phenomena of adhesion and the fundamental principles underpinning adhesive mechanisms. Adhesion is a complex physiochemical process whereby the interface between the two distinct materials is brought into intimate contact, whereby attractive forces lead to the formation of the adhesive bond. The relative adhesive strength is dependent on the following parameters:

- Mechanical properties of the interface
- Chemical bonding interactions at the interface
- Wettability and coverage of the adhesive layer

The mechanical properties of the interface pertains to the overall morphology of the surfaces, with high degree of porosity and roughened surfaces providing a greater active bonding area and potential for interlocking of adhesive at micro-voids at the bond-line. The chemical bonding refers to the type of chemical bonds that are active at the interface. With reference to polymeric bonding, covalent bonding (whereby two atoms share a set electrons) can be considered the strongest attraction force occurring between the adherend and adhesive material, with secondary forces such as Van der Waal's interactions the primary means of chemical bonding in less strong bonds.

The concept of wettability refers to the ability for the adhesive material to suitably cover the adherend surface. During the process of forming a surface, it is necessary for a material to break some molecular bonds within the bulk of the material to enable the formation of the surface. Hence, surface energy is defined as the excess energy at the surface of a material (energy used to break the bonds and form the surface) compared with the bulk material itself. Surfaces that have predominately carbon-hydrogen bonds tend to have low surface energies and so do not wet easily. Surfaces that have lots of oxygen and hydrogen bonds have inherently greater surface energies and therefore improved adhesion performance. Examples of low energy surface materials are Polyethylene and polypropylene. A metric to test wettability can be considered the wetting angle between the two

materials, with a low contact angle represent high coverage, higher contact angles represent a scenario where the material does not suitably spread across the adherend surface leading to poor adhesion strength.

When considering an adhesively bonded joint, there are two principle mechanisms at play. Adhesion refers to the adherence of the adhesive to the adherends, whereas cohesion refers to the inner strength of the adhesive. A key factor regarding adhesion optimisation is the use of appropriate pre-processing to ensure that weak boundary layers on the adherend surfaces are removed prior to adhesive application. To ensure intimate molecular contact at the interface, different approaches can be utilised [21]. A degreasing step is commonly used prior to most bonding applications. This is achieved using organic solvents such as acetone to remove organic matter such as grease, oil and wax from the surfaces of the adherends. Another common approach to physically change the surface of the adherend is via surface roughening. In this technique, abrasive materials are utilised to remove layers and generate a roughened surface texture. The benefits of this method are two-fold: weak boundary layers can be eradicated as well as increasing the active surface area available for bonding.

A prevalent technique utilised to roughen bonding surfaces for metals is the grit blasting process. This process entails the employment of hard grit particles, propelled under the action of compressed air onto the target surfaces, leading to the removal of material at the surface. The benefits of this technique are two-fold: weak boundary layers can be removed and a random micro-structure can be imparted onto the interface. Sample roughness can be measured using stylus profilometry, with different grit blast media used to tailor the degree and form of material removal. Factors effecting the final form include the hardness of the grit (hardness needs to be greater than the sample) as well as the density (density is proportional to the energy imparted at the sample surface).

Focussing on the pre-treatment options for plastics, it can be observed that chemical modification of the bonding surface is the main approach to enhance performance. The use of chemical treatments can also be used, whereby the adherends can be immersed in solution, enabling the etching away of the adherend surface or modification of the surface making it more chemically active. An electrochemical reaction can also be included where current is transferred. Examples of this approach include acid etching and anodising.

Another group of treatments can rely on surface modification through exposure to excited charges or species to increase the surface energy of the adherends; an example of this approach is corona discharge [22]. Corona is a stream of charged particles i.e. electrons and neutrons, accelerated under the stimulus of an electric field. A corona is produced when a gap filled with air and other gases is exposed to high voltages, emanating from an electrode tip, leading to a chain reaction of high velocity

particle collisions resulting in the production of more ions. The corona treatment process leads to the oxidation of the sample, with an increase in OH and COOH groups at the surface resulting in an increase in surface energy [23]. Examples of polymer materials with bond strength improvements include poly-propylene, polycarbonate and poly-ether ether ketone (PEEK), although bond strength is still relatively low compared to metals [24-26]. Another prominent technique to enhance bond performance is the flame treatment process. This technique is particularly advantageous for the processing of non-uniform shapes. The process can be summarised as a burning process, where the polymer is subjected to an oxidizing flame.

2.2: Failure modes for adhesive joints

As mentioned as a potential detraction from the usage of adhesive joints, several failure modes exist; these are outlined in Fig. 2-1. Adhesive failure is commonly observed as the limiting strength emanating from the interface, leading to the detachment of adhesive and adherend seen in Fig.2-1a. This is widely considered a sub-optimal bond. In contrast, the cohesive failure depicted in FIg.2-1b. illustrates the scenario where bulk properties of the adhesive fail prior to the interface, leading to an improved performance, a variant of this is shown in Fig.2-1c where a thin layer cohesive failure occurs. Accounting for the various failure modes possible for the single lap joint, it becomes apparent that appropriate joint design, material selection and surface preparation are of paramount importance [27].

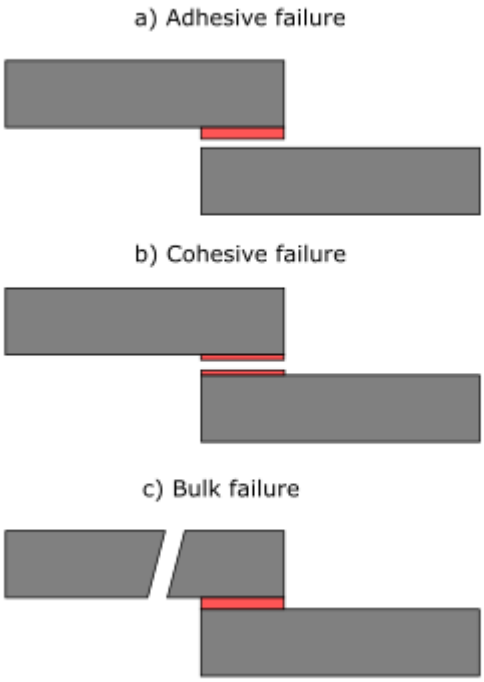

Figure 2-1: Schematic showing the various failure modes possible for the single lap joint. Adhesive-based failure occurs when the interfacial bond strength is weaker than the adhesive (a), cohesive-based failure occurs when the bond strength exceeds the adhesive strength (b); this mechanism is viewed as the optimal failure pathway. Bulk failure can occur when adhered strength is lower than the adhesive strength (c); this mechanism typically emanates due to eccentric bending of the single lap joint.

2.3: Fracture mechanics overview

2.3.1: Griffith's energy-based fracture criterion

A pertinent area to address is the concept of crack propagation within an adhesive joint; this is commonly enabled via the use of fracture mechanics theory. The energy based-fracture approach formulated by Griffith [28] is a useful concept. In this approach, the energy required to break atomic bonds, and in turn, material at a crack front is balanced via the energy released during the process. A simple illustration of the energy required to break atomic bonds as well as the associated equation (Eq 2.1) are given in Fig. 2-2 [29].

The figure shows a crack that has grown to a finite length, '*a*' within a structure with thickness, '*B*'. To enable this, energy has been used to break down atomic bonds. The term ϒ refers to the amount of energy required to break the atomic bonds per unit surface area created by the crack. The schematic

in Fig 2-2 shows that there are two free surfaces, highlighting the need to multiply the energy equation by a factor of 2.

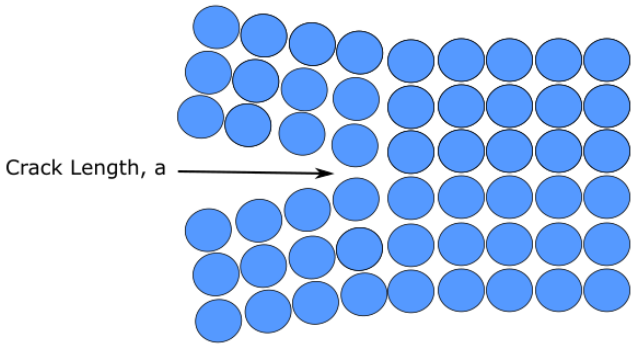

Figure 2-2: Schematic highlighting the crack propagation mechanism underpinning the energy-based theory of Griffith. The crack length 'a' represents the number of atomic bonds per unit length.

$$\text{Energy to break bonds} = 2\Upsilon aB \qquad \text{(Eq2.1)}$$

In addition to the energy input required to continuously drive crack growth, an additional term is required to compensate for the reduction in strain energy within the material as crack propagation progresses. The full equation (Eq 2.2) taking into account the two energy criteria is :

$$E_{total} = 2\Upsilon aB + \frac{\sigma^2}{2E}V - \frac{\sigma^2}{2E}B\pi a^2 \qquad \text{(Eq 2.2)}$$

Where the additional parameters of '*E*' (Young's modulus), 'σ' (applied stress) and '*V*' (material volume) are incorporated within the equation. This equation accounts for the strain energy present within the structure (second term) as well as the associated reduction in strain energy as a function of crack length, '*a*'. Due to the squared term a^2, it can be observed that the strain energy within the system becomes increasingly sensitive to the specific value for crack length. Small cracks are stable, requiring further input to increase crack length. However, once a critical crack length is achieved, the process accelerates, and catastrophic failure occurs across the crack front.

To determine the crack length at which spontaneous failure of the material will occur, the previous equation is differentiated with respect to the crack length. Setting the right-hand side of the equation to zero and using some simplification leads to the expression for the failure stress, σ_f as:

$$\sigma_f = \sqrt{\frac{G_c E}{\pi a}} \qquad \text{(Eq 2.3)}$$

In this expression, the term $G_c = 2\Upsilon$ is known as Griffith's critical energy release rate. Since this expression solely models crack growth due to the breaking of atomic bonds, this initial model described the crack propagation behaviour of brittle materials, largely underestimating the energy release for ductile materials such as metals. This expression was modified by Irwin and Orowan with the addition of a term for plastic deformation per unit surface area (G_p) for the energy release rate term (shown in Eq 2.4). This addition to the expression accounts for plastic flow at the crack tip providing a more representative value for ductile materials. When utilising these equations for brittle materials, the surface energy term dictates the response (a typical release rate for glass is approximately G=2 J/m^2), whereas ductile metals are governed via plastic dissipation (steel is around 1000 J/m^2).

$$G = 2\Upsilon + G_p \qquad \text{(Eq 2.4)}$$

The critical energy release rate can be calculated using the compliance method. An example of this can be found using the double cantilever beam (DCB) setup. The deflection of the two beams can be obtained using beam theory, as well as the energy release rate relation:

$$G = \frac{P^2}{2b}\frac{\partial \mathrm{c}}{\partial \mathrm{a}} \qquad \text{(Eq2.5)}$$

where P is the applied load, c is the compliance of the structure, and b is the plate thickness. For the DCB configuration, compliance can be expressed as:

$$c = \frac{2u}{P} \quad \text{(Eq2.6)}$$

Substituting in c $= \frac{Pa^3}{3EI}$, where *I* is the moment of inertia of the beam equating to $I = \frac{bh^3}{12}$. Using this relation within the original energy-based equation, results in the final form below:

$$G = \frac{12a^2}{Eh^3}\left(\frac{P}{b}\right)^2 \quad \text{(Eq2.7)}$$

2.3.2: Stress Intensity factor

Another useful parameter to define the stress state for various crack geometries is known as the stress intensity factor. The concept of stress intensity factors can be described through the examples of an elliptical hole under a far-field tensile stress. Under this loading the stress as a function of the horizontal distance from the crack tip can be defined as:

$$\sigma_{yy} = \frac{\sigma_\infty}{\sqrt{1 - \left(\frac{a}{x}\right)^2}} \quad \text{(Eq2.8)}$$

Where $'\sigma_\infty'$ is the far—field tensile stress, 'a' is the crack length value and 'x' refers to the horizontal distance along the crack plane; This realtionship is highlighted within Fig 2.3 for reference. There exists an asymptote within this stress distribution, when *x* = *a*, representing the tip of the crack front. This work was developed further by Irwin, where a formula was constructed to determine the stress-state more easily for different angles relative to the crack. The equations for normal stresses in the *x* and *y* directions, as well as the shear stress are given below. This derivation also enabled the formulation of the stress intensity factor, *K*, an important parameter in fracture mechanics.

$$\sigma_{xx} = \frac{\sigma_\infty\sqrt{\pi a}}{\sqrt{2\pi r}} cos\frac{\theta}{2}(1 - sin\frac{\theta}{2}sin\frac{3\theta}{2}) \quad \text{(Eq2.9)}$$

$$\sigma_{yy}=\frac{\sigma_\infty\sqrt{\pi a}}{\sqrt{2\pi r}}cos\frac{\theta}{2}(1+sin\frac{\theta}{2}sin\frac{3\theta}{2}) \quad \text{(Eq2.10)}$$

$$\tau_{xy}=\frac{\sigma_\infty\sqrt{\pi a}}{\sqrt{2\pi r}}cos\frac{\theta}{2}sin\frac{\theta}{2}cos\frac{3\theta}{2} \quad \text{(Eq2.11)}$$

$$K=\sigma_\infty\sqrt{\pi a} \quad \text{(Eq2.12)}$$

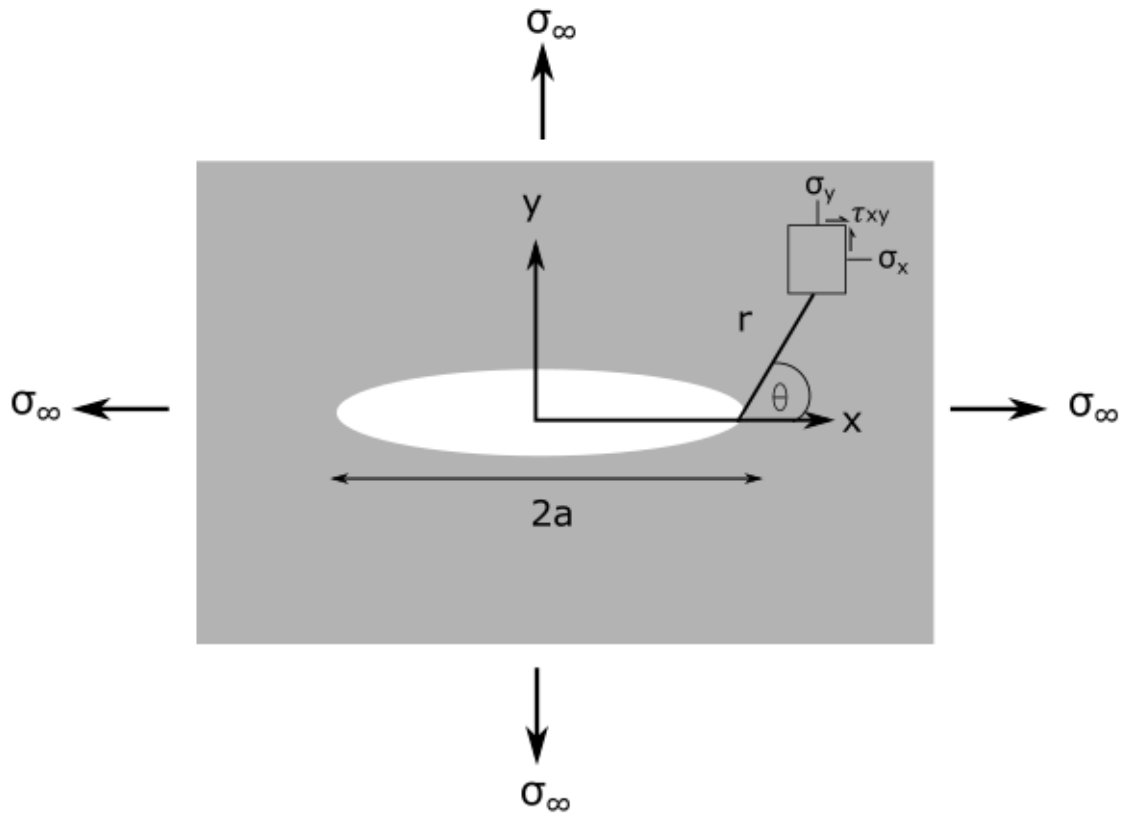

Figure 2-3: Schematic illustrating the bi-axil stress state for an elliptical hole subjected to fair-field tensile stresses in the x and y planes

Within all three stress equations, the term $\sigma_\infty\sqrt{\pi a}$ is termed the stress intensity factor. The unique quality of this parameter is that the value of the stress intensity factor entirely captures the severity of stress state at the crack front. It is worth noting that there exists a relationship between the stress intensity factor and the critical energy release rate. The relationship between critical energy release rate and failure stress can be written as:

$$G_c = \frac{\sigma_f^2 \pi a}{E} \quad \text{(Eq2.13)}$$

Using the stress intensity relation, this expression can be re-written as:

$$G_c = \frac{K_c^2}{E} \quad \text{(Eq2.14)}$$

2.3.3: Crack opening modes

There are three distinct opening mechanisms that can be used to describe crack opening behaviour within structures; a summary schematic is provided in Fig. 2-4. Mode I loading is the most common variant, with crack propagation occurring through tensile loading at the crack front, typically any crack will have a tendency to develop into this form through progressive loading. Mode II is of secondary importance and occurs through in-plane shearing. Mode III loading is a tearing-based mechanism that is typically less common than the other forms [30].

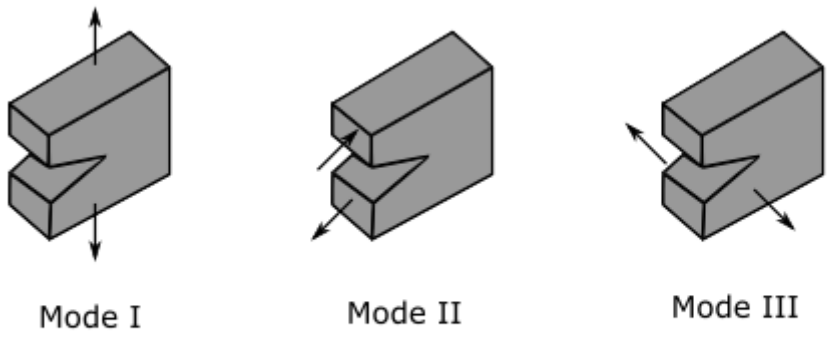

Figure 2-4: Schematic highlighting the crack opening modes. Mode I loading describes a tensile loading scenario; Mode II shows in-plane shearing with Mode III loading occurring via tearing.

2.4: Adhesive joint stress distribution (SLJ)

Within an adhesive joint, there is typically an uneven distribution of stress, with high stresses observed at the edges of the adhesive layer. This section serves to review key analytical expressions for the single lap joint to highlight the importance of the stress distribution.

2.4.1 Average stress equation

The simplest analysis describing shear behaviour in a SLJ considers constant shear stress across the overlap length. This model assumes that the adherends are rigid and the adhesive deforms solely by shear. The shear stress, τ relationship is realised through:

$$\tau = \frac{P}{lb} \qquad \text{(Eq2.15)}$$

Where *P* is the applied load, *b* is the joint width and *l* is the overlap length. Although this equation is unsatisfactory and not an accurate representative of the true stress state, it is frequently used for quoting shear strength values in ISO and ASTM standards [31].

2.4.2 Volkersen shear lag model

Early work aimed at explaining the stress-strain behaviour was conducted by Volkersen in 1938 [32]. Moving away from the concept of uniform stress within the joint, he postulated that the bonded area of the joint experienced differential shear stress in the plane parallel to the load; this was termed the shear lag theory. It was assumed that the adhesive deformed solely by shear and the adherends deformed exclusively through tension.

This theory is visualised in Fig. 2-5, with stress in the upper adherend maximal at the start of the adhesive bond (Point 1) and zero at the free surface (Point 2). Conversely, the bottom adherend experiences a maximal stress at (Point 1'), progressively decreasing to zero at the free surface (Point 2'). The equations representing the shear stress distribution across the overlap length are given below.

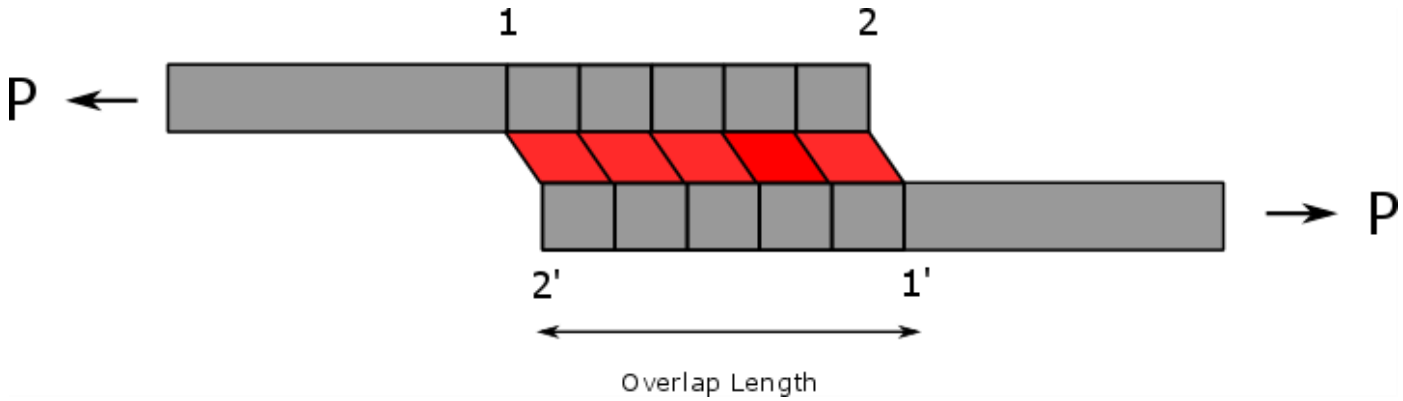

Figure 2-5: Schematic of the differential straining theory from Volkersen [32] in a SLJ. Points 1 and 2 refer to the outer edges of the upper adherend. Points 1' and 2' refer to the outer regions of the lower adherend.

$$\tau(x) = \frac{Pw}{2bl}\left[\frac{\cosh(wx)}{(\sinh(0.5w))} + \frac{(\gamma-1)}{(\gamma+1)} * \frac{wsinh(wx)}{2\cosh(0.5w)}\right] \quad \text{(Eq2.16)}$$

$$w^2 = (1+\gamma)\varphi \quad \text{(Eq2.17)}$$

$$\gamma = \frac{t_t}{t_b} \quad \text{(Eq2.18)}$$

$$\varphi = \frac{G_a l^2}{E t_t t_b} \quad \text{(Eq2.19)}$$

Where *P* is the applied load, *b* is the joint width, *l* is the overlap length, *x* is position along the joint length, t_t is the thickness of the upper adherend, t_b is the thickness of the lower adherend, G_a is the shear modulus of the adhesive and *E* is the Young's modulus [33]. The limitation of this model is the failure to account for the bending moment induced in the joint due to the eccentricity of the load profile. The first approach that factored in the eccentric load path was developed by Goland and Reissner [34]. In this work, the eccentric loading path that induces a bending moment was accounted for in the solution through the incorporation of bending moment factors [34]. The bending moment induced within a SLJ when subjected to a tensile load is depicted in Fig. 2-6.

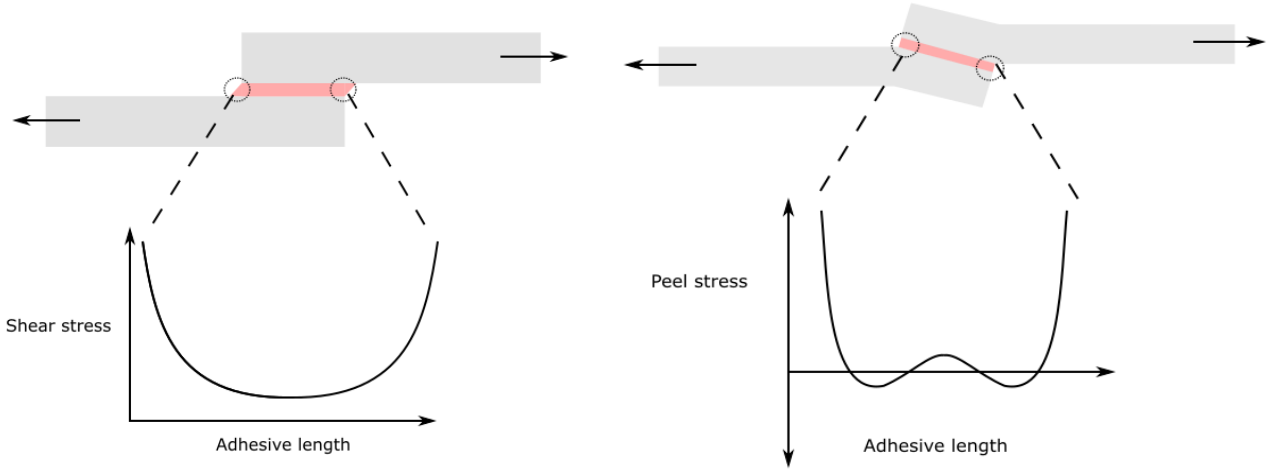

Figure 2-6: Illustration of the bending moment induced within adherends, due to the eccentric loading profile, the adherends deform to align the load path through the joint. A highly uneven distribution of normal forces is transmitted through the adhesive layer.

2.4.3 Bending moment theory

Goland and Reissner [34] proposed that, as the adherends are increasingly strained, the bending moment is continually reduced as the load path becomes increasingly aligned. To address this, they used a bending moment factor, *k* and a transverse force factor *k*' that enables a relation between applied tensile load per unit width (*P*'), the bending moment (*M*) and the transverse force (*V*) at the overlap regions of the joint. These relations are:

$$M = \frac{kP't}{2} \qquad \text{(Eq2.20)}$$

$$V = \frac{k'P't}{c} \quad \text{(Eq2.21)}$$

As the joint continually rotates based on an applied load *P*, the factors *k* and *k*' decrease. The derived expression for the factors *k* and *k*', are given below as well as the equation deriving the parameters u_2 and β; the final equation for stress distribution is given.

$$k = \frac{\cosh(u_2 c)}{\cosh(u_2 c) + 2\sqrt{2}\sinh(u_2 c)} \quad \text{(Eq2.22)}$$

$$k' = \frac{kc}{t} sqrt(3(1-\nu^2)\frac{P'}{tE}) \quad \text{(Eq2.23)}$$

$$u_2 = \sqrt{\frac{3(1-\upsilon^2)}{2}} * \frac{1}{t} * \sqrt{\frac{P'}{tE}} \quad \text{(Eq2.24)}$$

$$\beta^2 = 8\frac{G_a}{E}\frac{t}{t_a} \quad \text{(Eq2.25)}$$

$$\tau(x) = \frac{1}{8}\frac{P'}{c}[\frac{\beta c}{t}(1+3k)(\frac{\cosh\left(\frac{\beta c}{t}\right)\left(\frac{x}{c}\right)}{\sinh\left(\frac{\beta c}{t}\right) + 3(1-3k)}) \quad \text{(Eq2.26)}$$

Where *P*' is the tensile load per unit width, *c* is half the overlap length, *t* is the adherend thickness and ν is the Poisson's ratio [33]. The peel stress equation as well as the required parameters are given below.

$$\sigma(x) = \frac{1}{\Delta}\frac{P't}{c^2}\Big[(R_2\lambda^2\frac{k}{2} + \lambda k' \cosh(\lambda)\cos(\lambda))\cosh(\frac{\lambda x}{c})\cos(\frac{\lambda x}{c}) + (R_1\lambda^2\frac{k}{2} + \lambda k' \sinh(\lambda)\sin(\lambda))\sinh(\frac{\lambda x}{c})\sin(\frac{\lambda x}{c})\Big] \quad \text{(Eq2.27)}$$

$$\lambda = \gamma\frac{c}{t} \quad \text{(Eq2.28)}$$

$$\gamma^4 = 6\frac{E_a}{E}\frac{t}{t_a} \quad \text{(Eq2.29)}$$

$$R_1 = \cosh(\lambda)\sin(\lambda) + \sinh(\lambda)\cos(\lambda) \quad \text{(Eq2.30)}$$

$$R_2 = \sinh(\lambda)\cos(\lambda) - \cosh(\lambda)\sin(\lambda) \quad \text{(Eq2.31)}$$

$$\Delta = \frac{1}{2}(\sinh(2\lambda) + \sin(2\lambda)) \quad \text{(Eq2.32)}$$

Another seminal model is the Hart-Smith model to relate shear and peel stress distributions. In the analysis, the adhesive plasticity was incorporated into the solution with plastic deformation occurring at the edges of the joint with a central elastic region [35]. This analytical solution was not added to the stress distribution plot below owing to the similar predictions to the original Goland and Reissner peel stress equation.

2.4.4 Stress distribution plots based on analytical solutions

Based on the analytical expressions for stress provided above, the shear and peel stress distributions across the single lap joint were modelled. Representative graphs for the Goland and Reissner shear and peel stress relationships are given in Fig. 2-7 alongside the base-line value predicted via the average stress equation**.** The parameters utilised for the simulation were intended to illustrate the general stress distributions predicted for a steel-epoxy lap joint. The geometric and material parameters used are provided in Table 2-1.

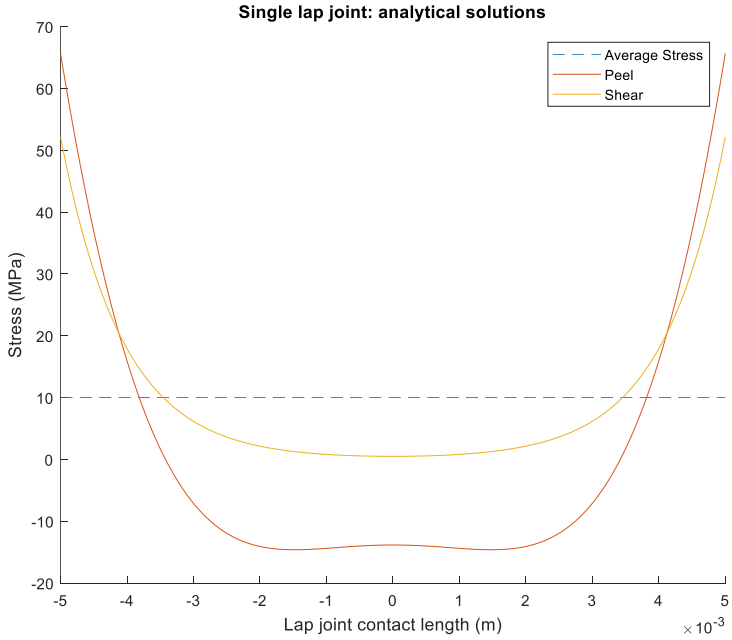

Figure 2-7: Shear stress distribution across lap joint width for the average shear equation, Volkersen shear model and Goland and Reissner peel stress distribution. Simulation plots from MATLAB model.

Table 2-1: Summary of the main material and geometric parameters used for the analytical simulations shown in Fig.2-7

Lap joint length (mm)	50
Lap joint width (mm)	10
Lap joint height (mm)	5
Contact area (mm^2)	10
Adherend stiffness (GPa)	210
Adhesive stiffness (GPa)	3
Adhesive thickness (µm)	10

It was observed that the peak peel stress values obtained from the analytical expressions are slightly higher than the peak stresses for the shear stress distribution. This scenario is common within the single lap joint, resulting in failure commonly being governed by the peak peel stress values. The average value of 20 MPa is a poor predictor of the stress state with this value under predicting the true stress state at the edges of the bond-line by more than a factor of 5. Ultimately, although analytical solutions provide good insight into the stress distribution within the single lap joint, numerical-based modelling offers greater flexibility in studying the single lap joint behaviour.

2.5.Numerical Modelling of Adhesive Joints

2.5.1 Finite element modelling for stress analysis

A major drawback of the analytical models developed for adhesive bonding is that each model requires a significant number of assumptions to enable a solution. Finite element modelling (FEM) has emerged as a more attractive approach to modelling bonded structures. At the basic level, FEM divides a mechanical structure into smaller sub-sections consisting of elements and connecting nodes to solve for a 'field quantity' (in the case of stress analysis, the displacement field or the stress field). For each element, the field quantity is interpolated from the nodal values and since elements are interconnected the field quantity can be determined across the entire structure.

As discussed, the stress state within the single lap joint is non-linear and complex, this makes the modelling process non-trivial, where obtaining a converged solution becomes difficult. In many scenarios, a suitable approach used to gain insight into the mechanical performance of bonded joints is to perform an elastic analysis to gauge the stress state and assist in optimising real-life performance. For situations where failure and progressive damage of the joint has to be studied, the implementations of cohesive zone modelling has become the modern method of analysis [36].

2.5.2 Cohesive zone modelling

The intention of cohesive zone modelling (CZM) is to relate the displacement or separation of two points of commonality between the adherends to the force per unit of area, termed the traction. Cohesive elements can be used to model an exceptionally thin region between the two bulk materials, in this case representing an adhesive layer. The cohesive elements act to constrain the two adherends together transmitting loads until the force and displacement cause damage leading to failure. The

major advantage of using CZMs relative to traditional fracture mechanics based approaches, is the ability to model damage development within a structure without the initial presence of a crack [37].

The traction-separation law governs the behaviour between the adherends, providing the relationship between element separation and traction. The cohesive elements exhibit a reversible elastic response until a critical separation value, δ_o occurs. Above this threshold, damage and failure occurs if the fracture separation δ_f is reached. The area under the traction-separation law is equivalent to the fracture energy G_c. Additionally, the damage evolution within the cohesive elements require an appropriate model. The Mode I energy release rate is calculated through the use of double cantilever beam (DCB) opening tests and Mode II energy release rate is obtained through the use of end-notched-flexure tests or the thick adherend lap joint test.

The cohesive law obtained for an adhesive joint setup is equally dependent on the material properties of the adherends. Therefore, to find parity between experiment and simulation, sufficient material characterisation is required. Simulation of lap joints are covered in Chapter 6.

Chapter 3 : Literature Review

This section will discuss the fields of study that provide a benchmark for the study of a micro-structured interface.

3.1: Laser ablation

The process known as laser ablation has been an area of prominent research for establishing structured interfaces in bonding applications. The surfaces developed through laser ablation could be described as a more structured version of a grit-blasted sample, with greater repeatability of micron scale features. Bonding performance can be improved through three distinct mechanisms:

1. Increase in available surface area for bonding.
2. Mechanical interlocking of adhesive entrapped in pockets of removed substrate.
3. Chemical modification of surface during material removal such oxidation reactions increasing surface energy.

Work performed by Zhang et al, [38], introduced the concept of structuring adherend substrates through laser vaporisation. The intention behind this work was to enhance adhesive bonding between metal and ceramic substrates. SiN was chosen as the ceramic material and stainless steel was the selected metal. Using a KrF excimer laser under carefully chosen laser parameters, material was successfully ablated from SiN substrates forming a spherical micro-feature topography. Laser ablation did not prove successful in generating a structured topography on stainless steel substrates. Mechanical testing of Single lap joints (SLJs) illustrated a marked improvement in shear strength in laser ablated samples relative to untreated and abraded specimens.

This work was augmented by Baburaj et al. [39] in which laser ablation was used on titanium samples to form structures termed micro-columnar arrays (MCAs). The SLJ shear results corroborate the findings of Zhang et al. [38], with the MCAs resulting in an increase in shear strength. An optical microscope image of the titanium-epoxy interlocking features is provided in Fig.3-1.

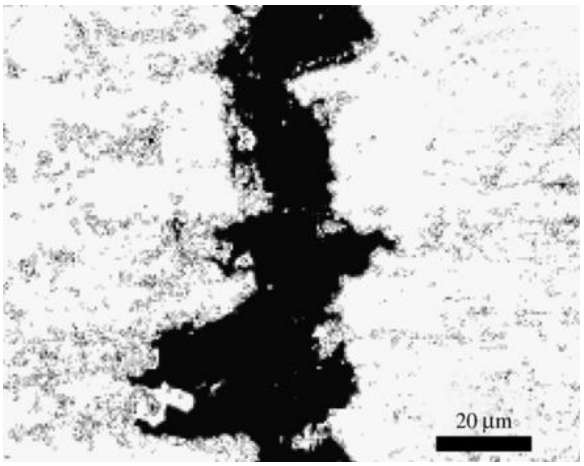

Figure 3-1: Optical micrograph of titanium-epoxy interface, image from Baburaj et al. [39]. The laser ablated titanium (white) has a highly dense microstructured interface enabling the epoxy (black) to penetrate recesses.

The use of laser ablation was bolstered through the results obtained by Alfano et al. [40] for aluminium and steel adherends. Using a Ytterbium excimer laser, the failure loads of both joint configurations increased, with a strength increase in excess of 100% for the aluminium bonded joints relative to those subjected solely to a degreasing pre-treatment. It was hypothesised that chemical modification at the interface during vaporisation resulted in the marked improvements. This result is shown in Fig.3-2.

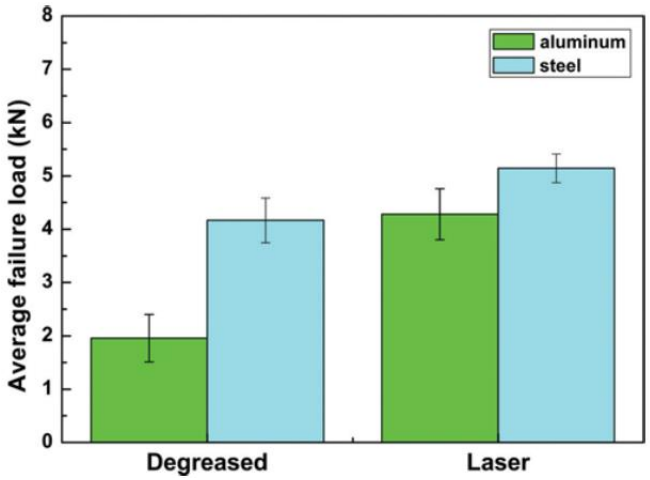

Figure 3-2: Average failure loads in kN for aluminium (green) and steel adherends (blue) with degreasing alone (left) and laser ablated (right). From Alfano et al. [21].

The strength and toughness in copper-to-epoxy joints tested in the T-peel test coupon were substantially increased by employing laser ablation in Hernandez et al. [41]. The improvement was attributed to chemical modification and mechanical interlocking of the structured surface with the adhesive promoting a cohesive failure in the adhesive layer. Work utilising laser based structuring of

stainless steel in tandem with injection moulding of a plastic to transmit the load was conducted by Byskov-Nielsen et al. [42] highlighting the potential to substantially increase mechanical strength via a micro-structured interface. Although laser ablation techniques illustrate the potential mechanical improvements attainable via imparting a mechanical micro-structure on adherends surfaces, this approach has notable limitations:

- The process is highly randomised with micro-features possessing a high degree of dimensional variation
- The main route of strength enhancement occurs via interlocking of the adhesive as opposed to physical interlocking of the discrete features.

Hence, it is useful to review the potential avenues to impart greater repeatability for structuring adherends surfaces for greater repeatability and the potential to introduce physical interlocking of square-wave features within the bond-line.

3.2: Repeatable patterning for feature interlocking

Outside of laser ablation, repeatable structuring is a field that remains open-ended with research still rather preliminary in nature. Work performed by Cordisco et al. [43] has compared the fracture performance of adhesively bonded aluminium with sinusoidal patterns relative to planar joints. This work involved the use of double cantilever beam (DCB) specimens, tested under Mode I crack opening conditions. Testing was performed in tandem with serial imaging of the crack front to enable the crack extension as well as the reaction force of the joint to be computed. To investigate the effect of patterning on mechanical response, different pattern aspect ratios were used ranging from 1:4 to 1:2. The crack extension/force curves as well an image of the test setup are given in Fig.3-3.

A notable feature of this work was the feature interlock between the sinusoidal units. As exemplified through laser ablation examples, traditionally the concept of mechanical interlocking refers to an interlock between adhesive and adherend rather than an interaction between the adherend features.

A limitation in this work was the millimetre scale used for patterning, with the sinusoidal pattern created through hot wire electrical discharge machining (WEDM), a process lacking the potential for micrometre scale work. Alternative processes enabling smaller scale features would prove desirable to amplify the material improvements further.

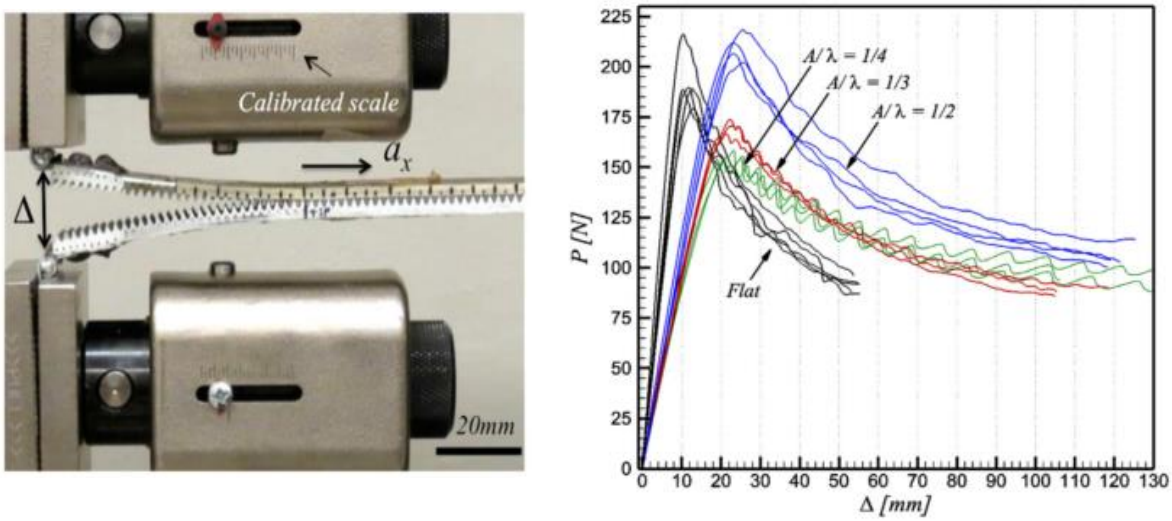

Figure 3-3: (left) Image of Mode I testing of sinusoidal DCBs performed by Cordisco et al. [40]; (right) crack extension/reaction force graphs for sinusoidal patterned Aluminium with varying aspect ratios (A/λ) versus flat adhesive joints.

Another example of an interlocked bonded structure is seen in Maloney and Fleck [44]. Maximum peak load was found to increase with aspect ratio (amplitude/wavelength) and crack propagation was delayed (compared to flat surfaces) under Mode I loading owing to the more torturous crack path. Interlocking square wave features for DCB and butt joint setups have shown strength and toughness improvements due to their introduction of a mixed-mode response which incorporates the stronger shear mode into both joint types. Again, the feature sizes used were on the order of 13 – 50 mm, higher than the intended magnitudes of the present study [45]. Finite element work by Corbett et al. [46] predicted up to 86.5% improvement in work to failure for a SLJ setup composed of a male and female adherend interlocking in shear. Follow-on experimental work looking at optimising the geometry of a single (mm sized) interlocking feature recorded work to failure improvements of up to 542% [47]. Haghpanah et al. [48] used teeth profiles in steel to show patterning can dramatically modify the failure mechanism of the joint following an initial fracture, leading to substantial changes in joint strength and toughness. Steel adherends were machined into three distinct geometries: planar samples, samples starting with a positive tooth and samples starting with a negative tooth. These specimens are illustrated in Fig.3-4. It was observed that the 'positive' sample reached a failure load 12% greater than the flat sample. The 'negative' sample fractured at a much lower load, although this initial fracture is arrested within the teeth leading to further loading and a substantial work-to-failure; attributed to localised plastic deformation within the adherends.

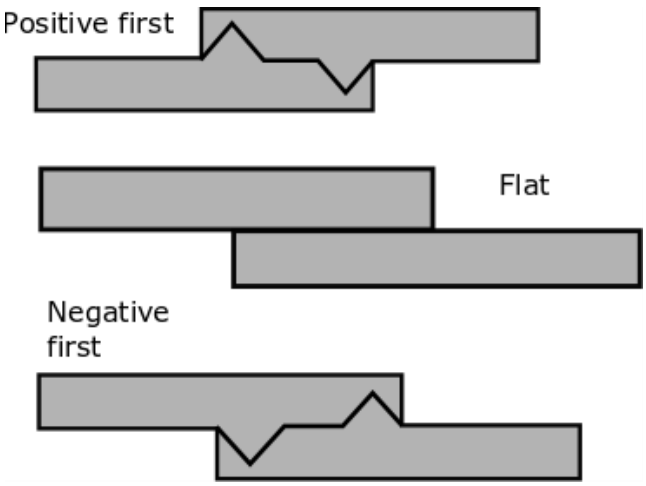

Figure 3-4: Steel joint geometries: Positive tooth first joint (top), flat joint (middle) and a negative tooth joint (bottom), adapted from Haghpanah et al. [45].

In addition to experimental findings, research performed by Reedy et al. [49] found that, for a nanoscale interlocking pattern, the interfacial toughness is directly proportional to the area of bonded contact. Although the study of feature patterns is in its infancy, the concept appears to hold credence as a method of adhesive joint enhancement. When reviewing the main experimental studies to introduce physical interlocking, the main limitation of this research is the millimetre length scales used for the features. A major issue with this approach is the significant design implications whereby notably large alterations to the bond-line geometry would be required relative to micro-features that would not significantly impact on the wider joint dimensions. Furthermore, it is hypothesised that the greater feature densities made possible by micro-fabrication routes would provide a means to increase joint toughness. Therefore, it is useful to review alternative manufacturing strategies to enable repeatable feature design at sub-millimetre length scales.

3.3: Pattern generation for adhesive interlocking

A final area of pertinent research centres on unique pattern generation methods for repeatable structuring. The research of Seock et al. [50] is particularly relevant to addressing micro-scale structuring. This work aimed to determine the effect of surface topography on joint fracture toughness through varying the geometries at the interface. To achieve periodic geometries, photolithography was used followed by isotropic wet etching. To achieve the micro-patterns, steel substrates were spin coated with SU-8 photoresist and exposed under a photomask. To achieve varying linewidths, features ranging from (10-90) µm were used. Following exposure, Nital solution was used to etch the exposed

steel. To create a composite joint, CFRP prepregs were laminated onto the surface and cured; a representation of the interface is given in Fig.3-5. Testing for Mode II and mixed mode failure illustrated that increasing the groove width relative to ridge width corresponded to an increase in toughness. This finding was attributed to greater energy dissipation during cohesive failure in the adhesive layer rather than in adhesion between the adherend and adhesive.

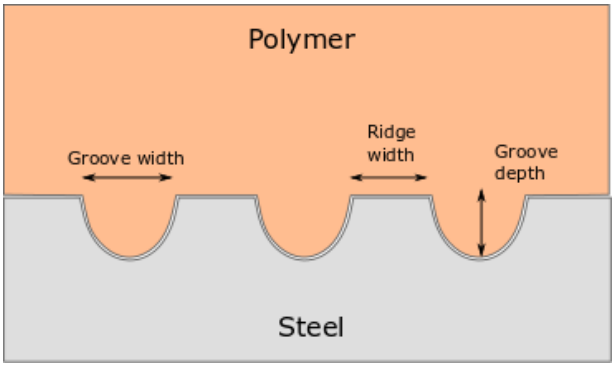

Figure 3-5: Schematic of steel/CFRP composite joint. The three dimensions outlined fully characterise the interface. Adapted from Seock et al. [50].

The use of imprint lithography has seen some use for patterning in adhesive bonding applications. Imprint lithography enables the transfer of patterns based on an initial master into thermoplastic polymers, if they are heated above the glass transition temperature. This technology enables features ranging from the micrometre scale to the nanometre scale. Work performed by Matsuzaki et al. [51] used lithography techniques and anisotropic etching of silicon to create teeth-like pyramidal profiles for bonding of butt joints. This work utilised the patterned silicon as a master to imprint microstructures into CFRP. Results illustrate that the joint strength increased from 1.17 MPa to 1.95 MPa due to the pyramidal structures. Further work by Hikosaka et al. [52] has demonstrated through crack opening tests, that the imprinting of periodic channels results in an increase in Mode I fracture toughness with enhanced performance with an increase in aspect ratio. This phenomenon was ascribed to three main mechanisms:

1. An increase in overall microscopic crack length
2. Increase in Mode II loading per unit area
3. Transition from interfacial failure to cohesive failure

Matsuzaki et al. [53] created a periodic groove pattern using a somewhat less studied material: Polypropylene. Polypropylene has limited adhesive capability due to a low surface energy; the rationale behind this work was to improve adhesive capabilities of polypropylene through adhesive

mechanical interlocking. Patterning was achieved through the process of roll-imprinting, in which the polypropylene was heated to its crystalline melting point and roll imprinting provided the transfer of pattern. An undercut angle was also used ranging from 0° to 35° based on previous studies that suggested purely vertical side walls resulted in more damage during separation from the master. An image of the structures created by roll imprinting is given in Fig.3-6a. Butt joint tests were performed with results illustrating the structuring yielded greater strength than planar polypropylene joints. These findings are seen through the stress-displacement graph in Fig. 3-6b. When reviewing these micro-scale manufacturing approaches, it is apparent that the repeatable structuring has not successfully enabled feature-to-feature interlock to be utilised, owing to the relatively low resolution limits of the manufacturing processes. It can be concluded that the rationale behind these approaches is akin to laser ablation-based techniques, relying on adhesive interlocking as opposed to adherend-to-adherend interlocking.

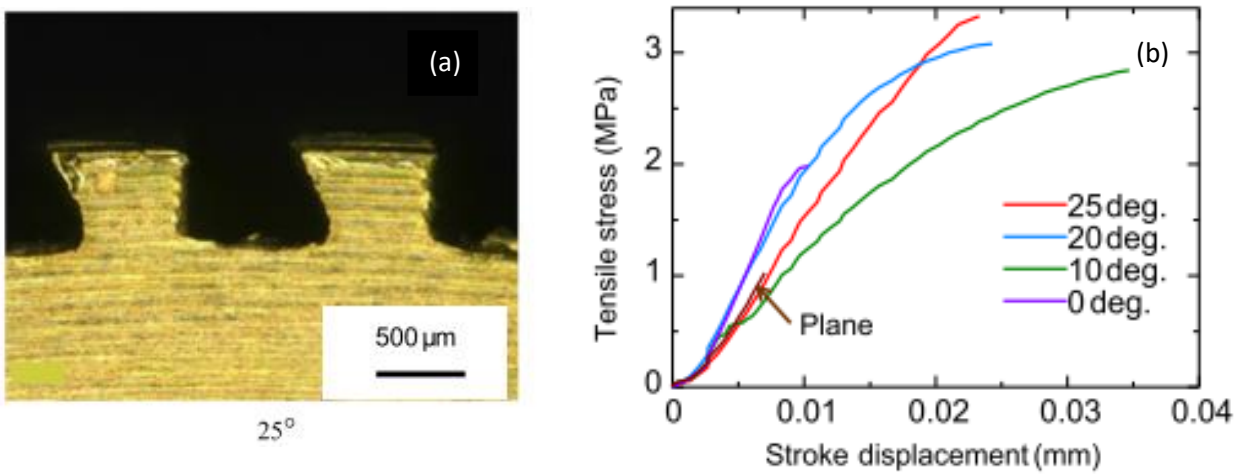

Figure 3-6: (a) Cross-sectional image of polypropylene patterning from roll imprinting with an undercut angle of 25° and (b) Stress-displacement graphs for planar polypropylene joints and structured patterns with various undercut angles from [53].

3.4: Response to the literature and aims of the thesis

Through reviewing the key areas of work related to the proposed research, it is clear that each area does not fully address the keys aims of the work. These can be summarised below:

- Micro-feature geometries and relative dimensions need to be precisely controlled (not possible via laser-ablation)
- Interlocking needs to be introduced at the adherend-to adherend level (not possible via laser ablation or previously studied 'micron-scale' techniques)

- Micron-level resolution is required to impart a high feature density as well as minimise impact on overall joint architecture (not possible via previous larger-scale interlocking approaches)

Based on the limitations outlined above, it is evident that a micro-fabrication strategy that can suitably address all three criteria would be a valuable area to research to understand the implications on adhesive joint performance. We propose there are several mechanisms that can lead to increases in mechanical strength, joint toughness and repeatability at the point of assembly. Since the usage of adhesive joints within critical engineering applications is hampered due to concerns about varying failure loads and failure types, the reasons outlined below are proposed to strengthen the argument for using adhesive bonding.

3.4.1 : Increasing the bonding area and adhesive interlocking

As elucidated from the studies provided, a substantial increase in the surface area can lead to an improvement in joint strength. Through the fabrication of highly dense patterns, a many-fold increase in active adhesive surface area can be achieved leading to higher joint toughness. Furthermore, a substantial contribution can be expected from the mechanical keying of adhesive.

3.4.2: How will surface patterning modify stress distribution?

The implementation of patterning at the interface can be an effective approach to redistributing a load across its bond-line. From the stress distributions in Fig. 2-6, the central regions of the bonded area experience a much lower load relative to the extremities of the bonded area. It is hypothesised that interlocking features across the entire bonded area provides a unique avenue to potentially modify stress distribution across the bond-line through the incorporation of varying feature geometries. In this scenario, the prospect of more compliant features (higher aspect ratio features) can be positioned at the extremities of the joint enabling greater feature deflection to potentially nullify the high peak stresses that are typically present within unstructured bonded joints. This hypothesis is concept is investigated within the 3D -printing research in Chapter 7.

3.4.3: Crack propagation arrestment

Through the presence of the features, the adhesive layer morphology leads to a source of crack arrestment and improved joint toughness. Once a crack has initiated within the adhesive layer, the features can provide a barrier to further crack propagation. The patterned features could result in a 'stick-slip' scenario in which the crack is impeded substantially at periodic points across the bond-line, leading to a greater overall energy dissipation. The idea of a more obstructive crack path is illustrated in Fig.3-7.

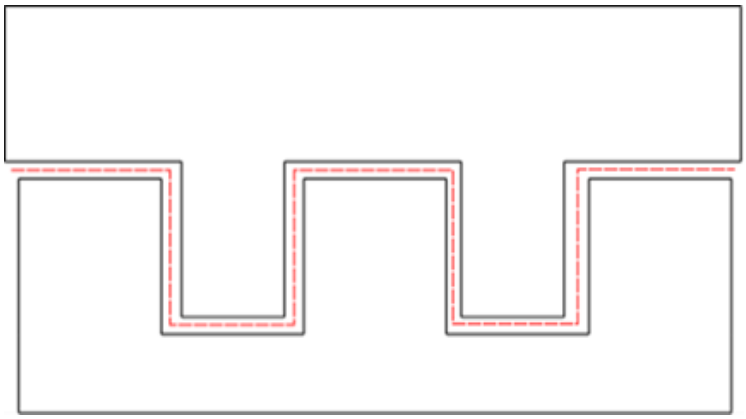

Figure 3-7: Representation of crack path for rectangular pattern. The more torturous crack path developed through patterning will require the crack to redirect orthogonal to the loading direction, requiring greater work to failure.

A further source of enhancement within this mechanism is the localised regions of compression loading between articulating micro-structures. It is hypothesised that this will mitigate adhesive failure from dictating the failure of the joint with the bulk phase enabling substantial increases in strength. It has been postulated that this proposed mechanism could be greatly enhanced through the use of a suitably ductile adherend, possibly through the use of polymers such as polycarbonate, bond strength could be increased through localised adherend deformation. The overall toughness of the joint could be greatly enhanced in a scenario where the adherend plasticity can be incorporated into the bond-line of the joint. A novel feature of the patterned bonded joints is the ability to transmit load throughout the structure through an additional means other than the adhesive itself. The adherend material will possess greater mechanical properties relative to the adhesive layer, providing an opportunity for a substantial strength improvement. The interlocking of features will enable this direct contribution to the strength of the bond. With reference to the crack opening mechanism outlined in Fig. 3.7, the prospect of micro-structuring using square waves will enable a mixed mode loading to

assist in modifying the crack propagation mechanism. It is well-established that adhesives are typically stronger under shear loading relative to tensile loading. Micro-structuring will lead to shear loading at the top faces of each feature with Mode I loading occurring on the sidewalls.

3.5: Aims of the thesis

This chapter has put forward the key information surrounding adhesive bonding research with a focus on the untapped area of study associated with micron-scale interlocking adhesive joints. Based on the results obtained pursuing similar structured interfaces, it is logical to deduce that substantial improvements can be attained through micro-structuring. The aims of this thesis are to:

- Successfully fabricate and test micron-structured joint interfaces using conventional cleanroom techniques to realise structured polymer interfaces.
- Illustrate the viability of the micro-fabrication processes for a range of engineering materials through employing additional manufacturing processes e.g. injection moulding based production.
- Confirm that interlocking of mechanical specimens is possible and consistently achievable at the point of joint assembly
- Determine the load carrying capacity of mechanical interlocking (i.e. independent from the adhesive)
- Ascertain the implications and potential mechanical benefits associated with micro-structuring of adherends for adhesive bonding relative to un-structured, planar joints.
- Explain the underlying mechanisms that underpin joint strength and toughness in mechanical interlocking scenarios by varying key geometrical parameters.
- Model the structured joints through finite element analysis techniques to expedite the testing of various microscale geometries and optimise joint design.
- Study the viability of 3D-printing based manufacturing as a route for more rapid and cost effective structured adherend production for real-world engineering applications.

3.6: Structure of the thesis

The remaining chapters are separated into distinct stages of research within the remit of micro-structured adhesive bonding.

The first research chapter (Chapter 4) provides relevant data and insight into the various micro-fabrication techniques used throughout the research as well as details regarding the production of polymer joints via micro-injection moulding. Chapter 5 documents the design of a custom test rig to enable the successful testing of single lap joints within a conventional tensile testing setup as well as reviewing the results obtained for a brittle substrate material (silicon) as well as a detailed analysis of the mechanical performance of ductile polycarbonate adhesive joints. The third research chapter (Chapter 6) documents the process of modelling structured joints and the design optimisation through statistical methods to further understand micro-structured interlocking. Within this chapter, the conventional approach of cohesive zone modelling is addressed and other approaches are explored with the interlocking behaviour of the micro-structured joint considered. Chapter 7 assesses the prospect of 3D-printing of joints and the scope for extrapolating this work into real-life engineering applications. This chapter provides a unique opportunity to rapidly prototype designs expediting concept to testing phase. The thesis concludes with a holistic assessment of the research outcomes, determining the extent to which the initial aims of the research have been successfully addressed.

Chapter 4 Microfabrication techniques

This chapter documents the various micro-fabrication strategies used to realise the production of micro-structured interfaces. For convenience in terms of structure surfaces, this work initially started out using silicon as the substrate material and later evolved towards injection moulded polycarbonate substrates. The corresponding section relating the experimental testing is provided in Chapter 5.

4.1 Silicon micro-fabrication

Silicon was chosen as the initial test material based on the relatively straightforward fabrication process. Silicon is used predominantly in cleanroom applications due to its fundamental role in the semiconductor industry. Micro-fabrication processes are largely based on earlier work in the semi-conductor industry. The key processes are photoresist spinning, photolithography, resist development and anisotropic etching. The key stages are shown in Fig. 4-1.

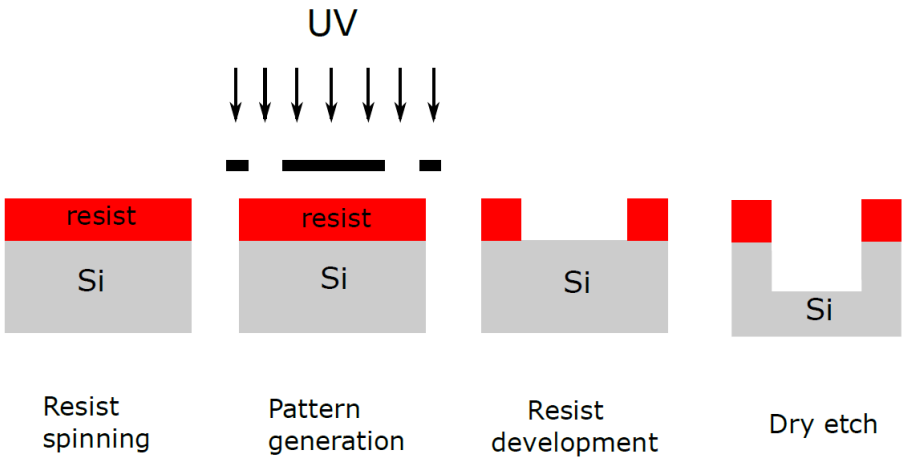

Figure 4-1: Schematic highlighting the key stages in the silicon micro-fabrication strategy used throughout this work

4.1.1 Resist Spinning: S1828 photoresist

The first stage in the process is the dispensing and subsequent spinning of a photo-sensitive substance known as a photoresist. Precise thicknesses are achieved through using specific spinning speeds, with

thinner resist layers achieved with increasing spin speed. Typical film thickness ranges from sub micrometre thicknesses for electron beam lithography to several hundred micrometres.

Throughout all the silicon etching fabrication, the positive tone resist S1828 was used with a spin speed of 3000 rpm; this leads to a thickness of 3.6µm. Other positive tone resists were trialled throughout the work. The S1828 resist was chosen due to possessing a larger film thickness relative to other available positive resists. This, in turn, enabled greater deep-etching performance as the directionality of this process is highly dependent on resist thickness (see Section 2.1.4).

An experimental spin curve was developed to determine resist thickness at spin speed ranging from 1000 rpm to 4000 rpm; this is shown in Fig.4-2.

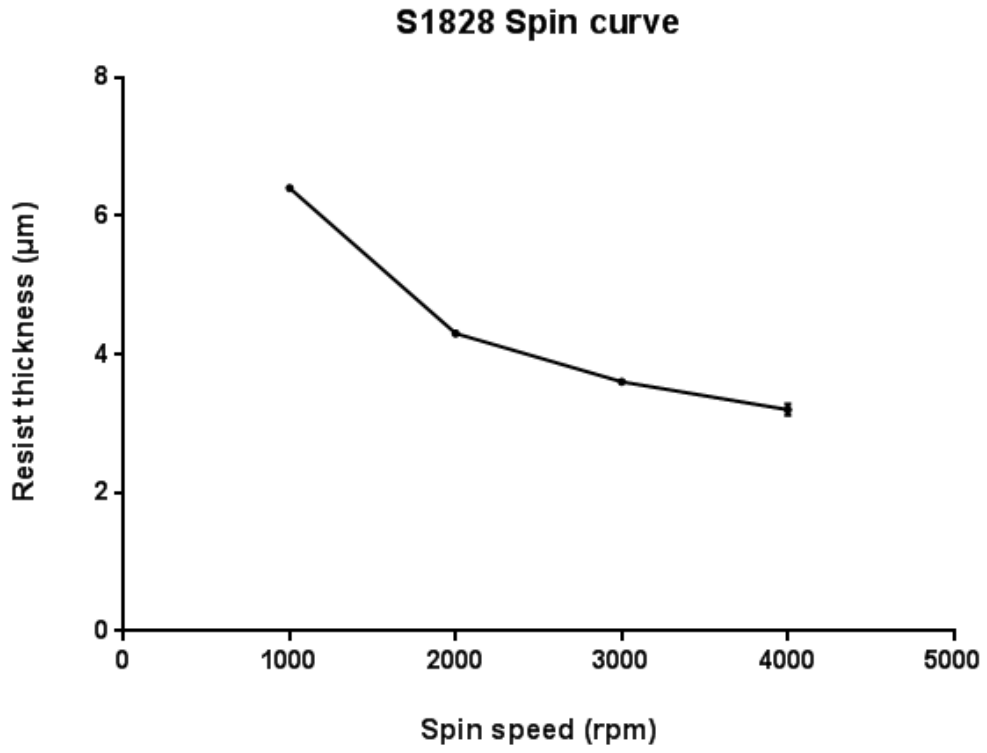

Figure 4-2: Experimental spin curve for the positive tone resist S1828 with resist thickness (µm) versus spin speed (RPM), error bars for each entry are (+/-SD).

4.1.2 Photolithography and resist development

The second stage involves selectively exposing regions of the resist to UV light through photolithography. A photomask sits intermediately between the light source and the sample, light can be selectively applied to parts of the sample, leaving other regions unexposed, this is shown in figure

4-3. Photolithography is the method of choice for a minimum feature size typically within the micrometre range. The maximum resolution, *R* obtainable for photolithography-based pattern exposure can be expressed as:

$$R = \frac{k\lambda}{NA}, \qquad \text{(Eq4.1)}$$

where *k* is a process constant (typically 0.4 for mass production, λ is the wavelength of the light source and NA is the numerical aperture for the lens system (a value of 0.6 is common). The numerical aperture parameter represents the range of angles at which light can leave or enter the lens, providing a metric for the resolving power of the lens. Using these values alongside a light source wavelength of 365 nm equates to a maximum resolution of 170 nm. The resolution of photolithography is limited by the diffraction of the incident light, resist properties and the gap between mask and resist [54]. The photoresists can be classified as positive or negative tone. When positive resists are exposed to UV light, the polymer bonds within the exposed areas are broken down. In contrast, the bonds in a negative tone photoresist are strengthened through exposure. Common positive photoresists include S1800 resists that have typical thicknesses ranging 1-4 µm. The most prominent negative tone resist is known as SU-8 which can achieve thickness up to 500µm. In this work, a Karl Suss MA6 Mask Aligner was used for photolithography. During the development phase post-exposure, the comparably weaker regions of the photoresist can be removed using specific chemicals where the dissolution rates of exposed regions differs greatly compared to unexposed regions of resist.

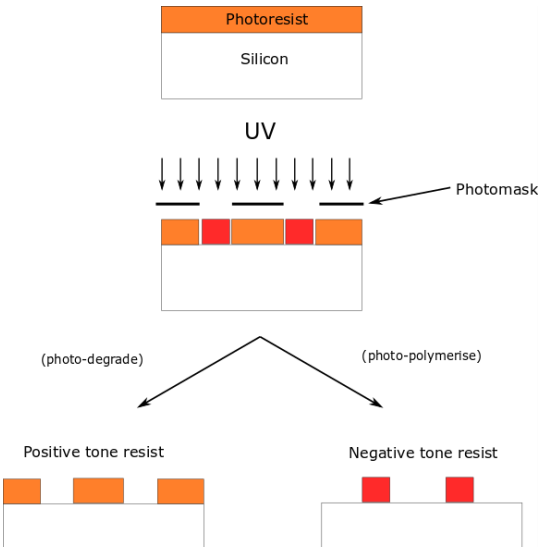

Figure 4-3: Resist tone: Positive resist is weakened in regions of UV exposure and is removed with greater ease (left); Negative resists photopolymerise under UV exposure and remain after development (right).

4.1.3 Metrology techniques

An integral part of the fabrication phase of work involved quantifying the quality of micro-fabrication work to assess process viability. Various metrology tools were employed over the course of the research; this section will provide details regarding these tools as well as details of the analyses.

4.1.3.1: Contact profilometry

Contact profilometry is an accurate and straightforward measurement technology where a stylus runs across the surface of a sample providing spatial data as a function of the scanning length. Within the scope of the present research, contact profilometry was used to assess feature heights primarily. Contact (or stylus profilometry) relies upon the physical scanning of a probe across the sample surface. A feedback loop is employed monitoring the force exerted from the sample onto the probe to ensure that the probe maintains physical contact with the sample. Deviations in the probes positioning are recorded through the use of position-sensitive photo-detectors that convert position data to electrical data that can be shown graphically.

In this work, the Dektak XT (Bruker, Germany) stylus profilometer was used. Analysis was performed using Vision64 software, which is the corresponding software for this specific profilometry tool. To minimise inaccuracies in measurements, data levelling was employed to provide accurate values for feature heights. Due to the requirement for the stylus to come into contact with the surface, lateral dimensions were not measured using this method [55,56].

4.1.3.2: Optical profilometry

Another branch of profilometry known as optical (or non-contact) profilometry was used extensively throughout the project to quantify both heights as well as lateral dimensions. Two different optical profilers were used, the Contour GT (Bruker, Germany) and the Alicona InfiniteFocus (Alicona, Austria). The Contour GT is suitable for test samples exhibiting low roughness, with a resolution on the nanometre range; therefore, it was ideal for analysis of cleanroom substrates. The operating principle for optical profilometry is termed white light vertical scanning interferometry, where light is separated into two beams, one is directed towards the sample, the other is sent to an internal reference mirror, these two beams of light recombine and are sent to a detector. The detector measures the intensity of the light as the interferometric objective is moved positionally in the vertical

axis, with the maximum interference between the beams recorded and positional data for the sample is produced [57].

Scanning electron microscopy

Scanning electron microscopy (SEM) was used for qualitative imaging primarily, with images taken to determine micro-fabrication quality. This technique relies upon the back-scattering of electrons hitting the sample, enabling nanoscale resolution. SEMs operate under a vacuum, with an electron beam hitting the sample. The subsequent back-scattering of these secondary electrons is detected and converted into a greyscale image [58]. The electron beam is created through the usage of an electron gun, emitting a beam of electrons. A column consisting of a series of electromagnetic lenses and apertures provide a mechanism to focus and direct the beam onto the sample. SEM typically employs two imaging detectors for detecting two separate types of electrons: secondary electrons and backscattered electrons. Scattered electrons are low-energy electrons emanating from close to surface of the substrate. In contrast, backscattered electrons (BE) are higher energy electrons, possessing a greater penetration depth into the sample [59].

For nanoscale fabrication work, the prospect of incident electrons impacting upon a substrate can lead to notable damage of nano-features. In this work, the comparably large feature size rendered this issue negligible. Conductive samples such as metals and silicon can be imaged effectively using the SEM process. For insulating materials such as polymers, samples are required to be sputter coated in gold-pallidum to enhance conductivity to improve image quality. Throughout this work the FEI Nova NanoSEM 630 microscope was used for any SEM-based metrology. It should be noted that all optical microscope and SEM images were analysed using ImageJ software. This software was particularly useful for measuring local feature sizes throughout the quantification work presented in this chapter.

4.1.4 Dry (anisotropic) etching

Dry etching uses plasma or gasses to remove substrate material. The most pertinent method of dry etching is known as Reactive Ion Etching (RIE). In the RIE process, cations are produced from compounds such as carbon tetrafluoride (CCl_4) and are accelerated towards the sample surface. Etch species containing halogens are the most extensively used. When RIE is used to produce large vertical profiles, the technique is known as deep reactive ion etching (DRIE) [60].

Anisotropic etching requires the employment of both chemical interactions as well as ion bombardment of the silicon. The ion bombardment enables material removal whilst the chemical

interaction enables passivation of the silicon sidewalls to ensure etching occurs exclusively in the vertical direction [61]. The schematic in Fig. 4-4 illustrates the alternation between etching and passivation phases leading to the vertical removal of silicon matter. Throughout this thesis, all dry etching was performed using the STS Inductively coupled plasma (ICP) etch tool.

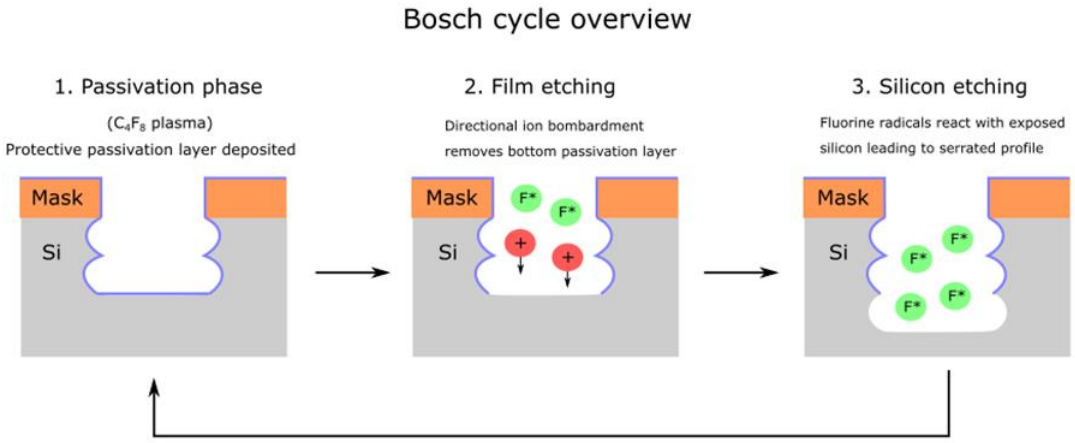

Figure 4-4: Schematic summarising the key phases associated with the Bosch process etch cycle. The passivation phase involves the deposition of a protective layer (violet layer) using C4F8 plasma (Step 1); the film etching phase involves directional ion bombardment (red circles) attracted via voltage bias to remove the passivation layer (Step 2) with fluorine free radicals (green circles) used to etch the exposed silicon whilst the sidewalls are protected (Step 3), leading to a serrated sidewall profile as the phases alternate.

The alternating phases in the process lead to a serrated profile as opposed to a continuous form. The highly directional form of the etch as well as the serrated sidewalls are exemplified in Fig. 4-5. As will be discussed in the experimental testing section, silicon proved to be a sub-optimal material for mechanical testing as the highly brittle nature resulted in great difficulty when testing within an adhesive joint configuration. However, this work proved invaluable as the starting point of the fabrication work performed in the JWNC.

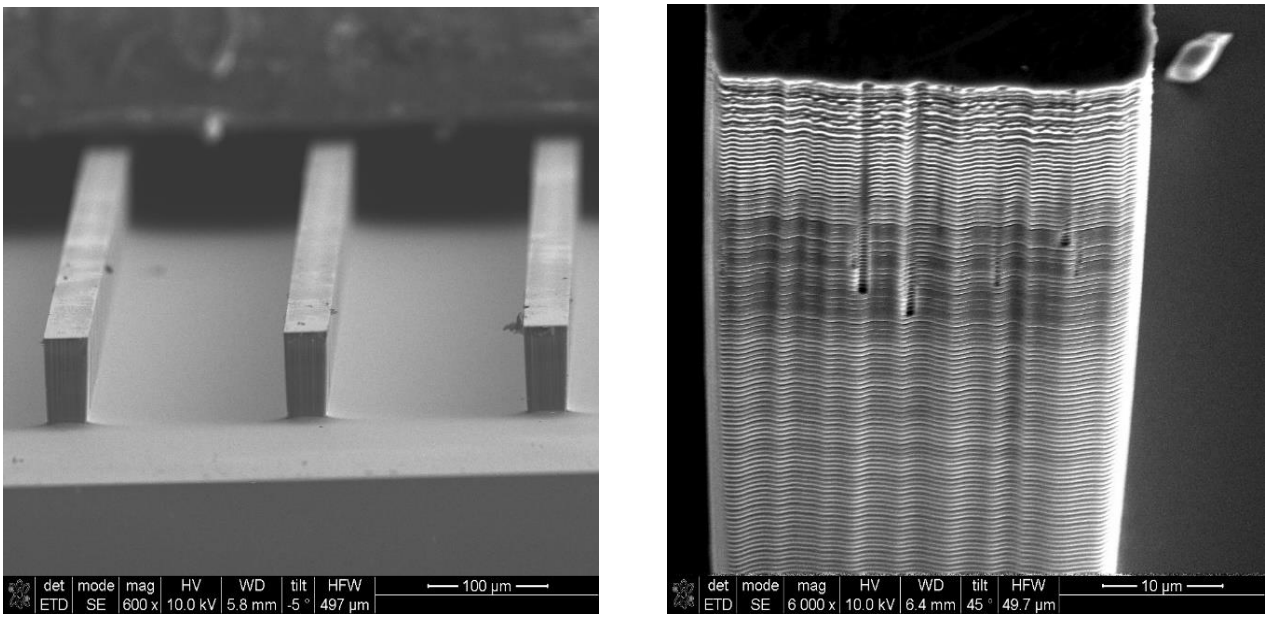

Figure 4-5: SEMs of etched silicon, image on left illustrates the repeatable feature geometries and pitch obtained through the microfabrication process; image on the right shows the serrated etch profile obtained from a Bosch process etch.

4.1.5: Proposed alternative: SU8 resist on Stainless steel

4.1.5.1 SU-8 Background

An alternative configuration was proposed in which the substrate material would be highly polished Stainless steel 316L with features composed of the negative resist SU8-3050. The family of negative tone resists known under the umbrella term 'SU-8' are an epoxy-based resist developed and patented by IBM. The distinct advantage of using SU-8 resists is the capability of producing large thicknesses (upwards of 2mm) and high aspect ratios (upwards of 20) [62, 63]. The advantages of this concept are largely based on the relative ductility of steel compared to silicon as well as the option to clamp the steel as opposed to fixing the joint via adhesive. Before the fabrication stage, it was important to establish the overall surface quality to determine the viability of the steel substrate as a microfabrication material. To achieve a relatively confluent, flat SU-8 resist layer, low roughness values are required. To achieve this, optical profiles of the stainless steel were taken to visualise topography and find the surface roughness. The 2D plot in Fig. 4-6 is supplemented by Table 4-1 giving the key roughness parameters averaged across the sample area alongside the standard deviations. Average roughness (Ra) and Root-mean squared values (R_q) were used to ensure that both positive and negative topographies were accurately represented in the roughness measurements. The average values were obtained from five sampling lengths within the Vision 64 surface profilometry software.

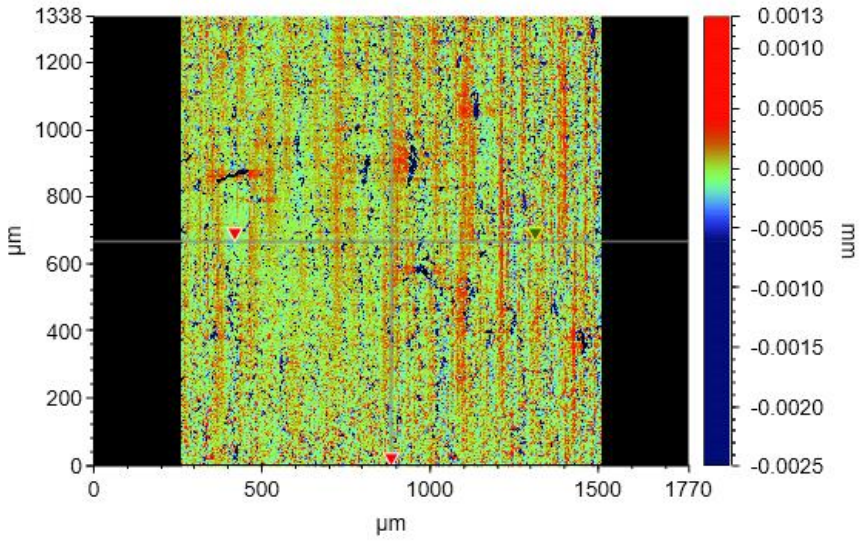

Figure 4-6: 2D Contour plot of Stainless steel 316L topography the axes correspond to the scanning area for the sample in µm as well as the measured surface heights for each point in mm.

Table 4-1: Selected surface roughness values for the 316L stainless steel substrate

Parameter	Mean (µm)	S.D (nm)
Ra	0.148	12.9
Rq	0.211	10.8
R(max)	1.73	0.31

The roughness values obtained for the steel samples were deemed suitable to pursue as a substrate. Although the roughness values are markedly higher than a silicon wafer (approximately 0.1 nm), for the fabrication of large features of 50µm and greater, this value should suffice. From a fabrication perspective, a point of concern was the potential for light scattering during photolithography to occur due to the elevated surface roughness leading to some feature size variation.

4.1.5.2: Fabrication process for SU8-3050

SU-8 resist was spun at 2000 rpm for thirty seconds to achieve a resist thickness of approximately 68 µm. A pre-exposure bake of one hour on a hotplate at 95°C was used to evaporate all the solvent from the resist prior to UV exposure. An exposure time of 60 seconds was used followed by a post-exposure bake for five minutes with a gradual ramping of the temperature from 65 to 95°C to prevent the resist cracking. Unexposed resist was removed through developing in EC-solvent for 8 minutes followed by a wash in isopropanol. The optical profiles obtained for the SU8-steel specimens were generally encouraging with the feature sizes remaining consistent across the sample area. Feature heights were around 64µm compared to the quoted value of 68µm from the datasheet. It was hypothesised that the slight decrease in resist thickness will be due to the lower adhesion of SU8 to steel relative to silicon.

The image in Fig. 4-7 conveys the feature enlargement caused by light scattering due to the roughness in steel. The 150µm designed feature size was found to be closer to 175µm; the 450µm trenches were then reduced to a size of around 425µm. Although these variations are not ideal, the disparity from the initial mask features could be accounted for through plotting the feature enlargement versus feature size for a range of linewidths and designing in accordance to the trend line observed.

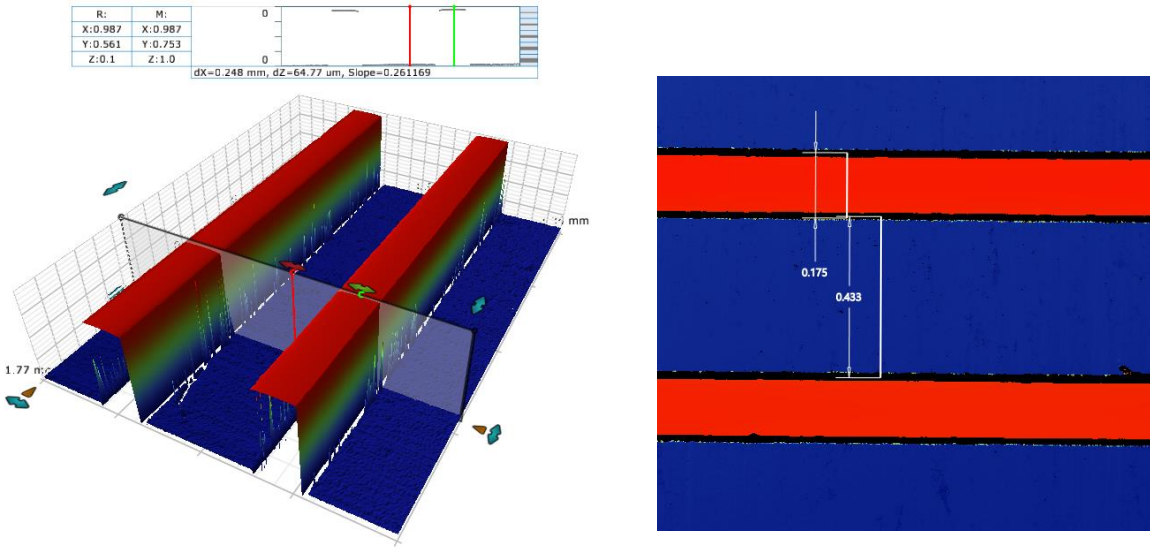

Figure 4-7: Optical profile of SU-3050 features on steel. The feature height dz = 64.77 µm.

The main drawback of using this material for testing was the bi-material aspect alongside relatively poor adhesion between the SU-8 and the steel. The SU-8 micro-features proved to easily delaminate from the substrate under relatively minimal loading. A possible area to explore could have been the

use of aluminium as a substrate material as this has higher quoted bonding strength to the SU-8 material, although it seemed unlikely that such improvements would be sufficient. At this point, the project pivoted towards looking at finding a fabrication route to enable the micro-structures to be realised within polymers, enabling all the key attributes outlined earlier in this section to be satisfied.

4.2 Injection moulding

Due to the problems with the brittle silicon and the poor SU-8 to steel adhesion, the focus of the project then shifted towards aligning cleanroom micro-fabrication with manufacturing techniques to enable polymer fabrication. The key advantages identified for polymer joints are:

1. The option to create highly ductile joints (polycarbonate or polypropylene) where the presence of the interlocking features can be fully studied

2. Optical transparency of many polymers would be advantageous for in-situ imaging during testing

3. Manufacturing of polymers from an initial master boasts high throughput with high numbers of test samples produced economically

4.2.1 Overview

The most optimal method of making micro-structured polymers involved incorporating injection moulding into the fabrication process. Injection moulding is a well-established manufacturing process that is heavily used in producing plastic parts industrially. A notable example of its employment was in the 1980s with the inception of compact disks, where micrometre-sized features required repeatable and economical replication [64]. The injection moulding process (Fig. 4-8) entails the heating of a chosen polymer to around 100 degrees above its glass transition temperature $T_{g,}$, the polymer is then injected into a mould cavity that is kept at a much lower temperature, typically 50 degrees below $T_{g.}$ The polymer subsequently cools and is ejected with this cycle repeating

The polymer is placed into the hopper in the form of pellets which are directed under gravity into one end of a screw. The polymer is then heated through four separate heating elements, each successively increasing the temperature of the melt. Through increasing temperature, the rotational motion of the polymer and a narrowing gap of the screw, the polymer reaches the nozzle at the end of the screw fully homogenised in both temperature and form in a process known as plasticising [65]. A first polymer shot is required to fill the mould cavity to enable pressure build-up in the screw. This mechanism is enabled through the presence of a non-return valve at the injection end of the screw. This valve moves back through the presence of polymer, when the cavity is filled with polymer this

valve prevents further flow through the nozzle, effectively preparing for the next shot. The main components of an injection moulder are highlighted in Fig. 4-8. The polymer is injected through pressure exerted via a thrust emanating from the injection cylinder, at the distal end of the screw. The polymer passes through a passageway connecting the nozzle to the mould cavity, known as the sprue; this region forms the narrow protrusion on each solidified part. Once the mould cavity is filled, the part is held under pressure to mitigate shrinkage and is subsequently ejected, enabling the mould cycle to progress [27].

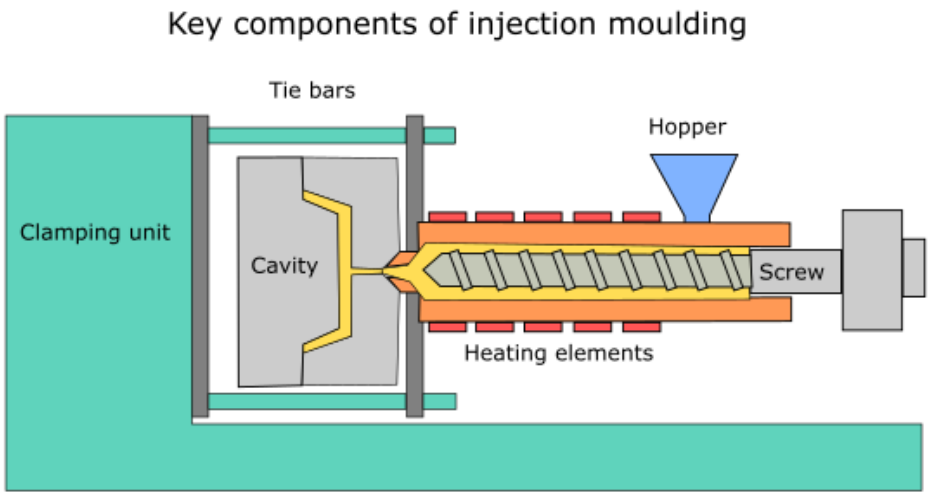

Figure 4-8: Schematic of injection moulding machine with major components annotated.

Injection moulding can be utilised for both amorphous and semi-crystalline polymers. Amorphous polymers have a randomly ordered molecular structure that lack a sharp melting point. The result is that amorphous materials soften gradually as the temperature increases. These materials exhibit better forming properties and reduced proclivity to warp upon cooling. Within the present study the amorphous polymer, polycarbonate was chosen for final testing. In contrast, semi-crystalline polymers have a highly ordered molecular structure with sharp melting points, these materials tend to have enhanced mechanical strength although there is a notably increased warpage upon cooling relative to amorphous polymers.

4.2.2 Injection moulding tooling

There are various sub-components that comprise the tooling that ultimately determines the mould cavity enabling the production of moulded parts. Conventional mould tooling, used in the creation of common everyday products (such as car dashboards) is generally made by milling steel and assembling all parts to form the desired cavity dimensions. The mould production process to enable the successful

replication of micro- or nanoscale features requires notable adaptations to the tool design process as the high resolution necessary cannot be achieved via conventional machining techniques. The most commonly adopted method to mould micro and nanoscale structured surfaces relies upon the utilisation of hybrid tooling where a non-metallic insert can be added into the mould cavity configuration. This insert is manufactured through employing cleanroom techniques where the micro/nano structure can be successfully fabricated. A schematic of the hybrid tooling configuration is given in Fig. 4-9 with an exploded view and enclosed setup shown. As can be seen, the polymer-based inlay is encased between the steel back plate and frame. When the movable platen comes into contact with the fixed platen, the dimensions of the moulded part are determined (see Fig. 4.9b) Within this setup, the inlay (also known as an insert) is the component created via cleanroom techniques in advance by other means. The inlay, supported by the backplate, fits inside the frame, which is subsequently inserted into the main tooling of the moulder. Parts are produced in accordance with the dimensions defined once the tooling is enclosed. In the current work, two different inlay dimensions of 25 mm x 25mm ('small tool') and 75 mm x 25 mm ('slide tool') were used producing parts of 2 mm and 1 mm thickness, respectively. Photographs showing the different moulded parts are provided in Fig. 4-10.

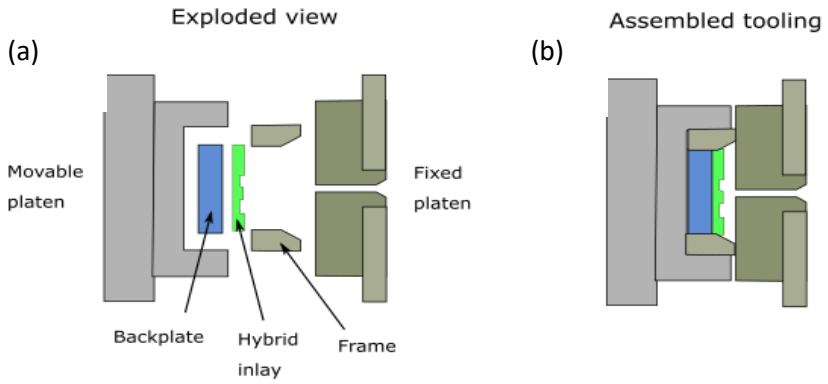

Figure 4-9: Overview of hybrid tooling setup used for injection moulding of micro-structures: (a) exploded view and (b) the view during operation.

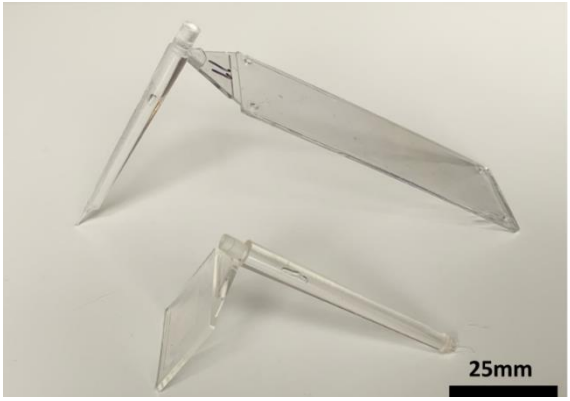

Figure 4-10: Photographs of moulded parts for the 'slide tool' (top) and 'small tool' (bottom).

There are several key parameters related to the mould cycle that must be considered to ensure high part quality. These are:

- Injection velocity
- Tooling temperature
- Mould temperature
- Holding pressure
- Cooling time

The Injection velocity largely defines the injection time and pressure, controlling the rate at which the polymer melt is injected. A common issue whereby the melt freezes prematurely can arise if this value is set too low; leading to incomplete parts and inaccurate geometries. If the injection velocity is too high, there is potential for the polymer melt to infiltrate other regions of tooling in a process known as flashing. The tool temperature dictates the cooling rate of the polymer melt once it has been injected into the cavity. A value that is too low will result in poor filling due to an overly high temperature gradient. Setting this value too low will lead to overly high cooling times as well as risking incomplete cooling causing problems during the ejection phase. The melt temperature determines the viscosity and flow properties of the polymer during injection. A value that is too low can lead to mould-filling issues. A value that is too high can lead to excessive cooling times. The holding pressure refers to the pressure at which the polymer is held following injection. This pressure counteracts shrinkage within the cavity to ensure proper filling is achieved. Too low a value can lead to improper part geometries. Cooling time refers to the period after the injection and holding phase where the tool is effectively stagnant, waiting on the part to sufficiently cool. If this time is too short, part deformation is likely. Assigning too high a value extends the time required.

4.2.3 Micro-injection moulding overview

Micro-injection moulding has proven to be a promising approach to produce micro-structured parts with a high degree of precision and excellent throughput [66-74]. Injection moulding is a well-established technique that has been used for decades within the manufacturing industry on account of its efficient use of time and resources. The process can be used with a range of polymers with parts produced based on the dimensions of the tooling used. Within the field of surface engineering, injection moulding has been utilised with the successful replication of features on the micro/nano-scale [75]. However, owing to the high number of variables that can influence process and part

performance, significant optimisation work is usually required. As outlined earlier, the main parameters are the mould temperature, melt temperature, injection speed, holding pressure, mould inlay material and type of polymer used. To ensure complete filling of micro-cavities during the mould cycle, it is imperative that these parameters are carefully selected.

A wide range of different polymers have been used within the field of micro-injection moulding [43, [75-78]. Common thermoplastics used include polystyrene (PS) [79], polypropylene (PP) [80], polycarbonate (PC) [68, 81], cyclic olefin copolymer (COC) [82], poly methyl methacrylate (PMMA) [79,72], polyoxymethylene (POM) [83], polyethylene (PE) [79], polyether ether ketone (PEEK) [84,85], acrylonitrile butadiene styrene (ABS) [79]. The major difference with conventional injection moulding, is the need for alternative tooling materials to ensure the requirements of micron-scale resolution, durability and complete micro-cavity filling are met. Micro-moulding research has researched the possibility to use silicon mould inserts, although the highly brittle nature of silicon results in fracture under the high pressures in injection moulding [70,86,87].

Metal-based moulding is more favourable due to higher associated strength. However, the increase in cooling rate leads to more rapid solidification that can risk part fidelity. Rapid cooling tends to result in incomplete filling of micro/nano-cavities, and a frozen polymer layer precipitating is often observed prior to fully filling [88]. Metal inserts can be fabricated through techniques such as electrical discharge machining (µEDM), micro mechanical milling and electrochemical machining (ECM) [89-91]. These approaches tend to result in high surface roughness as well as a marked reduction in minimum feature size relative to silicon microfabrication strategies.

A popular insert production method is LIGA (German for: Lithography, Electroplating, and Moulding). This approach produces a replica of the original substrate through the creation of a metal master via electroplating; this master is then used as the moulding insert. Conventionally, nickel-based electroplating is used; a schematic of the LIGA process is provided in Fig. 4-11 [92]. It should be noted that this process is conceptually similar to the epoxy-casting approach researched previously.

Finally, an emerging replacement for the LIGA process comes in the form of hybrid inserts. In this configuration a polymer-based layer is housed within conventional metallic tooling [93]. Within this setup, the lower thermal conductivity of the polymer facilitates a longer period of time for filling to occur, leading to enhanced replication. The metal tooling component provides greater cooling and heat transfer after the filling phase providing a useful compromise between part fidelity and throughput.

4.2.4: Fabrication of mould insert: mixed etch master

A key consideration to address was the successful separation of the mould inlay and moulded part. To achieve this, a smooth draft angle of approximately 10^{o} is imparted on the parts through modifying the etch process to continuously have passivation and etching occur at the same time [94]. It should be noted that the maximum etch depths obtained via the mixed etch process are lower relative to the Bosch process due to a reduced etch rate and photoresist selectivity. Fig. 4-11 compares the sidewalls produced with each process.

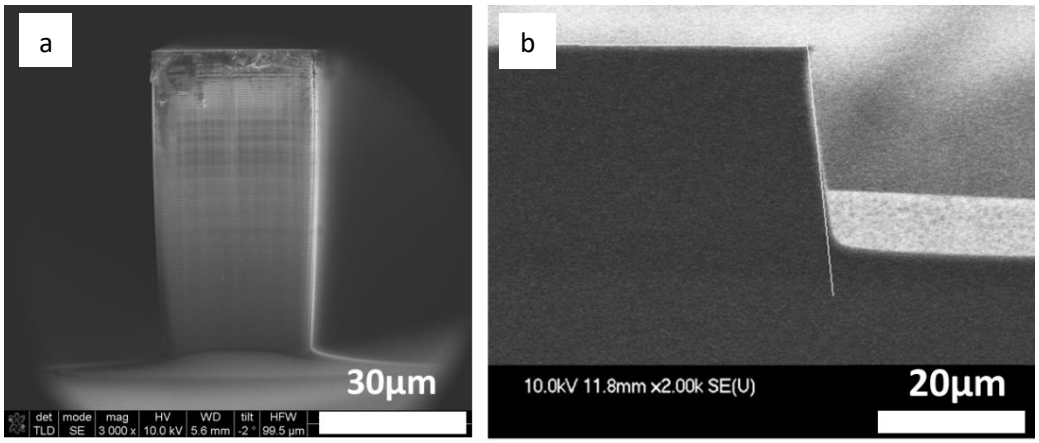

Figure 4-11: Cross sectional SEMs highlighting (a) the nanometre scale scalloping associated with Bosch process etching and (b) the smooth positively sloped sidewalls obtained from mixed process etching.

4.3: Mould insert production

4.3.1: SU-8/TOPAS 5013 mould inlays (Option 1)

4.3.1.1: Working principle

An initial micro-fabrication strategy route was explored using the transparent polymer TOPAS 5013 as the substrate with SU-8 microfeatures as the mould inlay. TOPAS 5013 (otherwise known as cyclic olefin copolymer) is an amorphous polymer produced from copolymerisation reactions, providing markedly higher chemical resistance compared to comparable thermoplastics. This manufacturing approach relied heavily on the previous work using SU-8 with one major difference in the form of back-side UV exposure. SU-8 is a negative resist that forms structures through the process of photo-polymerisation - i.e. areas of UV exposure cure and form the feature after resist development. With conventional, top-side exposure, light intensity decreases as a function of resist depth, producing an undercut sidewall profile as conveyed in Fig. 4-12. This avenue was inspired by the work of Steigert et

al. [95], where they employed back-side exposure of SU-8 on TOPAS 5013 to reverse the profile orientation into a positive angle to enable mould retraction.

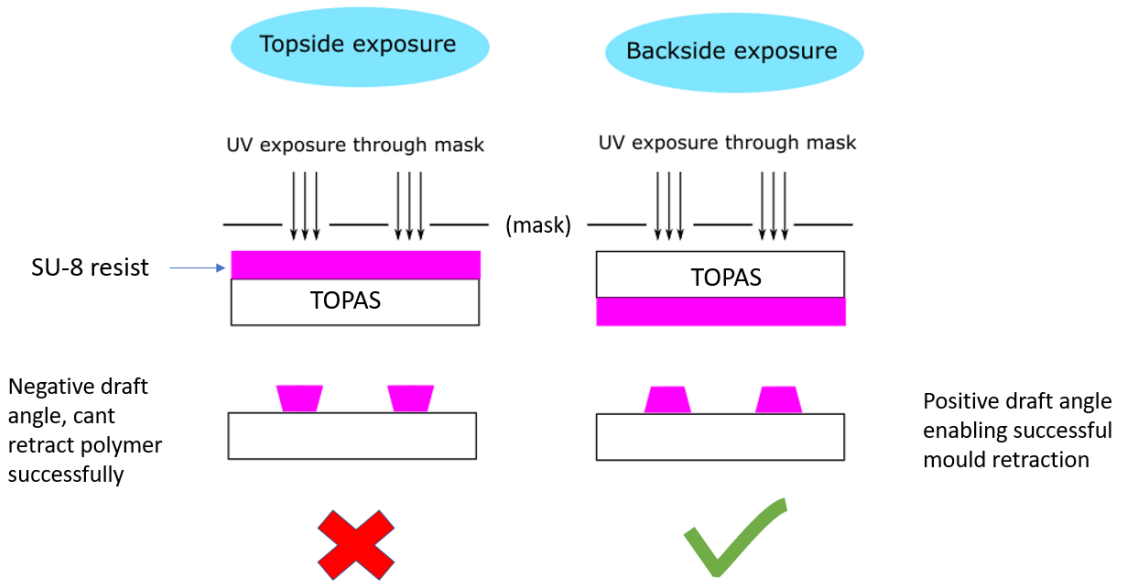

Figure 4-12: Schematic of photolithography results for a negative tone resist with topside exposure compared to backside exposure through a UV transmitting substrate such as TOPAS.

The major advantages of this route are the overall simplicity of the inlay fabrication in tandem with the large feature height sizes that can be obtained when using SU-8 (up to 1 mm heights). TOPAS was identified as the material of choice owing to its transparency, relatively robust thermal properties and chiefly due to its chemical resistance to the SU-8 developer (EC-solvent).

4.3.1.2: Results and limitations

Additional modifications to the fabrication procedure were made to account for the use of TOPAS 5013 as the substrate. These included lowering the dehydration bake temperature to 90°C as opposed to 180°C. The early fabrication of the TOPAS was leading to over-developed profiles as shown in the stylus profile in Fig. 4-13. The individual features started merging together, indicating that the bottom layers of SU-8 were receiving too high an exposure dose. To combat this issue, exposure times were drastically reduced compared to those used for silicon.

A trial mould run was performed with the SU-8 samples with the patterns de-laminating from the TOPAS after 5 cycles. Efforts to improve the mechanical strength of the interface through the deposition of nanometre metallic layers were studied. The metallic layer has good adhesion strength to the TOPAS as well as the SU-8, which may prove an avenue for mitigating the de-lamination. Another issue to acknowledge with this approach is the feature size variation based on the diffraction of light through the TOPAS substrate.

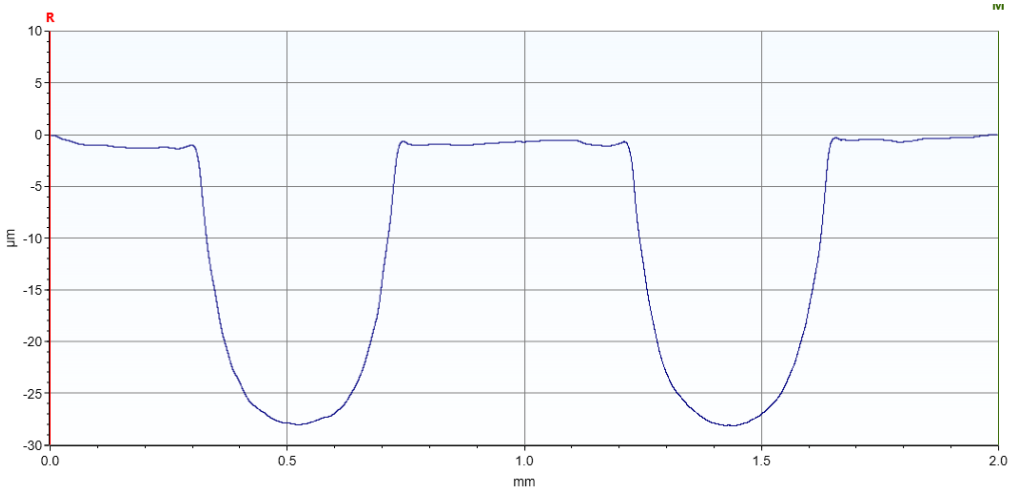

Figure 4-13: Over-exposed SU-8 profile following an exposure of 60s. Feature heights were found to be significantly lower than the intended 50 µm due to the merging of the bottom layers of SU-8 leading to a base layer.

The issue of surplus SU-8 resist within the channels was mitigated through lowering the UV-exposure during the photolithography stage. The lower exposure time was deemed still sufficient to define the micro-structuring as can be seen in the line profile in Fig. 4-14. The diffraction of light will result in greater lateral UV exposure: leading to feature enlargement. This problem can be largely diminished

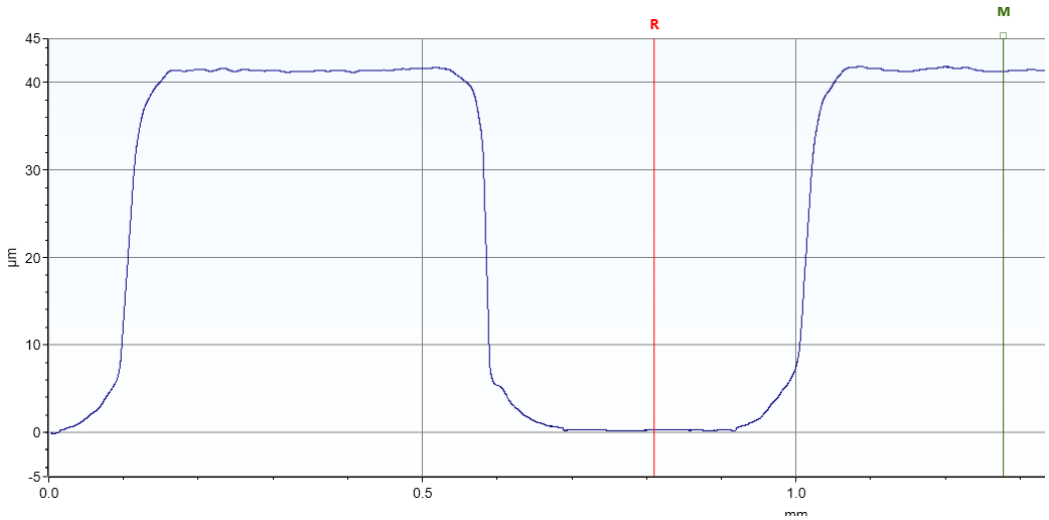

Figure 4-14: SU-8 profiles with a much lower exposure time of 20s. The merging of features has ceased; feature heights were less than the intended 50 µm; however, they were consistent across the central area of the sample at 42 µm.

through tracking the actual size versus the designed size and using the data as a prediction tool. The SEM image in Fig. 4-15 highlights the onset of damage within moulded polystyrene parts with delamination following shortly afterwards. Due to poor throughput in tandem with the relatively poor resolution of the process, this approach was not pursued, although an optimised approach may still be viable for certain injection moulding applications.

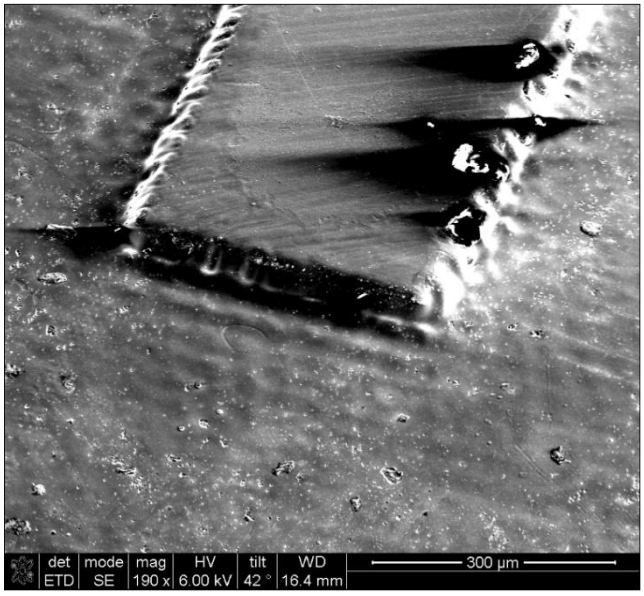

Figure 4-15: SEM of polystyrene pattern moulded from the SU-8 inlay. The linewidth of the SU-8 was 450 µm with a feature height of 42 µm. There is evident damage on the features, indicating deterioration of the mould inlay.

4.3.2: Epoxy mould inlay approach (Option 2)

4.3.2.1: Working principle

Another approach that was identified was previously employed by Steigert et al. [95] and was extensively explored as the main route to achieving micro-structured polymers with a variety of feature geometries. The schematic in Fig. 4-16 provides an overview for the process.

Starting with a micro-patterned silicon master (Step 1), patterns are cast and transferred into the elastomeric poly-dimethlysiloxane (PDMS); this serves as an intermediate step (Step 2). The use of PDMS within micro-fabrication processes is well-established with specific significance to the microfluidic community [96,97]. An epoxy containing 10 wt% aluminium powder known commercially as WEICON C is cast on the PDMS and thermally cured (Step 3); the cast epoxy becomes the mould insert (Step 4).

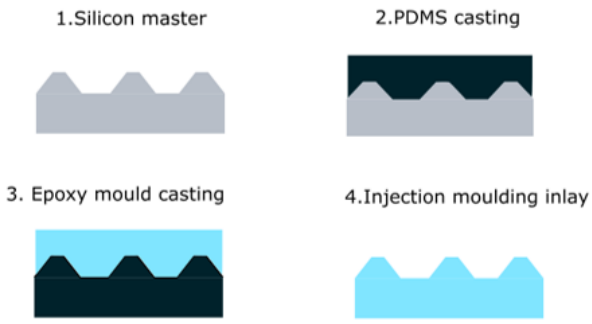

Figure 4-16: Schematic summarising the Epoxy casting procedure. The first stage involves obtaining an etched silicon master via photolithography and dry etching (Step 1). The second step entails pattern transfer to the PDMS yielding an inverse of the initial pattern (Step 2). The PDMS is then used in the epoxy casting phase (Step 3). Final step is injection moulding using the epoxy inlay (Step 4)

The trial fabrication was performed using a silicon wafer with 450 µm linewidths and 450 µm spacing. The etched features were created using a mixed process etch to obtain the positively sloped sidewalls, the feature heights were found to be approximately 36.7 µm. The feature height for this stage was arbitrary due to the preliminary nature of the work. Sylgard 184 Silicone elastomer kit was used to form the casting PDMS. A ratio of 10:1 between the resin and curing agent was weighed on a digital balance and mixed continuously for several minutes. The mixture was dessicated for 15 minutes to remove air bubbles. The mixture was then poured on top of the silicon and subsequently dessicated again for at least 15 minutes or until no bubbles were visible. The PDMS was cured at 80^{o}C for 4 hours and peeled away from the silicon. Through optical images taken for the PDMS, it is apparent that patterns of relatively small dimensions and complexity can be adequately transferred to the PDMS. The photograph in Fig. 4-17 illustrates the PDMS casting step.

Figure 4-17: Photograph of the PDMS pattern transfer stage with the silicon wafer underneath. The tinfoil is used to prevent PDMS overflow.

4.3.2.2: Casting rig and curing insert processing

The next step of the procedure is casting the WEICON C epoxy on top of the PDMS to the correct lateral dimensions and thickness to fit the moulder perfectly. To realise this, a simple casting rig was made from PMMA. A schematic of the casting rig is given in Fig. 4-18. The WEICON resin and hardener were mixed in a weight ratio of 100:8 respectively in accordance with the datasheet. The epoxy is then poured into the acrylic template and cured within an oven for 4 hours ramping the temperature to 80^{o}C. A mould release spray was applied to the acrylic to enable the epoxy to be removed from the rig after curing. To nullify any risk of the PMMA softening, the highest temperature the rig was subjected to during curing was set as 80^{o}C. At this point, the epoxy is removed from the rig and given a further curing at elevated temperatures of 100^{o}C to confer thermal stability to the epoxy. The final stage of mould processing is the filing of the back-side and edges of the mould to ensure a perfect fit with the moulding tool and backplates.

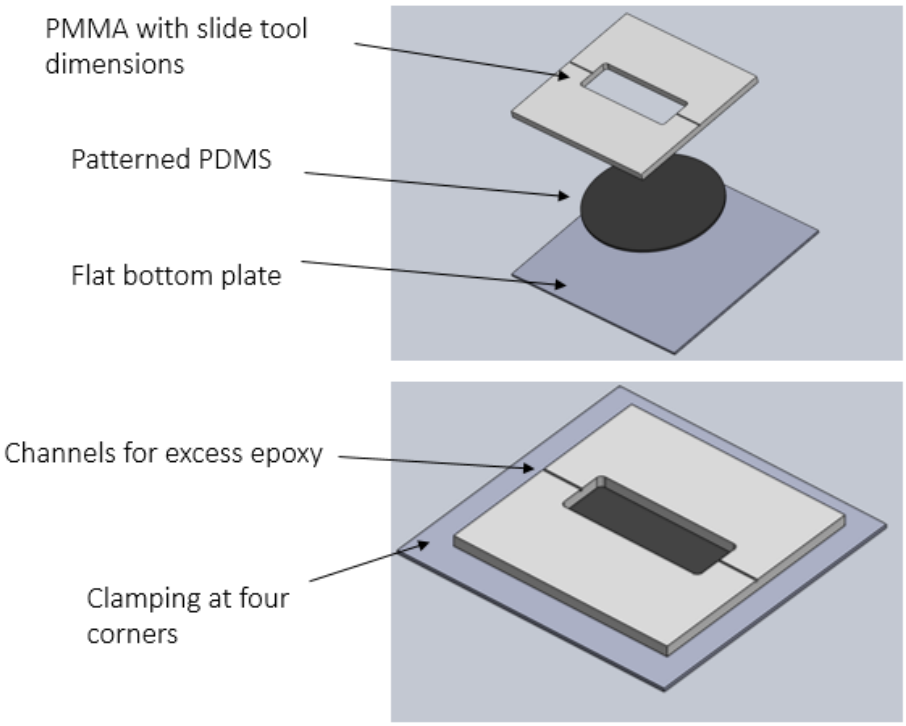

Figure 4-18: Exploded view of the components used in the epoxy casting rig.

4.3.2.3 Epoxy casting results

Optical profiles (see Fig. 4-19) were taken as well as stylus profiles to ascertain the surface quality of the epoxy cast parts and if there was any notable variation in dimensions in the mould relative to the silicon master. The feature heights were found to be smaller for the epoxy mould compared to the silicon, whilst the lateral dimensions exhibited a much narrower degree of variation. The key dimensions for the silicon master and WEICON epoxy part are given in Table 4-2. Mean surface roughness for the epoxy was characterised by the *Ra* and *Rq* values. Five sampling lengths were taken from a planar part of the epoxy sample and the resulting values were 82.6 nm and 159 nm, respectively.

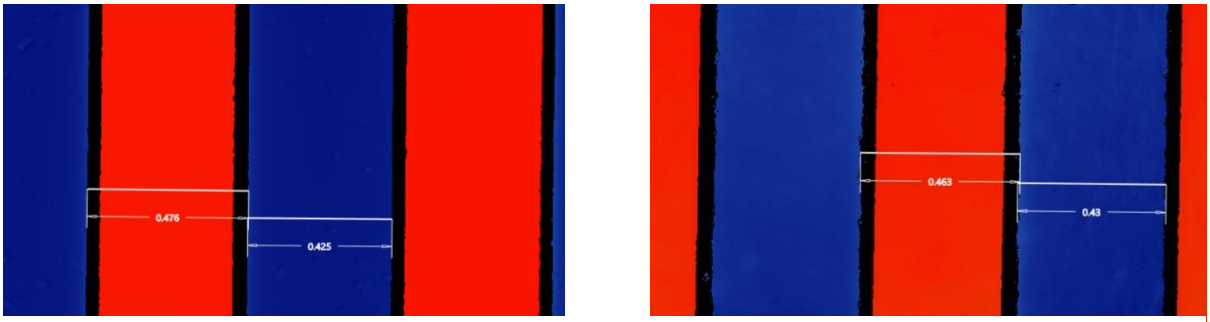

Figure 4-19: (left) Lateral dimensions for the silicon master (the red sections correspond to the gratings; blue sections correspond to the trenches) and (right) Lateral dimensions for the epoxy mould.

Table 4-2: Dimensional variation from the silicon master to the WEICON mould

Parameter	Silicon master	WEICON mould	% Variation
Height (µm)	36.9	33.5	9.2
Grating width (mm)	0.476	0.463	2.7
Trench width (mm)	0.425	0.43	1.2

At this stage, it was evident that the epoxy casting approach was capable of feature replication with low variation from the silicon. Additionally, the moulding results researched previously made this process increasingly promising. A useful concept was to analyse the capabilities of the epoxy casting technique by attempting to mould a more convoluted pattern. A microfluidic pattern from another branch of research was used. The lateral channel dimensions were 100µm with a serpentine-like channel design. The measured height of the channels were found to be 9.6µm via stylus profilometry.

Photolithography and reactive ion etching of silicon wafers was used to fabricate masters for the micro-imprinting process. To facilitate deep etching for the mixed etch process, the positive tone resist Megaposit SPR 220 7 was spun at 1500 rpm to obtain a sufficiently thick resist layer of 9.6µm. The channel depths were measured for the cast epoxy at three different locations with the mean depth found to be 9.3µm. The epoxy has an exceptionally low viscosity of 25mPas, enabling effective micro-cavity penetration, the height variation could be attributed to fractionally incomplete filling with the PDMS. Otherwise, there may be some mould shrinkage during the PDMS casting stage. Optical profiles for the epoxy mould inlay are given in Fig.4-20.

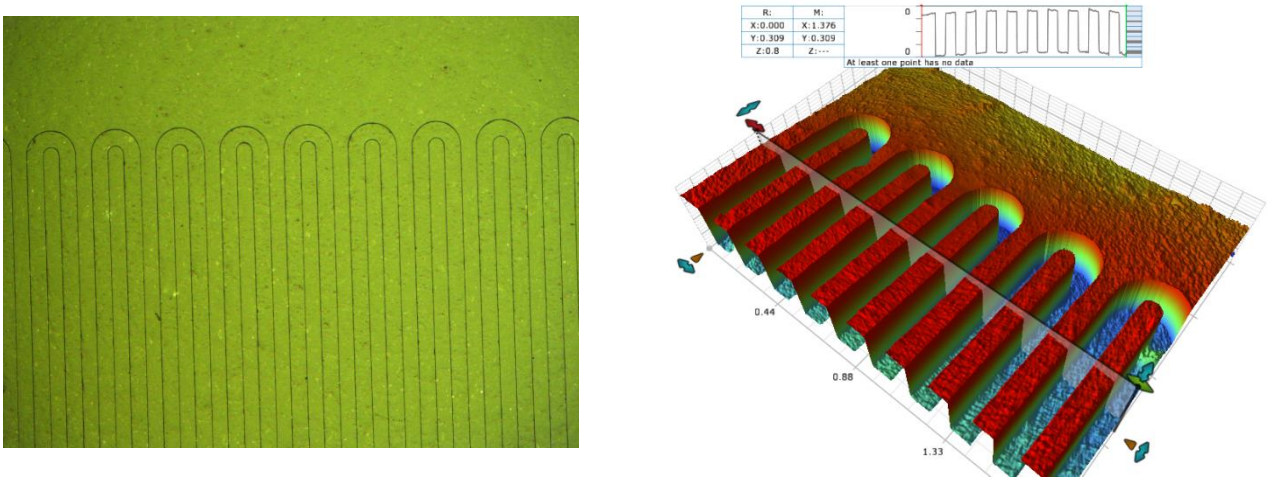

Figure 4-20: Optical microscope image of the serpentine microchannels on the epoxy mould inlay (left) and the optical profile of the microchannels (right).

4.3.2.4: Epoxy insert moulding results

For the first mould run, it was decided that a standard moulding recipe for polystyrene would be used. Although the literature suggests using markedly lower holding pressure than was chosen, it was felt that, for the simple rectangular nature of the mould, the inlay would be able to withstand higher pressures than the more intricate mould inserts used in the literature. Despite the lack of parameter optimisation, the initial results were encouraging. Ten parts were created in polystyrene with reasonably good replication. Images of the moulded parts in polystyrene are given in Fig. 4-21.

The moulding recipe that was used was based on previous research experience using 3D printed plastic inlays. The parameters used are summarised in Table 4-3. The holding pressure is substantially higher than recommended from previous papers (800 bar compared to 200 bar). Since the holding pressure was relatively high, the holding time was comparably lower than values in the referenced epoxy moulding research. A standard melt temperature of 260^{o}C was chosen, with a relatively long cooling time of 35 seconds used to accommodate the low thermal conductivity of the epoxy material.

Table 4-3: Injection moulding parameters used for initial epoxy inlay run.

Moulding parameters	**Units**	**Value**
Injection speed	cm^3/s	1
Holding pressure	bar	800
Holding time	s	5
Injection temperature	^oC	260
Cooling time	s	35
Shot volume	cm^3/s	4
Tool temp	^oC	no heat

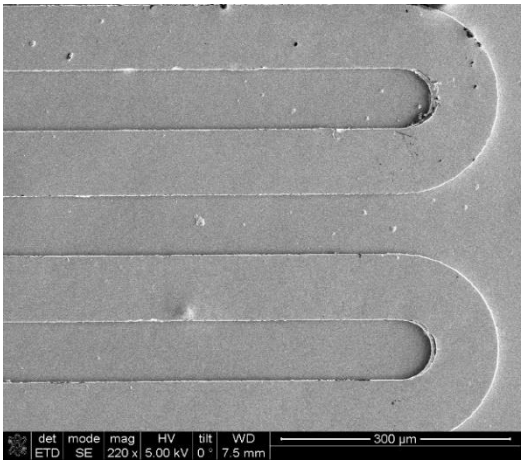

Figure 4-21: SEMs of the microfluidic serpentine pattern in polystyrene. Speckled artefacts are due to re-use of the PDMS substrate at the casting stage.

Although the parts made from the polystyrene replicated the features relatively well, there was evident curvature in the patterns that were moulded. This finding is illustrated in the optical profile in Fig. 4-22. The quoted thermal resistance of the epoxy is in the range of -35 to 220^{O}C. Since the melt temperature is injected into the mould gate at 260^{o}C, it is likely there is some mould distortion.

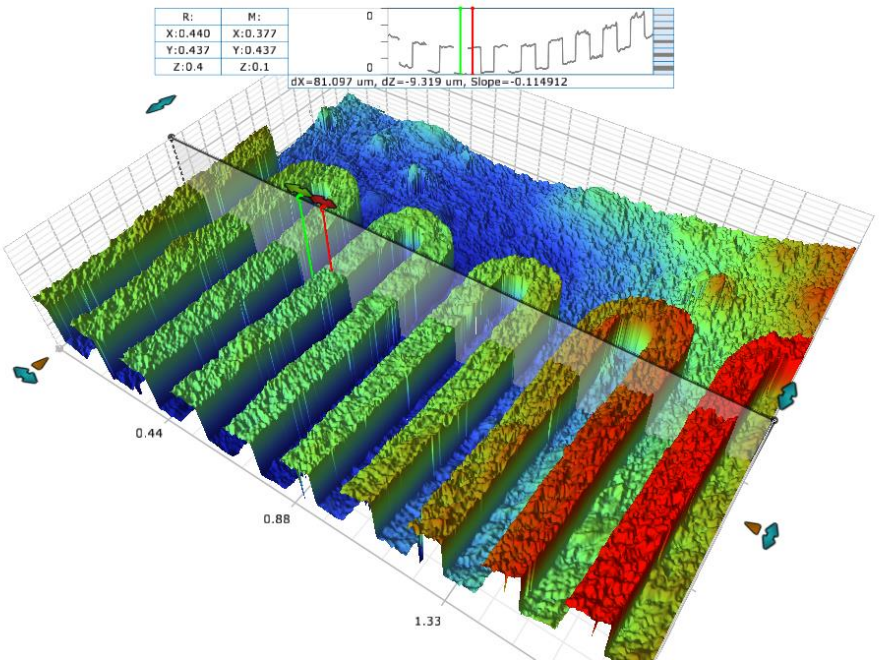

Figure 4-22: Optical profiles of a polystyrene part with a tilt in the patterned face, possibly due to excessive injection temperatures, causing distortion of the epoxy inlay that is translated to the parts.

Since the intention of the project is to use polycarbonate as the testing material, trial mould runs were also performed with polycarbonate. The major difference from using polystyrene is the elevated melt and mould temperatures of 280°C and 80°C respectively. In response to concerns over the flatness of the final parts, different temperatures, holding pressures, cooling times and injection velocities were trialled during mould runs. As previously seen with polystyrene, similar mould distortion was observed for polycarbonate as seen in the optical profiles given in Fig. 4-22. As expected, the individual feature heights varied significantly from the 9.6µm profile for the silicon master. Current moulding work will focus on using lower temperatures as this has been pinpointed as the most likely cause for the distortion.

Higher holding pressures could also be contributing to the mould warpage. According to the datasheet, the maximal pressure the epoxy can withstand is 140 MPa (1400 bar), well below the values used in all mould runs. However, the holding pressures in previous works were around 200 bar, substantially lower than the 600 bar used in this work.

Based on these initial moulding results for polycarbonate, it appears somewhat unlikely that successful replication can be achieved. Alternative moulding materials such as polypropylene have been considered to enable a lower injection temperature that would be less likely to distort the mould. Furthermore, polyethylene could potentially be used due to possessing a substantially lower melting point to materials investigated. Although this approach would have been potentially viable leading to markedly less inlay warpage, the lower strain to failure values for polyethylene (typically around 12%) prevented this approach from being investigated. An optical profile of the inlay after moulding is given in Fig. 2.23: the stitched optical profile over an area of 5 mm^2 in Fig. 4-23 gives a clear illustration of the warping that occurs during the polycarbonate moulding.

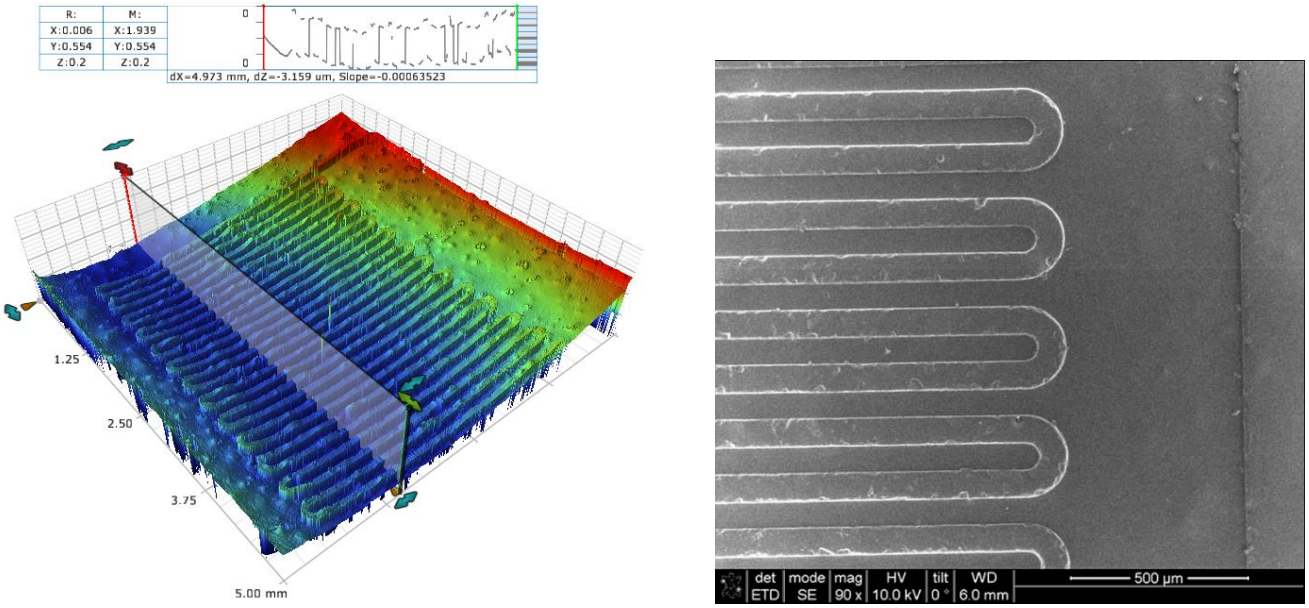

Figure 4-23: Stitched optical profile (5 mm x 5 mm) to illustrate warping (left) and SEM of polycarbonate microfluidic sample at X90 (right).

Since significant part warpage would lead to inconsistency as well as difficulties interlocking micro-structured joints, it was deemed that an alternative approach prioritising geometric fidelity would need to be found. Ultimately, to achieve flat and repeatable micro-structuring, the mould insert would require thermal resistance during the mould cycle.

4.4: Final moulding solution: Micro-imprinting method

4.4.1: Process overview

Next, a final approach was studied and identified as the optimal approach for production of micro-structured interfaces, with high resolution from the initial silicon master to the moulded part as well as boasting high process durability. Due to the promising results obtained, as well as implications for the microfabrication/microfluidic device community, the process was fully characterised.

After master fabrication using the mixed etch process, the insert for injection moulding was fabricated. This was done using an EVG6200 nanoimprint lithography tool. This process was conventionally designed for the production of nanoscale features. Therefore, modifications to the process were required in the form of reducing spinning speeds. This enabled a sufficiently thick layer for the imprinting process. Fig. 4-24 summarises the key phases in the micro-imprinting process. Firstly, a silicon master possessing the desired micro-structuring is produced via dry etching protocols outlined earlier (Fig. 4-24a). Secondly, the silicon master was subsequently covered in an anti-stick layer with EVG working stamp material spun on top of the wafer. As the nano-imprint lithography (NIL) process was originally developed for nanoscale dimensions, it is necessary to adjust spin parameters for a thicker layer. The wafer is then placed in the NIL tool where the working stamp layer (similar to PDMS in properties) is backed by a transparent layer of polyethylene terephthalate (PET), whereby the PET-backing provides the structural support. The PET-Working stamp sandwich is then UV-cured for 10 minutes (Fig. 4-24b), resulting in the inverse pattern from the silicon wafer being formed on the new working stamp-PET sheet The newly imprinted micro-structures can then form the injection

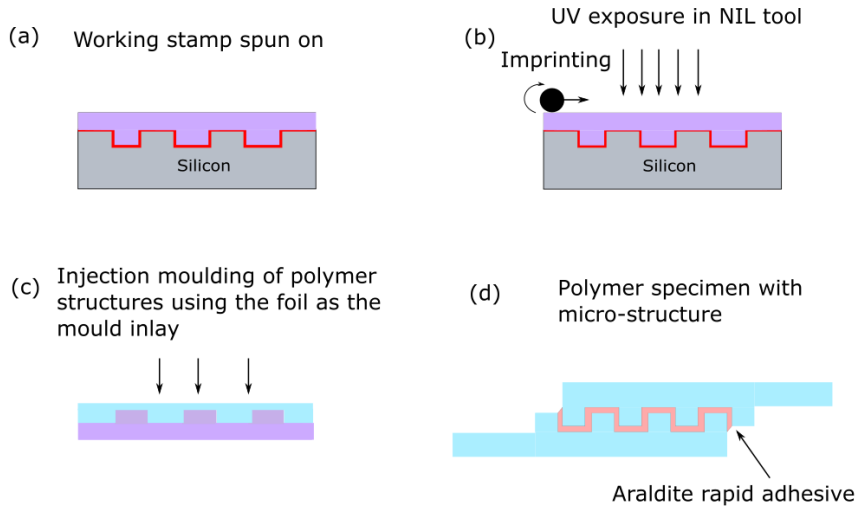

Figure 4-24: Mould inlay fabrication overview: (a) spinning of a working stamp material (purple) on top of the structured silicon master - an anti-stick layer (red) is spun initially to enable separation from the silicon substrate; (b) imprinting of the micro-features from the silicon to the working stamp material, followed by UV curing to solidify the mould insert; (c) injection moulding using the mould insert for the production of micro-structured polycarbonate specimens (blue) and (d) the final interlocking bonded lap joint with Araldite rapid adhesive

moulding inlay (Fig. 4-24c) enabling the production of moulded parts retaining the micro-structure defined in the initial silicon master (Fig. 4-24d).

To quantify the length scales possible to imprint using this approach, a spin curve was created for the working stamp material from spin speeds of 500 rpm to 4000 rpm. The spin curve is given in Fig. 4-25. From the curve it is evident that thicknesses of working stamp above 10µm can be obtained through spin speeds lower than 2000 rpm, speeds of 500 rpm enable a thickness of 90µm to be obtained. If possible, reducing spin speeds lower than 500 rpm is not recommended as the distribution of resist across the sample will have reduced uniformly at the spinning stage. However, since the layer is subjected to the imprinting process, this issue is largely nullified.

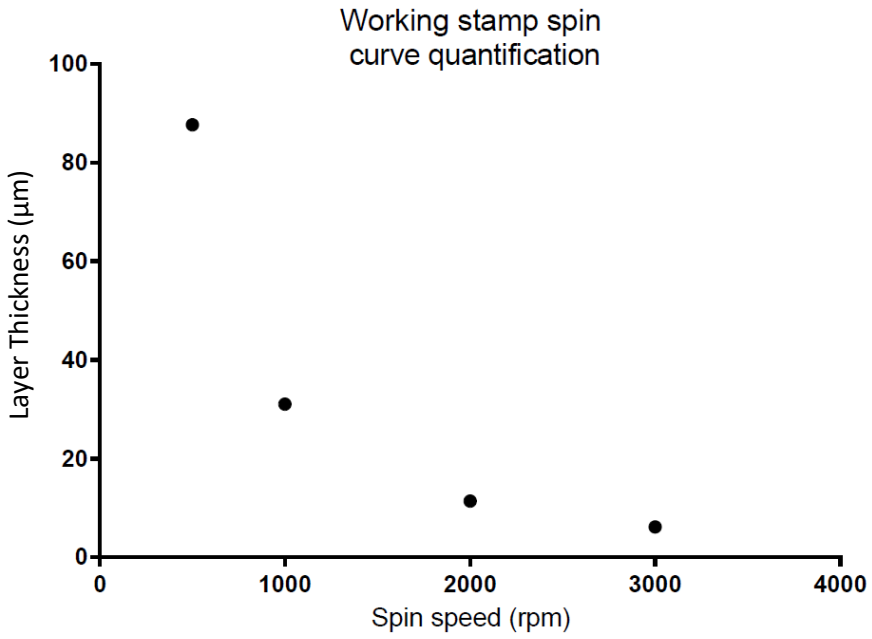

Figure 4-25: Working stamp thickness in micrometres versus spin speed (rpm).

4.4.2: Bosch process etching for moulding

Whilst pursuing a suitable micro-fabrication strategy to produce mechanical test specimens, a secondary goal was to illustrate an innovative strategy to mould parts possessing nano-scale scalloping. A novel aspect of the flexible insert production is the potential to injection mould using the initial silicon master produced via Bosch process etching. The Bosch process is used ubiquitously as a dry-etching methodology within the micro-electro mechanical systems (MEMS) industry. As mentioned previously, this approach entails the rapid alternation between material removal via ion bombardment and chemical passivation to protect the sidewalls from etching. The alternating

aspects lead to the progressive development of a serrated profile as seen in Fig 4-26. The key advantage is the ability to facilitate near-vertical sidewalls.

In this work, an inductively coupled plasma (ICP) tool is used for the dry etch process, with octoflurocyclobutane (C_4F_8) used for the passivation phase and sulphur hexafluoride (SF_6) as the etchant gas. The Bosch process boasts very high etch rates, as well as high selectivity between the photoresist and the silicon. Within the context of injection moulding, the notable disadvantage ascribed to the Bosch process is the alternating phases leading to a scalloped profile as opposed to a smooth surface. This scalloping leads to an etch profile that is not easily separated at the ejection phase of the mould cycle on account of mechanical interlocking between the insert and solidified part.

The hypothesis is that the flexible mechanical properties of the nanoimprinted mould inlay may facilitate successful ejection even of samples possessing nanometre scalloped sidewalls. It is possible that the additional compliance associated with this setup will prevent failure of the serrated polymer during ejection. A comparison of the prospective moulding between smooth, mixed etch profiles and Bosch process produced masters is given bellow in Fig. 4-26.

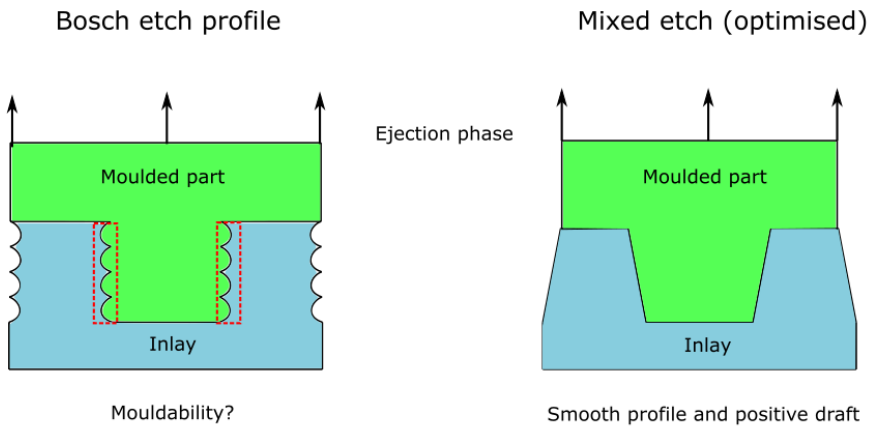

Figure 4-26: Schematic highlighting the interlocking scalloped profile (left) and the smooth sidewall profile from the mixed etch process (right).

This would be highly advantageous within the MEMS community as it would offer the prospect of fabricating ultra-high aspect ratio micro-features with a fully vertical sidewall; compared to the slight draft angle required using the mixed etch process. The fully vertical sidewall would enable greater achievable lateral resolution, permitting greater flexibility and opportunities at the design phase. Within this study, two different etch recipes were utilised. Two different scallop sizes (fine and coarse – see Table 4-4) were employed through varying the relative etching and passivation stages of the dry etch process. Mould inserts were fabricated and were subsequently utilised for injection moulding. Two different etch profiles provide an opportunity to establish whether scallop size has a significant impact on the fidelity of the final parts.

Table 4-4: Key process metrics for the different dry etch recipes used for micro-fabrication. Scallop depth and scallop period are presented as the mean +/- SD. Maximum etch depths were based on the results for the SPR 2207 photoresist used.

	Scallop depth (nm)	Scallop period (nm)	Sidewall angle	Maximum etch depths (μm)
Fine scallop Bosch	284 ±9	875±32	90°	Deep (> 300)
Coarse scallop Bosch	372±18	1238±70	90°	Deep (> 300)
Mixed etch process	n/a	n/a	80°	Moderate (~100)

4.4.3: Injection moulding parameters

As discussed earlier, the major variables that dictate the success of the moulding process are mould temperature, polymer melt temperature, injection velocity, holding pressure and the cooling time for each part. Optimal moulding parameters ensures sufficient filling of the micro-cavities to replicate the geometry from silicon master to polymer part. Polycarbonate was chosen as the polymer throughout for final parts due to suitable mechanical properties for the mechanical testing work. Injection moulding was conducted using an Engel Victory 28 fully hydraulic injection moulding machine. The PET insert was laser cut to the appropriate dimensions to fit within the injection moulding tool. Prior to moulding, the polycarbonate was dried for 2 hours. To ensure high quality parts were produced, the holding pressure was increased until the part did not exhibit shrinkage. Furthermore, the holding time and cooling were incrementally increased to improve the quality of the moulded parts. The optimised parameters are provided in Table 4-5.

Table 4-5: Key Injection moulding parameters used to produce the micro-structured polycarbonate.

Melt temperature (°C)	270
Tool temperature (°C)	60
Injection speed (cm^3/s)	18.3
Holding pressure (bar)	1412
Holding time (s)	8
Cooling time (s)	15
Shot volume (cm^3)	4.5

4.4.4: Process characterisation

To effectively document the efficiency of the fabrication process, samples were characterised to analyse the dimensional variation starting from the initial silicon master, and moving to the imprinted-mould insert and final polycarbonate parts. Measurements were taken for the silicon masters, inlays and moulded parts (Part Number 1, 10 and 20 from each cycle) using optical profilometry (Contour GT, Bruker, US). The key metrics taken were feature heights, feature widths and channel widths. Scans at five distinct locations were taken, with each scan permitting several further measurements to take critical dimensions. Measurements were gathered to compare all the component dimensions across each stage of the fabrication process, enabling the capabilities of the fabrication process to be assessed. Quantification for the moulded components was performed using moulded part numbers 1, 10 and 20 for the process characterisation (optimised mixed process produced master) as well as the Bosch process study.

4.4.4.1: Importance of aspect ratio

A study was conducted to assess the maximum achievable aspect ratios for the micro-imprinting process. The prospect of creating higher aspect ratio devices provides the microfluidic community with greater opportunities during the design phase. A key exemplification of high aspect ratio microfluidics can be seen in the research of Hung et al. [98], where a device was created for culturing cells within microchambers with continuous perfusion of media. To research the spectrum of aspect ratios that could be moulded, a custom acetate photomask was designed with linewidths of 160, 80, 40 and 20 µm. Based on these widths, as well as an intended etch depth of 80 µm for the silicon master, aspect ratios of 0.5, 1, and 2 were produced. The schematic in Fig. 4-27 summarises the key dimensions used for the aspect ratio study. Five scans were taken for the silicon and working stamp entries and five scans were taken for moulded Parts 1, 10 and 20.

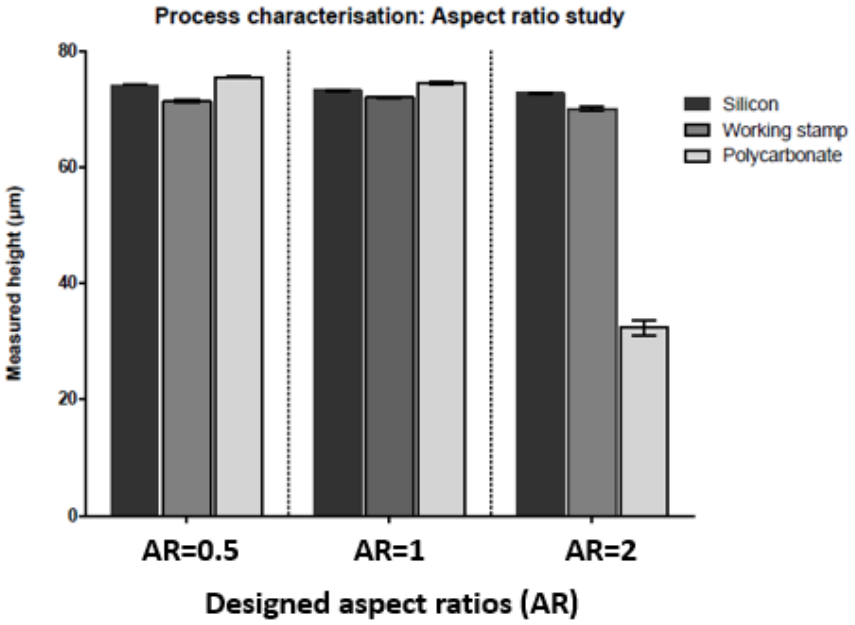

Figure 4-27: Bar chart representing the mean measured feature heights obtained at each successive phase of the micro-imprinting process +/-SD. Entries are categorised into the respective designed aspect ratios (AR) that applied to the silicon master. Five scans were taken for the silicon master, working stamp and moulded part numbers 1, 10 and 20.

Lower aspect ratios of 0.5 and 1.0 were achieved successfully with minimal variation from the initial silicon master. As the aspect ratio was increased to 2.0, the capability to replicate the working stamp height ceased, with a reduction in feature height of approximately 55% relative to the silicon master. There was no evident variation in measured heights as a function of part number, this is highlighted in Table 4-6 indicating that there was no discernible degradation as the mould cycle continues. These results indicate that work on the micron scale should not exceed aspect ratios of 1.0 to guarantee complete replication using the current micro-imprinting protocol. Assessing the aspect ratio results, it can be concluded that the micro-imprinting/injection moulding process outlined is highly applicable for microfluidic device design, provided higher aspect ratio replication is not required. Although, it is possible that further optimisation of the process parameters at the imprinting stage could yield higher attainable aspect ratios.

4.4.4.2: Importance of feature spacing

Feature spacing was studied to ascertain the capability to position channels close together. The ability to successfully produce devices with micro-structures positioned closely is a vital requirement within the microfluidic community as it provides a greater number of analysis features per unit space as well

as enabling more complex microfluidic designs. To ascertain the minimum feature spacing that could be effectively moulded, photomasks were designed with 20 µm linewidths spaced at intervals of 20, 40, 60 and 80 µm. An etch depth of 25 µm was chosen to minimise problems related with large feature depths impacting on the study of feature spacing. Optical profilometry was used to characterise the distance between adjacent ridges relative to the designed size. Fig. 4-28 illustrates the variation in moulded part size relative to the silicon master and working stamp inlay. Five scans were taken for the silicon and working stamp entries and five scans were taken for moulded Parts 1, 10 and 20.

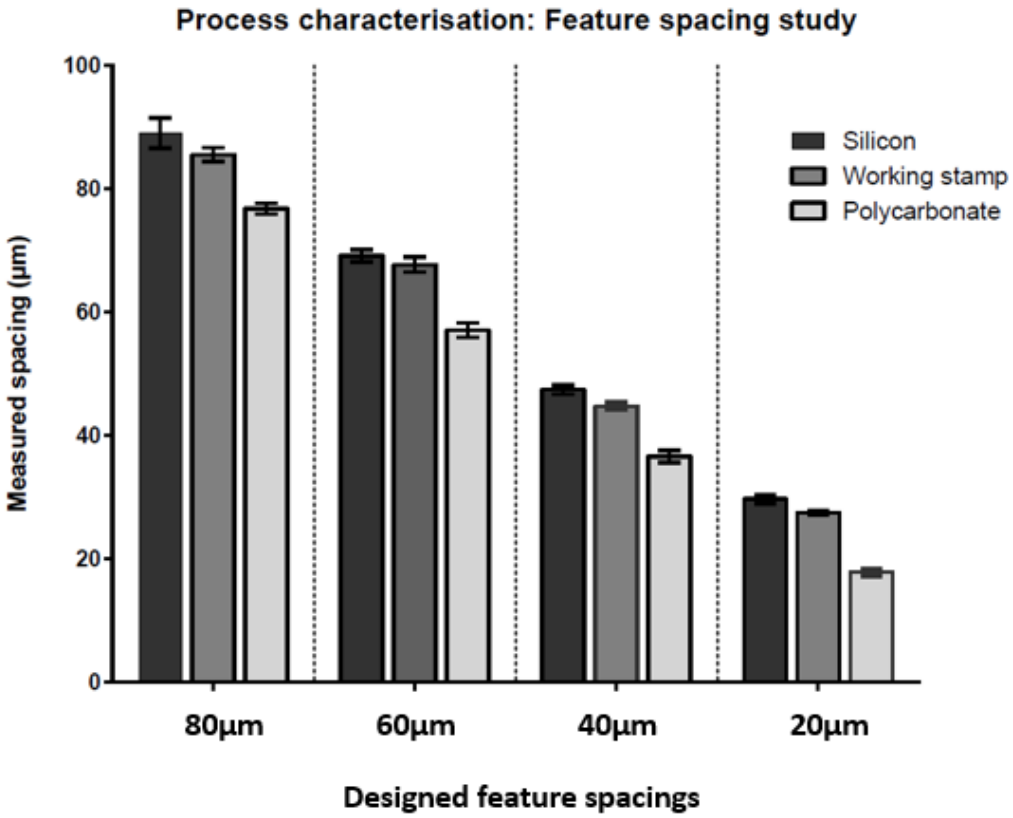

Figure 4-28: Bar chart plotting the mean measured feature spacings for each stage of the micro-imprinting process +/-SD. Entries are grouped into the respective designed feature spacing that applied to the silicon master. Five scans were taken for the silicon master, working stamp and moulded Parts 1, 10 and 20.

From Fig. 4.28, it is apparent that the replicated parts have a reduced channel width relative to the initial silicon master. It is concluded that the reduced channel spacing is due to the elastomeric inlay master flexing under the high moulding pressures leading to enlargement of the moulded features. The same relationship of decreased channel width relative to the silicon master was present for all feature widths studied. Minimal feature variation was observed as a function of part number, this is highlighted in Table 4-6 with the feature spacing measurements remaining consistent from Part 1 to Part 20.

Table 4-6: Mean values (with standard deviations) for the measured feature height in the aspect ratio (AR) study and measured feature spacing (FS) for moulded Parts 1, 10 and 20.

	Measured height (μm)			Feature spacing (μm)			
Measurement	AR=0.5	AR=1	AR=2	FS=80	FS=60	FS=40	FS=20
Part 1	75.5 ± 0.11	74.4 ± 0.25	32.4 ± 1.31	76.8 ± 0.88	57.0 ± 1.2	36.6 ± 0.98	17.8 ± 0.65
Part 10	76.6 ± 0.47	74.7 ± 0.26	32.6 ± 1.16	76.7 ± 1.17	57.8 ± 0.70	36.8 ± 0.70	17.8 ± 0.73
Part 20	75.5 ± 0.23	74.7 ± 0.32	30.7 ± 0.55	76.2 ± 0.96	57.8 ± 1.21	36.6 ± 0.82	17.6 ± 0.39
Mean	75.9 ± 0.27	74.6 ± 0.28	31.9 ± 1.00	76.6 ± 1.0	57.5 ± 1.04	36.7 ± 0.83	17.7 ± 0.59

Results convey that narrow feature spacings can be consistently replicated with spacings as low as 17.8 μm between features successfully moulded. Since lateral resolution was limited due to the use of acetate photomasks, it is hypothesised that significantly smaller feature spacing can be successfully imprinted and moulded using a glass photomask. Since the imprinting process is conventionally implemented for nano-scale applications, imprinting for lateral resolution appears to be more facile than high aspect ratio fabrication. These findings indicate that the micro-imprinting process is highly suitable for the development of narrowly positioned micro-structures. For most microfluidic applications, it is less essential to fabricate large aspect ratios, whereas the capability to produce narrowly spaced features is imperative for microfluidic device fabrication.

4.4.5.Bosch process injection moulding

4.4.5.1: Process durability

Conventionally, injection moulding involving samples created through the dry etch process require the mixed etch profile because the nanometre scalloping leads to an inability to separate the moulded part from the silicon master due to interlocking of the mould/tool interface. Successful moulding from silicon etched via the Bosch process would be highly valuable for the microfluidic community as it would reduce the dependence on dry etch expertise due to the easier development of Bosch etch recipes compared to the more variable mixed process etch recipes.

It is hypothesized that, in the current study, it is conceivable for the moulded part to detach smoothly at the ejection phase owing to the greater compliance associated with the PET-supported inlay. Through having a higher compliance than stiff metallic mould inserts, it was speculated that, during the ejection stage, the part would have a greater chance of separation. Samples were moulded using an initial silicon master depth of 35 µm with Part numbers 1, 10 and 20 characterised using SEMs and optical profilometry to determine the quality of the parts as the process progressed. Cross-sectional SEMs were taken for Parts 1, 10 and 20 to assess the durability of the process as well as quantifying the success of the mould ejection phase of the process. Fig. 4-29 conveys the degradation of the moulded parts from Part 1 to Part 20 for the two Bosch etches (large and small-scale scalloping) as well as the mixed etch process serving as a control experiment.

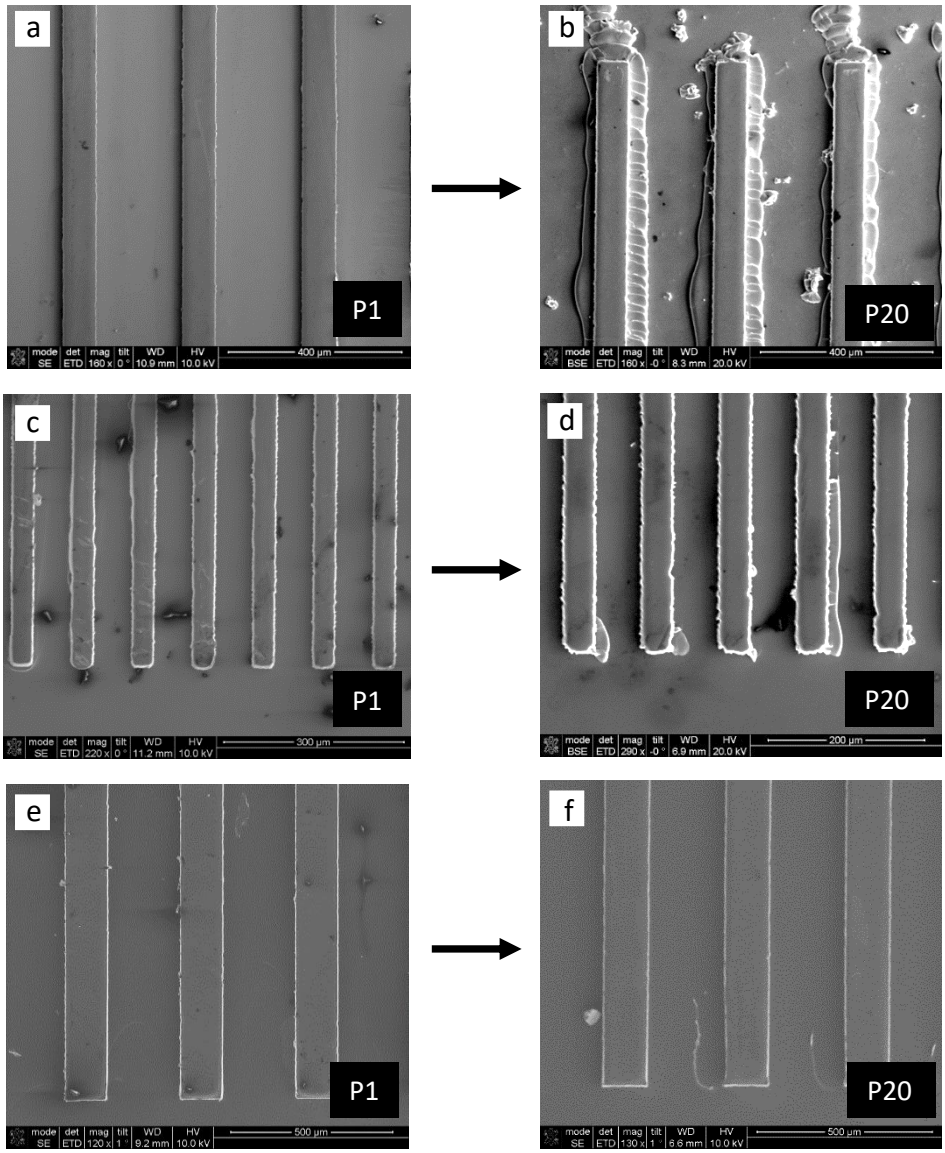

Figure 4-29: Inlay deterioration study. Low magnification SEMs to examine inlay deterioration as moulding progresses. Arrows signify the progression of the mould cycle from Part 1 (P1) to part 20 (P20): (a) and (b) show top-down images of Parts 1 and 20 moulded from the Bosch process produced master with coarse scalloping, respectively. (c) and (d) show Parts 1 and 20 moulded from the Bosch process produced master with finer scalloping, respectively and (e) and (f) act as control experiments, showing top-down images for Parts 1 and 20 moulded from inserts produced using the mixed process – these show minimal damage.

From the images in Fig. 4-29a-d, it is apparent that there is progressive worsening for the Bosch process produced components. Comparing the images in Fig. 4-29b and Fig. 4-29d, the finer scalloping (Fig. 4-28d) led to a lessening of the deterioration of the moulded parts relative to the coarser scalloped parts. For both etch methods, it was seen that, as the moulding progressed, the overall part quality declined, specifically at the intersection between the bottom portion of the sidewall and the inlay substrate. This was credited to progressive damage occurring within the mould inlays with

scalloped sidewalls due to greater localised stresses involved in the ejection of the interlocked polymer/insert interface. This deterioration did not seem to have a major effect on the measured depths of the features, with the damage leading to surplus polymer becoming present within the channels of the parts. These results signify a partial success in moulding using the Bosch process since parts could successfully be separated from the mould inlay, although the interlocking of moulded part and inlay accelerates deterioration - hindering the manufacture of high-quality parts.

4.4.5.2: Successful part ejection

All parts moulded employing the Bosch process produced inlays were successfully separated without notable difficulty. In addition to observing general part quality, retention of the nano-scale scalloping in the moulded parts was considered a key barometer for successful Bosch process injection moulding as the transfer of the nanometre scalloping in the moulded parts illustrate successful ejection of the part from the mould insert without any discernible damage. SEM images in Fig. 4-30a and Fig. 4-30b confirm that scalloping is indeed present in the tenth moulded part for both the finer and coarse scalloping cases, respectively.

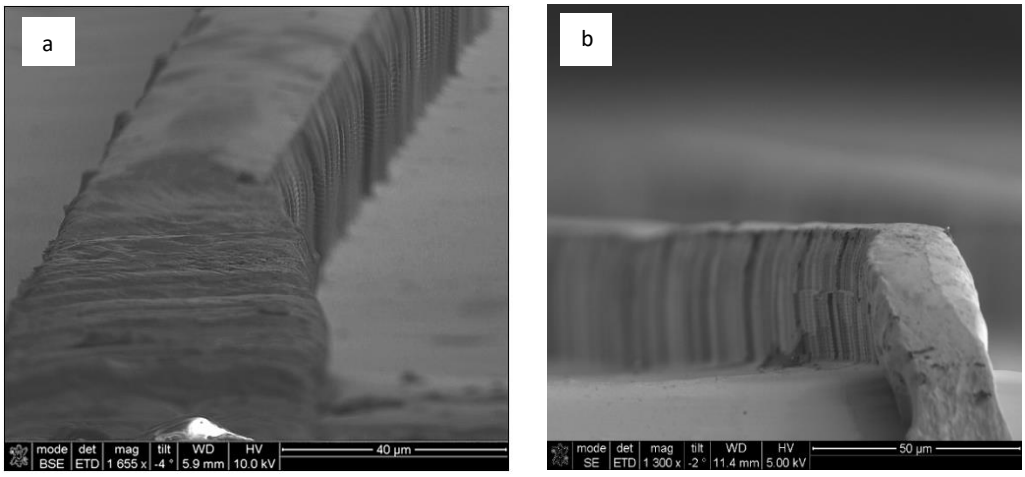

Figure 4-30: Cross sectional SEMs (in tenth moulded part) to confirm scallop retention: (a) fine scalloping and (b) coarser scalloping.

Referring to Fig. 4-30a and Fig. 4-30b, the presence of scalloping indicates that successful mould/inlay separation using the Bosch is feasible. Although it has been proven that moulding can be achieved utilising the Bosch process as the master, it remains substantially less optimal relative to the mixed process results shown earlier due to the more progressive damage indicated in Fig. 4-29. Thus, it is

recognised that a substantial amount of optimisation would be required before this approach could be considered as a prospective option for microfluidic design.

4.4.6: Microfluidic device fabrication: proof of concept

To showcase the suitability of the process for microfluidic-based work, a microfluidic device was designed and produced with acetate masks using the optimal mixed etch process. An image of the photomask design is shown in Fig. 4-31a and the image in Fig. 4-31b represents a scanning electron micrograph (SEM) of the moulded serpentine channel. Table 4-7 provides a summary of the measured channel lengths relative to the initial designed lengths (channel measurements were taken at five locations across the device).

Table 4-7: Comparison between the designed and measured dimensions for the serpentine channel width and inner radius size alongside the standard deviations.

	Design	Measured	SD
Narrow width (µm)	100	90.5	0.7
Inner radius (µm)	50	43.7	0.78

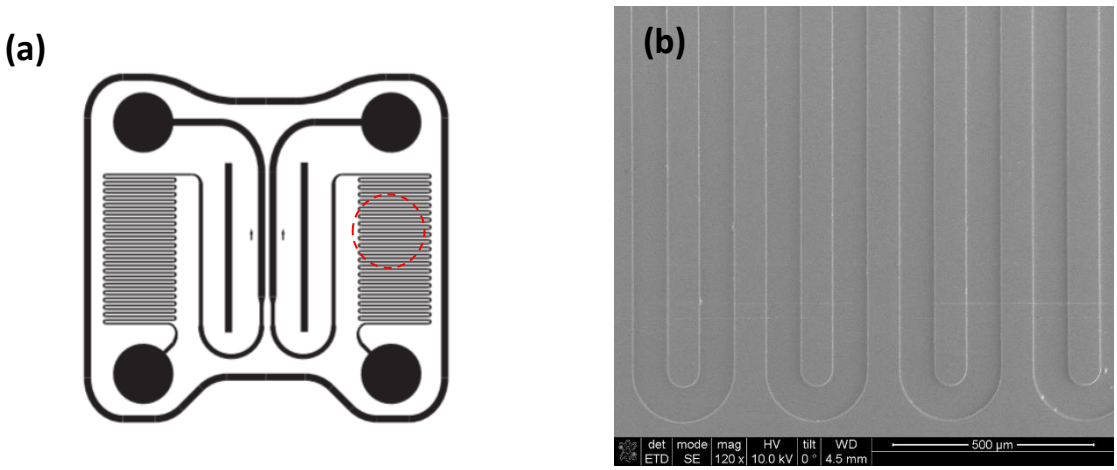

Figure 4-31: (a) Schematic of microfluidic device design alongside (b) a top-down SEM image taken of the moulded serpentine channels. The circled region in (a) signifies the region of interest shown in (b).

The sample had a measured mean channel width of 90.5 µm and a mean inner channel radius size of 43.7 µm. The mean height was measured as 9.44 µm, although height was not of primary concern in this case of low aspect ratio production. The SEM image in Fig. 4-29b validates that the imprinting process was particularly successful at replicating the network of serpentine channels. Therefore, this

proof-of-concept work highlights that complex microfluidic designs are readily produced using the hybrid inlay process.

4.5: Conclusions

The first critical objective outlined at the beginning of this thesis has been the successful production of micro-structured interfaces for use in mechanical testing applications. This work has entailed the investigation into various different resists and etching options to attain suitably high etch depths (>50µm) with the positive tone resist SPR 2207, identified as the most effective resist with appropriate resist thickness, exposure times and resists development times optimised to ensure appropriate resistance during the dry etching phase of the works.

The silicon fabrication provided the foundations for later fabrication where it became apparent that polymers would be the optimum choice for the remainder of the project. Through a period of comprehensive research, new approaches have been explored to develop a mould inlay for micro-injection moulding, conferring sufficient geometrical replication and durability for several injection moulding runs, ensuring that the elevated temperatures and holding pressures could be reliably withstood. Initial approaches utilising the back-side exposure of SU-8/TOPAS 5013 interfaces and WEICON C epoxy/PDMS casting were promising although resulted in premature deterioration of the interface and notable part curvature during mould cycles.

The final mould inlay objective was satisfied using a micro-imprinting process in tandem with injection moulding, where parameters have been sufficiently optimised to ensure complete filling of the micro-cavities. This process has been shown to retain feature fidelity from the initial silicon master whilst boasting the durability that is necessary for the injection moulding of suitably high sample numbers. Results have illustrated that feature spacing as low as 20µm could be reliably replicated as well as complex serpentine channels with marked feature curvature. Aspect ratio quantification illustrated that AR=1 could be feasibly obtained with higher aspect ratios proving challenging from a mould-filling perspective. Finally, the use of a flexible injection moulding inlay provided a unique means to injection mould utilising BOSCH process produced masters, providing an alternative to using the less standardised mixed etch recipes that have previously been required for micro-injection moulding.

Chapter 5 Experimental testing of micro-fabricated single-lap joints

Chapter overview

Moving on from the fabrication work, this chapter covers the mechanical test results obtained from testing the micro-fabricated interlocking joints. The testing is divided into separate sections documenting the results initially using silicon wafers as the adherend material and then moving on to results for polycarbonate joints produced via micro-injection moulding. The chapter begins with an overview of the micro-tensile testing machine used in the work as well as the bespoke test rig designs implemented to perform single lap joint testing.

5.1: Micro-tensile tester and test rig design considerations

To test structured lap joints, a suitable test rig had to be designed to successfully integrate into the Deben micro-tester shown in Fig. 5-1. This test machine is intended for testing of small dog-bone specimens with a maximum force of 5kN. Testing can be performed using tensile, compression or cyclical loading. Additionally, the rate of applied displacement can be varied from 0.1mm/min to 1 mm/min.

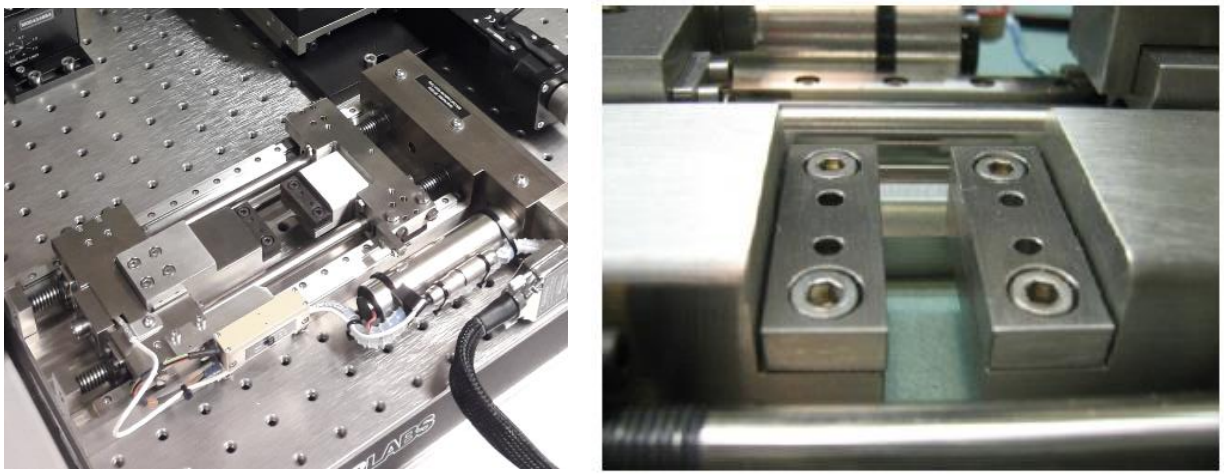

Figure 5-1: Photographs of Deben micro-tester. Entire tester setup shown (left); close-up image of the tensile clamping jaws for dog-bone specimens (right).

As can be seen in Fig 5-1, the clamping fixtures are specific to dog-bone specimens. They have a maximum relative inter-jaw distance of 40mm (20mm extension plus 20mm clearance between clamping jaws). To enable testing of lap joint specimens the loadcell and gearbox fixtures had to be removed and replaced with a new system to successfully test lap joint specimens, because the fixtures required needed to be substantially larger than the inter-jaw distance. Furthermore, a key point to address is the ability to image the bond-line during tests to accurately obtain strain data, as well as aid in explaining the underlying physics of the interlocking geometries. This would require the test rig to be designed in such a manner that the lap joint is fixed 'side-on', where the horizontal length of the side face of the adherends can be directly imaged via optical microscopy. A final key consideration was to ensure that the vertical centre of loading within the joint did not deviate from the original clamping setup; this would ensure that the force values measured via the loadcell were correct. The value quoted for this distance was 2.8 mm above the original jaws. The schematic in Fig. 5-2 illustrates this point.

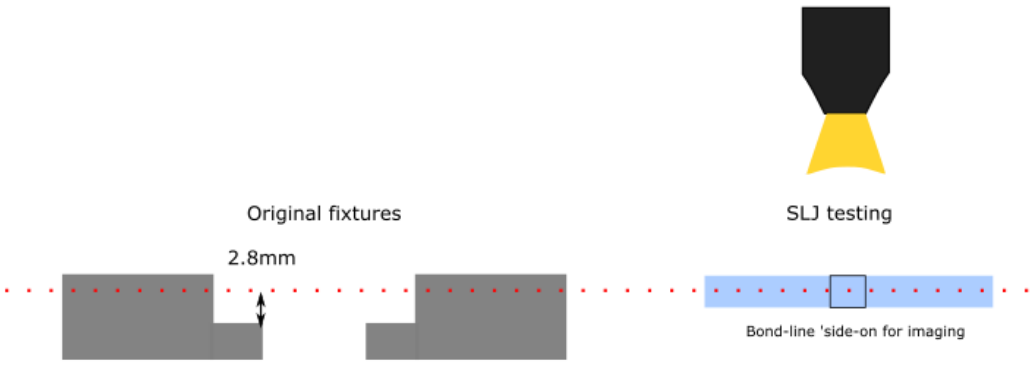

Figure 5-2: Schematic of the vertical position of the load-cell centre line projected from the original tensile clamping fixtures (left) and the extrapolation to ensure SLJ test is conducted at the same position (right) whilst enabling imaging of the bond-line.

The micro-test module interfaces with acquisition software that enables control of the test-rig as well as providing a means to display the force-extension data. These design considerations as well as limits imposed through material choice were addressed in the test rig designs used throughout the work. Details specific to each test rig design are given in the following sections separated into silicon and polycarbonate testing respectively.

5.2: Silicon adhesive joints

5.2.1 Testing protocol

As a starting point, it was deemed logical to use the silicon as an initial test material, owing to the relatively straightforward fabrication process (i.e. in the microfabrication world, surface patterning is generally first achieved in Silicon). After some preliminary experimentation with different pattern geometries, it was apparent that feature clearance had a pronounced effect on the failure loads on specimens. Therefore, the first full set of testing was performed with two very distinct interlocking setups shown in Fig.5-3.

The feature sizes chosen for the mechanical testing were separated into three categories:

(1): 150 µm features with 450 µm grooves (wider clearance of 300 µm for interlocking)

(2): 270 µm features with 330 grooves µm (narrower clearance of 60 µm for interlocking)

(3): Planar unstructured silicon as a control baseline

The etch depths chosen for the structured specimens were arbitrarily chosen to be 70 µm. This was deemed a suitably large depth to ensure features could be effectively interlocked. The profile heights, as well as lateral dimensions, can be seen from the summary schematic in Fig. 5-3. The silicon specimens were 525 µm thick; the bonding area was 7.5 mm^2 and the specimen length was 40 mm.

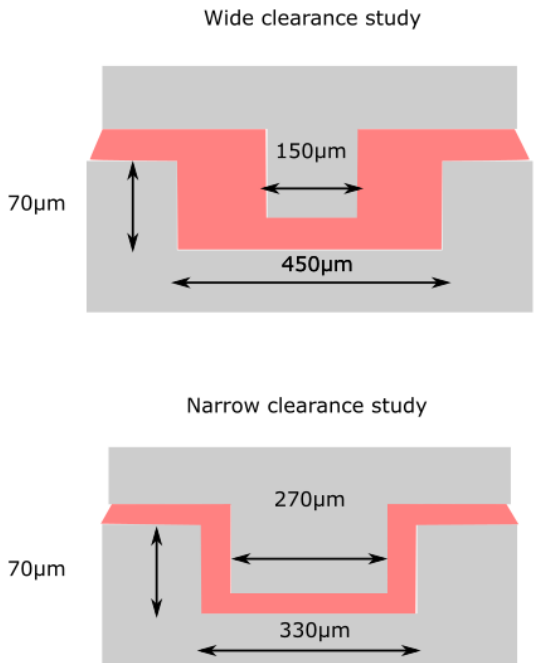

Figure 5-3: Schematic indicating the two interlocking setups used for the mechanical testing with the defining geometries. Top image depicts the wider clearance setup; bottom image illustrates the narrower clearance interlocking setup.

The two-part epoxy, Araldite Instant was chosen as the adhesive, with curing time of 4 hours at room temperature applied based on the datasheet. Material properties derived from tensile testing of the adhesive are given in Table 5-1.

Table 5-1: Material properties for the Araldite rapid adhesive obtained via tensile testing of standard dog-bone samples.

E (GPa)	UTS (MPa)	ε (failure)
0.49 ± 0.06	6.3 ± 0.65	0.29 ± 0.04

5.2.2 Test Rig design for silicon

Although silicon is ideal for producing very accurate surface patterns, there is a major problem for realising and testing silicon joints. Based on the brittle nature of silicon, as well as the low thickness of samples (525µm from the silicon wafer thickness), it was hypothesised that obtaining meaningful data would be problematic as it was thought that the silicon would fail prematurely in the bulk prior to the failure of the adhesive bond. The thickness issue was further compounded by the eccentric loading profile of the single lap joint. During tensile loading, a bending moment is induced within the joint leading to the adherends deforming to align to the loading path. In response to this, a setup was devised to largely prevent adherend bending to promote an exclusively shear strain response. Solidworks images of the rig design are given in Fig. 5-4. The rig was designed in which the silicon would be bonded to much thicker aluminium components to alleviate the bending moment concerns. The back-side of the silicon was bonded across its entire length to the aluminium (see Fig. 5-5), fixing the lap joint within the micro-tester. Since the bonding area of the silicon-aluminium interface is substantially greater than the silicon-silicon interface, failure should always initiate at the bond-line instead of within the bonded area to fix the joint in place. An image of the silicon test rig in-situ is shown in Fig. 5-6. Interlocking of the joints was achieved through manual assembly of the interlocking profiles. This entailed applying adhesive and aligning the square wave features together, with an evident degree of interlock manifested through experience and the clear ability for the interface to transmit load via the interlocking introduced via the micro-features. It should be noted that owing to the varying clearances utilised across all tests there exists a degree of variation during the assembly process, although this was mitigated as much as possible through repeated trials and user experience during the assembly process.

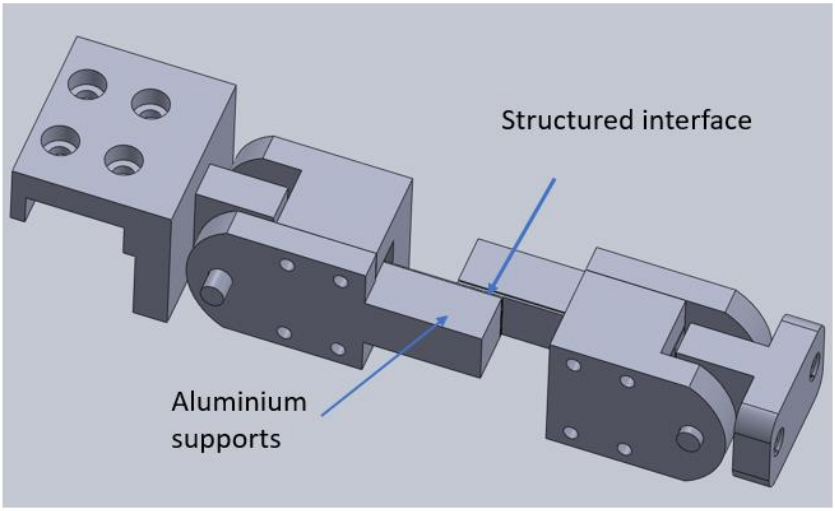

Figure 5-4: Test rig design with the Aluminium supporting components.

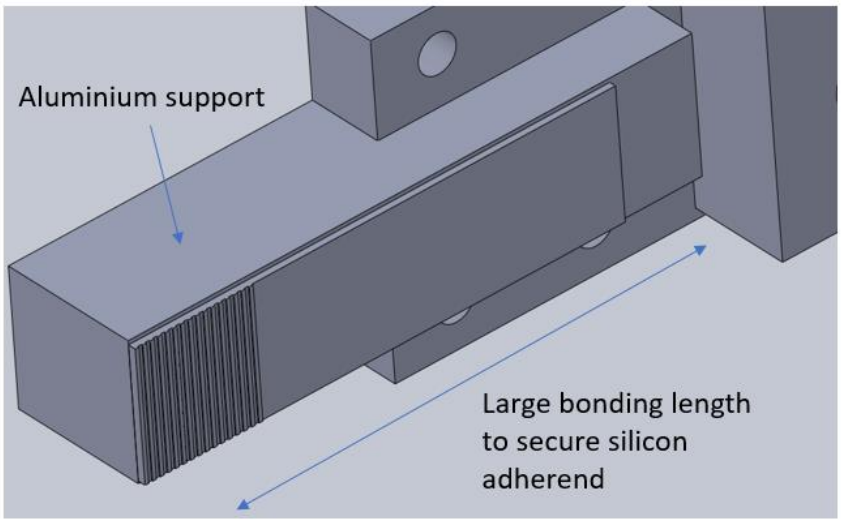

Figure 5-5: Solidworks image of a structured silicon adherend bonded to the aluminium support (the other adherend is removed for clarity).

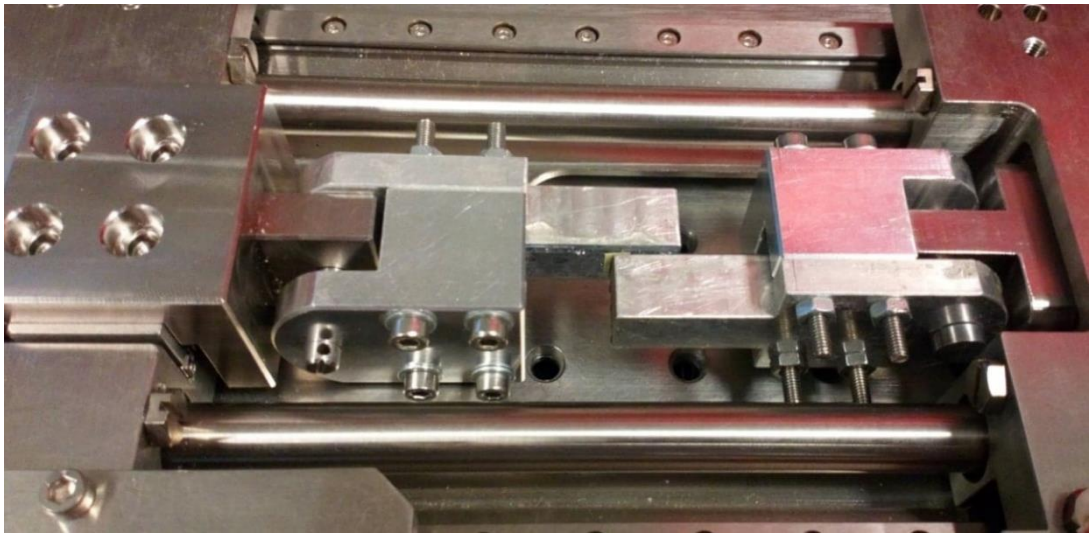

Figure 5-6: Test rig integrated into the Deben micro-tester. Original fixture is replaced with pin-based fixtures to rotate the test setup for imaging as well as enabling horizontal movement when assembling the test setup

5.2.3 Mechanical test results

5.2.3.1: Planar samples

Four tests were conducted for each adherend setup with a motor speed of 0.5mm/minute. The force-extension graphs for the planar samples, narrow clearance samples and wider clearance samples are given in Figures 5-7, 5-8 and 5-9 respectively. Additionally, photographs were taken to elucidate the failure mode for the specimens, these are shown in Fig. 5-10. It should be noted that the large extension readouts from all graphs include the extension of the test rig as localised strain data was not collected for the silicon specimens. The highly stiff and brittle nature of the silicon joint in tandem made taking localise strain data difficult, therefore the focus of the testing was to determine the strength properties conferred through the structured interface. Although localised strain measurements could have been measured via imaging techniques such as DIC, it was determined that the silicon testing would largely be utilised as proof of concept tests, with more detailed strain-based analyses implemented in future tests utilising alternative adherend materials.

For the planar tests, there were two modes of failure observed. Firstly, there was a conventional adhesive-based failure where the silicon adherends remained intact. The second failure mode occurred with bulk adherend failure at the edge of the joint with the interface intact. This can be attributed to the highly brittle nature of the joint as well as the high peak stresses leading to a high susceptibility to bulk failures. The large variability observed for the stress-extension plots was attributed to the highly brittle nature of silicon. Since crystalline silicon has a catastrophic failure properties, any deviation from perfect, collinear test rig alignment was highly susceptible to bulk

failures with adhesive failures likely only occurring whereby no deviation from collinearity was present during tensile loading.

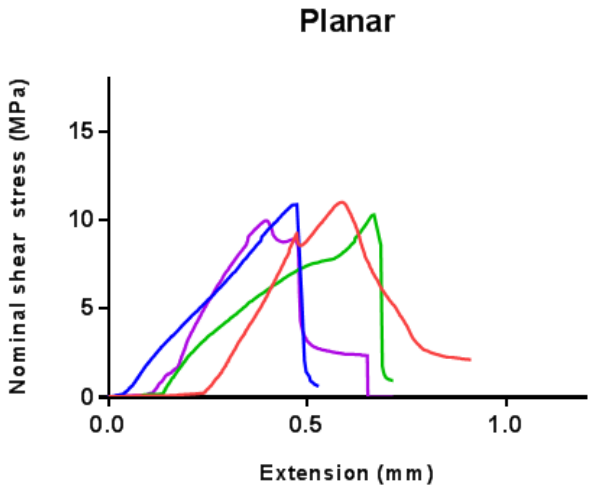

Figure 5-7: Stress-extension data for the unstructured planar samples, each entry represents a repeat test.

5.2.3.2: Narrow clearance structured joints

The force-extension graphs for the narrow fitting structures are given in Fig. 5-8. During the course of the test, progressive drop-offs in load were evident. At these points in the tests, there was audible cracking within the joint signifying that localised fracturing of the silicon had occurred. Due to the implementation of the supporting structure, the load was able to persist up to a critical point where crack propagation leads to failure. The failure mode observed for all narrow clearance samples was bulk failure.

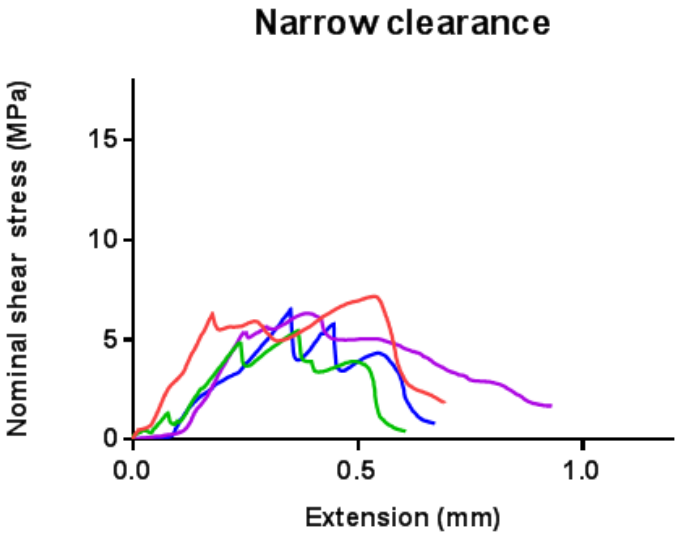

Figure 5-8: Force-extension graph for the narrow clearance adhesive joints. The extension is given as the absolute extension in mm; force is given as Newtons (N). Several drop-off points in force indicate fracture within the silicon prior to the final failure of the interface.

5.2.3.3 : Wide clearance structured joints

The force-extension graphs for the wide fitting structures are given in Fig. 5-9. The same drop-off behaviour was observed as for the narrow clearance category with bulk failure occurring for all test groups. The failure modes discussed for all test setups are given in Fig.5-10.

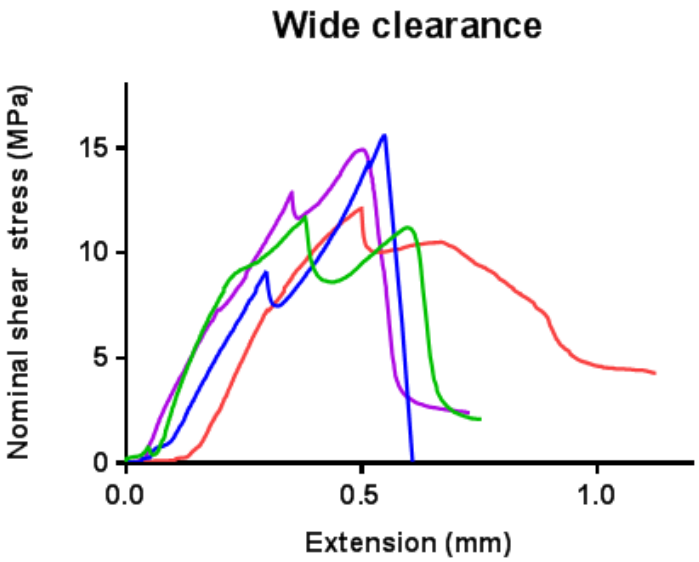

Figure 5-9: Force-extension graph for the wide clearance adhesive silicon joints. The extension is given as the absolute extension in mm; force is given as Newtons (N).

Figure 5-10: Photographs of the two failure modes observed during the planar testing. The image on the left illustrates the bulk failure of the silicon with the bonded interface remaining intact. The image on the right indicates the shearing of the adhesive layer, leading to the more conventional adhesive failure typically observed.

The average failure stresses of the three bonding setups were calculated along with the standard error, these are given in the bar graph provided in Fig. 5-11.

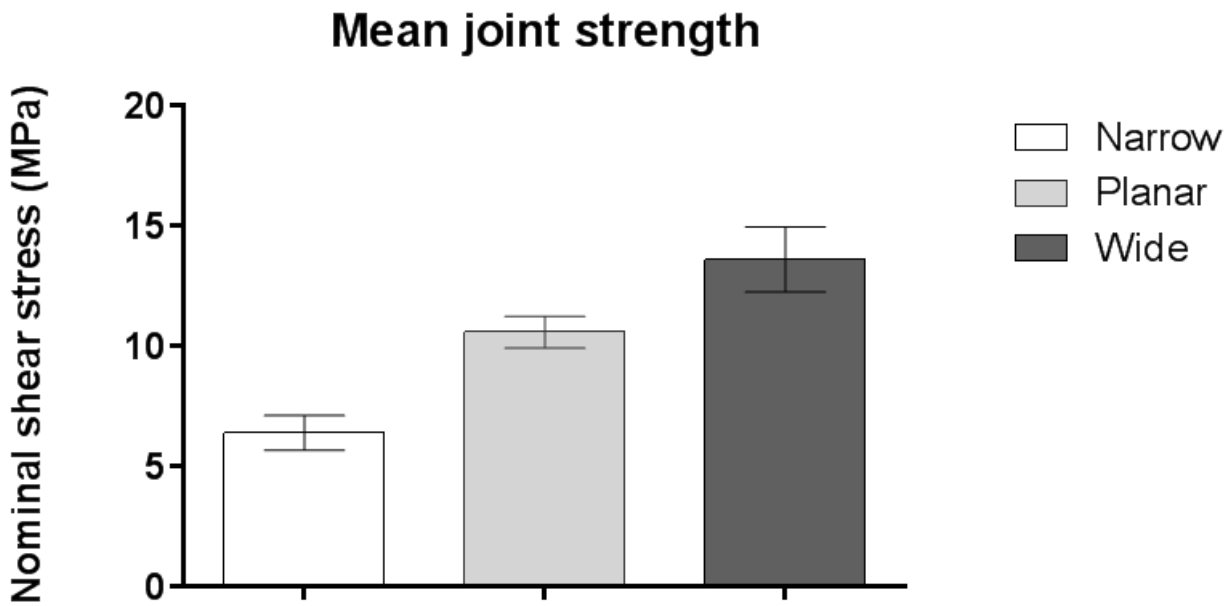

Figure 5-11: Chart of the average failure loads (in MPa) observed for: the narrow clearance tests (white), planar tests (light grey) and the wider clearance tests (dark grey) alongside error bars ((+/-SD).

5.2.3.4: Discussion

From the graph in Fig.5-11, a definite trend can be seen when comparing the average failure stresses for each group. The lowest failure stresses were consistently observed for the narrow clearance samples with a mean failure stress of 6.38 MPa. The failure stresses for the unstructured, planar joint exhibited an improved performance with a value of 10.57 MPa. The wider clearance samples resulted in the greatest mechanical response with an average failure stress of 13.60 MPa.

This results illustrate that, within the context of an extremely brittle adherend material, tight fitting, stiffer bonded joints fail at substantially lower loads relative to unstructured; whereas less stiff, wider fitting joints outperform the unstructured specimens. All specimens fractured at the edges of the bond-line; the region of the bonded interface under the highest shear stress, as corroborated by analytical solutions. The overriding observation from all interlocked testing is clear: the bonded interface was never the point of failure. This point indicates that the bonded region has greater

strength than the failure loads recorded, limiting the use of silicon to obtain test results that explain the impact of the micro-structured interface.

A significant limitation to analysing the reasons behind these findings is the inability to image the bonded interface. This becomes apparent when the transmission spectrum for silicon is considered in Fig. 5-12.

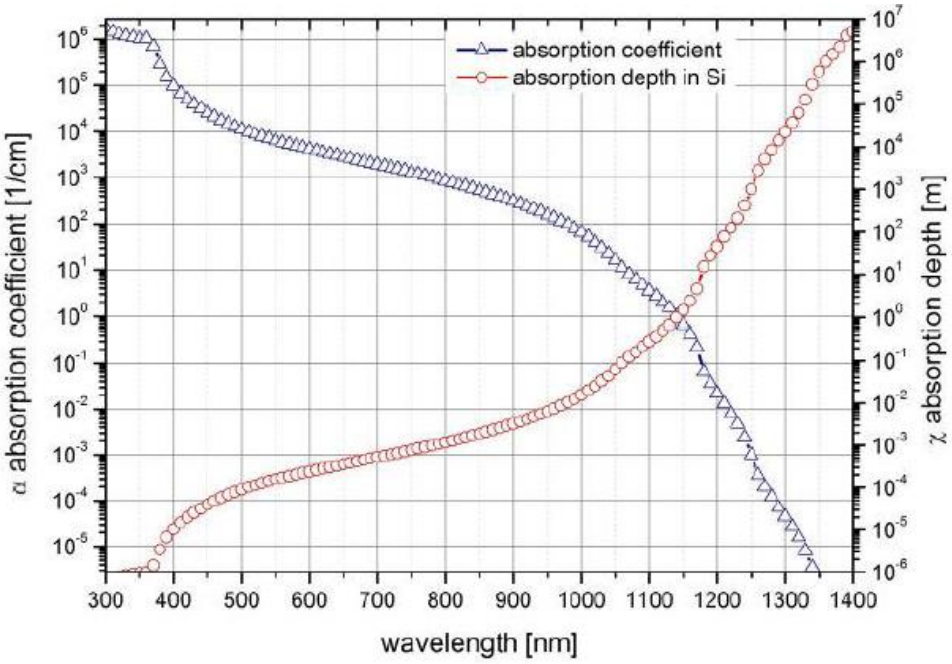

Figure 5-12: Graph showing the absorption coefficient (1/cm) and absorption depth (m) for silicon plotted against wavelength (nm). Image from reference [75].

The absorption coefficient for silicon is considerably higher for shorter wavelengths in the visible spectrum (400-700 nm). This correlates to a very small absorption depth within the material, with very little light being transmitted for imaging purposes. As the wavelength increases, the absorption coefficient decreases substantially as the infrared (700 nm and greater) region is approached. The inability to image the bond-line during the tests severely restricts analysis of the silicon failure [99]. Additionally, modelling of the silicon failure in FEA software such as ABAQUS would prove difficult based on the brittle nature of silicon.

5.2.3.5: Conclusions for silicon testing

The silicon testing provided a useful initial platform for the experimental testing work within the project. Although the average failure load results illustrated that the increase in active bonding area can lead to improved bond strength, the brittle nature of silicon combined with the stress concentrations imposed via micro-structuring had the potential to hinder performance leading to premature bulk failure. This stage in the research signified a turning point, and the remaining work focussed on strategies to combine micro-fabrication and injection moulding to enable the testing of polymers. By testing using ductile polymers, it was hypothesised that the tangible advantages of micro-structuring would be showcased more efficiently than in the present case (in particular, the idea that strong tough joints could be made that would not suffer from brittle bulk failure).

5.3: Polycarbonate adhesive joints

5.3.1: Advantages of polymer testing

Reflecting on the results for the silicon testing, it became apparent that a more ductile material would be required to fully assess the implications of a micro-structured interface. Additionally, since silicon could not be imaged effectively using microscopy, the sole information available to analyse the results was mechanical test results and the failure modes. Hence, although this result is indicative of the potential mechanical benefits of a micro-structured interface, alternative materials will be proposed for the work, ideally having the following attributes:

- Transparent to visible light to image the bond-line during testing
- Ductile to illustrate that the structuring can confer strength as the adherends yield
- Short fabrication time to expedite the testing of different geometries
- High throughput to produce numerous samples as opposed to the restrictions associated with ‘one-off’ silicon wafer fabrication

As discussed in Chapter 4, a micro-imprinting/injection moulding protocol was developed to produce polycarbonate adherends. Polycarbonate is strong, tough and can be injection moulded. Thus, it was the material of choice for the remaining tests within this chapter.

5.3.2: Preparation of joints

During the bonding of samples, an overlap length of 7.5 mm was implemented to produce a bonded area of 7.5 mm x 7.5 mm. For the structured interfaces, the entire bonding area is structured with square-wave micro features. Bonding was performed using a 2-component epoxy, Araldite Rapid with a curing time of 4 hours at room temperature, in accordance with the manufacturer's guidelines [100]. For the structured joints, the interlocking of adherends required a significant level of user expertise in ensuring that the two structured parts were truly interlocking, with samples correctly aligned and positioned at full interlock. The quality of the interlock was verified later using an optical microscope. Fig. 5-13 shows the three key geometries: feature depth *D*, feature width λ_f, channel width λ_c and total horizontal clearance *c*.

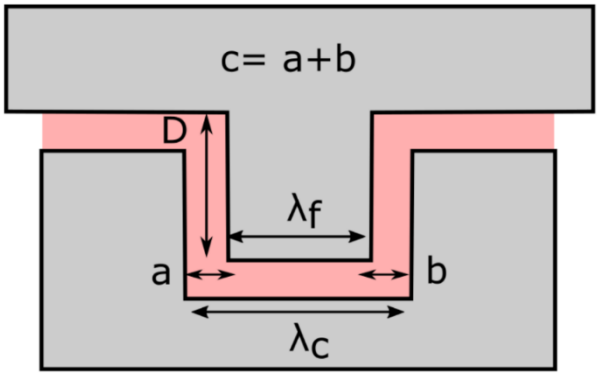

Figure 5-13: Schematic showing single interlocking feature with polycarbonate (grey) bonded by adhesive (pink): D denotes feature depth, λ_f denotes feature width, λ_c denotes channel width, a and b denote clearance at each side of the feature and C denotes total clearance.

Three distinct feature clearances and two different feature depths were selected to enable an investigation of the effect of clearance and feature depth on mechanical properties of the joints. The groups are summarised in Table 5-2 with feature width, λ_f remaining constant at 100 µm and three different channel widths λ_c of 150, 200 and 300 µm equating to clearances of 50, 100 and 200 µm. To evaluate the performance of the structured interfaces against a benchmark, joints with unstructured adherends were also tested, serving as the control experiment. Planar, unabraded polycarbonate (denoted as 'planar untreated') and flat P80 grit sandpaper roughened (denoted as ''planar roughened') polycarbonate joints were the two unstructured baseline instances chosen. The roughened surface is more representative of the properties achievable with nominally planar unstructured joints used within traditional engineering applications.

5.3.3: Quantification of test structures

For the structured parts, the feature quantification was conducted using a Bruker contour GT optical profiler, to ascertain the variation in size from the initial silicon master to the moulded part. For both the 50 µm and 100 µm depths, the feature heights were found to be marginally lower from the initial silicon master. This result is expected due to some partial shrinkage of polymer during the holding phase of the injection moulding cycle. Similarly, the measured feature widths were found to be lower across all categories, attributed to the polymer shrinkage effect, preventing the channels within the mould inlay from filling completely; this finding was more pronounced with the 100 µm deep structures.

Despite some fractional dimensional variation, the structured parts were excellent candidates for the interlocking experiments. The progressive variation of the key feature lengths from the nominal design values of the silicon master to the final polycarbonate specimens are given in Table 5-2. The optical microscope image in Fig. 5-14 aids in visualising the difference in part geometries from the initial design to the final moulded specimen for a part with an intended feature depth of 100 µm and a clearance of 50 µm. Due to the partial shrinkage associated with injection moulding during the filling phase, the feature corners had a more rounded geometry compared to the square-wave profiles originally created from dry-etching and the micro-imprinting process. Although not a deliberate goal in the fabrication process, this will be advantageous in lowering stress concentrations around the corners of features.

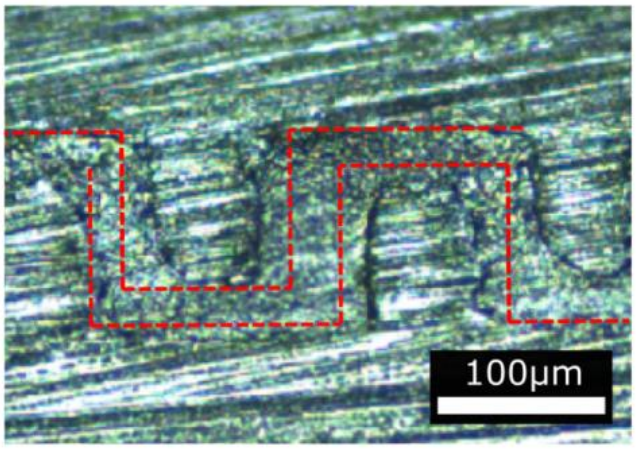

Figure 5-14: Schematic representing the typical variation in geometries from the initial silicon master (red lines) to the final moulded polycarbonate part with dimensions for the designed parts: λ_f,=100 µm, channel width λ_c =150 µm and depth D = 100 µm. The average measured dimensions were: λ_f, = 77.3 µm, λ_c = 170 µm and D = 98.9 µm.

Table 5-2: Test categories table: Designed feature dimensions and mean measured values for the silicon master and polycarbonate (PC) samples alongside standard deviations (in brackets). Parameters are: Clearance *C*, feature depth *D*, feature width λ_f and channel width λ_c, corresponding to the descriptions in Fig. 3.13.

Clearance (*C*)	Feature depth (*D*)			Feature width (λ_f)			Channel width (λ_c)		
Design (μm)	Design (μm)	Silicon (μm)	PC (μm)	Design (μm)	Silicon (μm)	PC (μm)	Design (μm)	Silicon (μm)	PC (μm)
100	50	51.7 (0.03)	48.0 (0.09)	100	93.9 (0.94)	82.8 (5.35)	200	202 (3.18)	227 (2.83)
200	50	51.7 (0.03)	48.0 (0.17)	100	94.4 (0.75)	78.6 (2.57)	300	304 (1.44)	325(3.91)
50	100	101 (0.19)	98.9 (0.05)	100	94.8 (2.45)	77.3 (5.33)	150	153 (1.79)	170 (3.85)
100	100	103 (0.13)	94.3 (0.66)	100	93.5 (2.21)	74.2 (2.29)	200	206 (2.16)	226 (2.26)
200	100	102(0.49)	94.4 (0.90)	100	93.0 (4.70)	69.4 (1.01)	300	307 (2.25)	331 (1.10)

5.3.4: Surface roughness measurements

To characterise the surface roughness of the unstructured polycarbonate and P80 roughened samples, optical profilometry was used. The untreated surfaces were coated with gold palladium (transparent surfaces may lead to image artefacts during optical profilometry) and imaged using a contour GT profiler due to the nanometre scale roughness. On the other hand, the roughened surfaces were imaged using an Alicona G4 profiler (a system more suited for imaging rough surfaces). Three samples were analysed for both the untreated and roughened groups, with three scans taken in the longitudinal and perpendicular directions. The common surface roughness parameters, average roughness (*R*a,), root mean square roughness (*R*q) and maximum height (*R*z) were measured: these are provided in Table 5-3. The results illustrate that the untreated planar samples possess a very low roughness in the nanometre range while the P80 roughened samples have a markedly higher roughness in the 2-3 micrometre range. The roughened samples were tested to provide a more representative benchmark, in line with common pre-processing treatments for adhesive joining.

Table 5-3: Surface roughness data for the untreated planar samples and planar P80 roughened samples alongside standard deviations. Measurements were taken in the perpendicular and longitudinal directions.

	Untreated Planar		Planar P80 roughened	
Parameter	Longitudinal	Perpendicular	Longitudinal	Perpendicular
Ra (nm)	32 ± 21	35 ± 27	2380 ± 647	2777 ± 685
Rq (nm)	41 ± 20	48 ± 32	3060 ± 811	3983 ± 402
Rz (nm)	403 ± 112	320 ± 130	12963 ± 2945	16023 ± 4920

5.3.5: Test rig design for injection moulded joints

5.3.5.1: Unsupported testing rig results

In contrast to the brittleness of silicon, the greater ductility associated with polycarbonate provided an opportunity to conduct tensile testing using an 'unsupported' test rig where the adherends are not fixed to supporting structures and are solely clamped at the distal ends of the specimen. The test rig design for this setup is shown in Fig. 5-15. Based on the design, samples can be fixed via mechanical fastening using bolts or via adhesive at the points of contact.

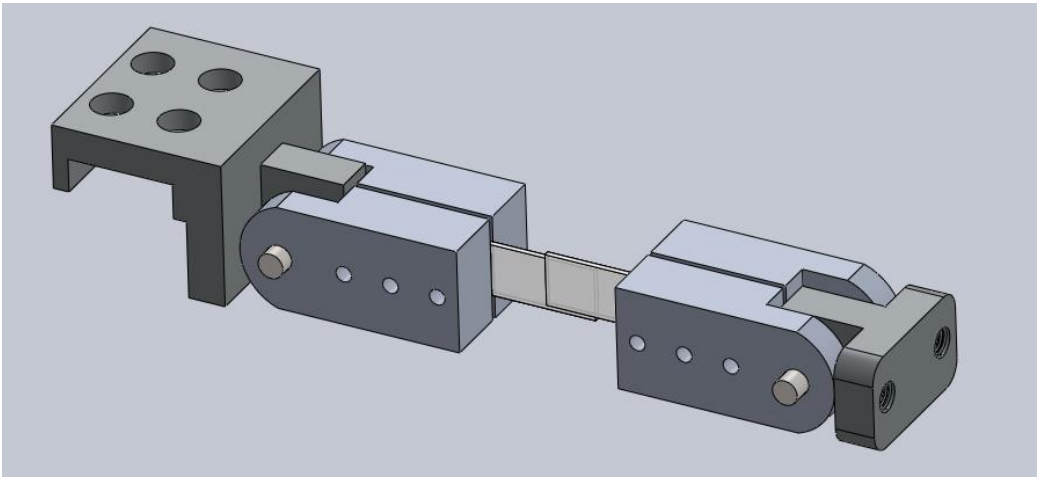

Figure 5-15: CAD design image of the unsupported test rig design where the polycarbonate lap joint (white) is permitted to bend during testing. Image taken from Solidworks CAD software.

Moulded part thickness was limited to 1 mm due to the dimensions of the injection moulding tooling. Due to this limitation, test results using the unsupported approach were limited due to bulk failure within the adherends. However, from these initial tests it was apparent that the structuring was providing a substantial increase in joint strength. Thus, it was worth addressing the bulk failure issue to enable the mechanical properties of the interface itself to be tested. The bulk failure mechanism is shown in Fig. 5-16, with the interface remaining bonded. The two possible solutions available to improve testing were outlined:

1. Redesign of mould tooling to produce a mould cavity enabling part greater part thickness e.g. 5mm
2. Utilise support structures of a comparable stiffness to polycarbonate to reduce bending effects

Figure 5-16: Image of the polycarbonate failure within the bulk of the adherends

5.3.5.2: Supported test rig design

To facilitate the testing of single lap joints comprised of the moulded parts, custom test fixtures were required. An image of the test setup is given in Fig. 5-17. As outlined, the most notable issue hindering successful testing was the 1 mm thickness of the moulded parts. To prevent bulk failure of the polycarbonate, specimens were bonded to much thicker supporting fixtures. This setup provides an avenue to resist the bending moment that would typically lead to premature bulk failure of the joint, prior to the interfacial failure. The support fixtures were 3D printed using a Form-2 3D printer using clear resin and bonded to the back of the specimens via adhesive. The specimen-to-fixture bond extended from the outer interface edge to the inner fixture edge close to the loading pins. Since this bonding length of 40 mm for the support fixture was significantly longer than the interface length of

7.5 mm, this generally required an interfacial failure exclusively within the lap joint, instead of de-bonding of the specimen backing from the holding fixture. The 3D-printed test setup was integrated into a Deben micro-tensile tester using custom made stainless steel connecting fixtures with loading pins.

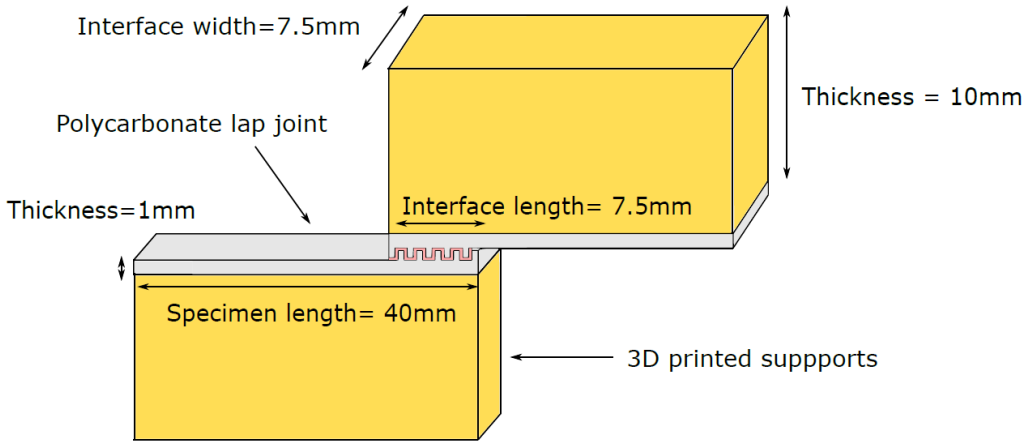

Figure 5-17: Schematic diagram and dimensions for a structured interlocking joint. Samples (grey) were cut to a length of 40 mm and bonded to thicker custom supports (orange) designed to prevent bulk failure of the polycarbonate. The dimensions of the structured bonded interface are 7.5 mm x 7.5 mm.

The extension rate chosen for testing was 0.5 mm per minute with a sampling rate of 2 Hz to record the force. Localised measurement of the strain during the test was recorded through tracking marker points at the peripheral edge of the bond-line. This enabled more accurate strain data to be obtained, through mitigating machine compliance. Images were obtained using a pixel-link camera imaging the bond-line at a sampling rate coinciding with the micro-tester (0.5 s). Strain data was obtained using Imetrum digital image correlation software to find the relative displacement between the two marker points. Load was recorded directly from the 5 kN Deben micro-tester load cell. For each category, the tests were performed five times to obtain a suitable number of tests for statistical analysis. An image of the integrated test setup with the markers for localised DIC tracking included is shown in Fig. 5-18.

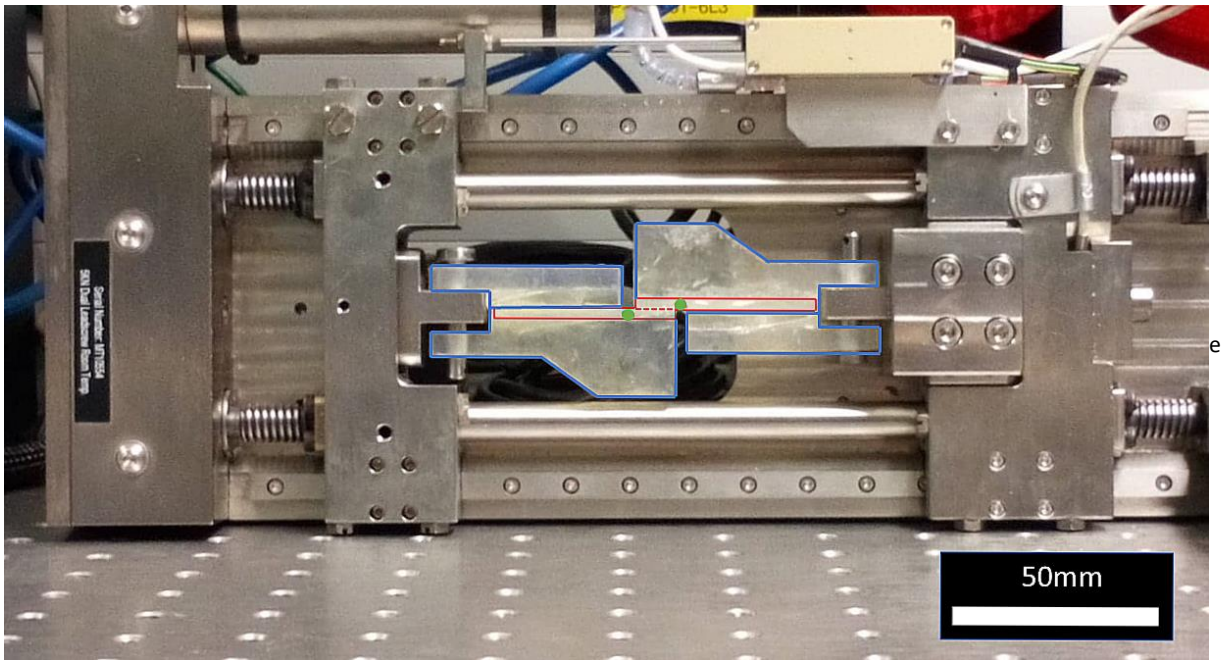

Figure 5-18: Deben micro-tester with integrated 3D printed test fixtures to prevent bulk failure of the polycarbonate bonded joint during testing. The blue outline denotes the 3D printed support structures, with the red lines denoting the polycarbonate lap joint. The green circles located at the edges of the interface denote the locations used for tracking relative displacement.

5.3.6 Digital image correlation for strain analysis

Due to the ideal optical properties associated with polycarbonate, localised strain data could be obtained using Digital Image correlation (DIC) software (Imetrum, UK). This enabled a substantially more accurate measurement of strain as the overall compliance of the test rig could be excluded. Digital image correlation is a non-contact, 2D or 3D full-field method for measuring strain. Developed in the early 1980s, it is a highly versatile measurement technique enabling measurements to be taken from the micron-scale to large scale measurements, with results comparing well to finite element simulation and strain gauges [101]. It has been used within fields including experimental solid mechanics, materials science, mechanical engineering [102, 103], civil engineering and biomechanics applications [104].

The purely optical nature of the measurement technique enables measurements to be taken with no alteration to the test setup. In this work 2D-image acquisition was performed [105,106]. The operating principle of DIC is via the tracking of unique points of data grouped into sub-sets within the image as a function of time. The relative displacement of these subsets of unique data points can be tracked to form a displacement field. The fundamental principles of DIC are shown in Fig.5-19.

An area of interest (AOI) is defined and separated into a distinct array of sub-sets as shown in Fig. 5-19a. The individual displacement values are calculated for points of the discrete sub-sections to find the overall sample deformation. In Fig. 5-19b, the red square encircling the group of pixels represents the reference image (before loading) for a discrete sub-set, with the centre point denoted $P(x, y)$. The image below in Fig. 5-19c illustrates the deformed image, with the shifted centre point, $P'(x', y')$. Tracking of the relative positions of subsets is achieved via selected correlation functions to match the similarity between the deformed and un-deformed sub-sets. The tracking procedure enables the displacement fields to be obtained for each sub-set, with the strain fields obtained via differentiation. Within the present work, DIC software was adopted for a simplified, extensometer function whereby the software tracked localised marking at either side of the bond-line to provide localised strain information for the bond-line instead of full-field strain data. Within the software, the extensometer was selected with the window size corresponding to the markings created at the edges of the bond-line; the step size corresponded to the centre of each reference window with a length of 7.5mm implemented; measurement lengths were corroborated with ImageJ software utilised.

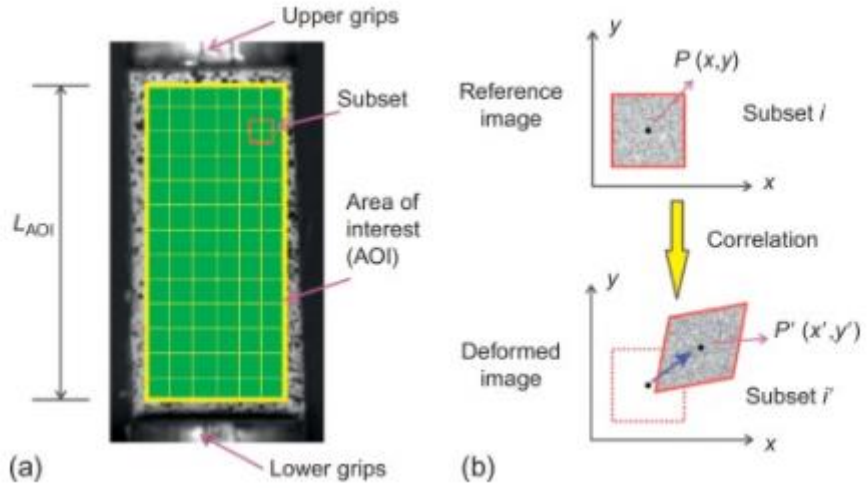

Figure 5-19: Schematic illustrating the principles of DIC particle tracking software.

5.3.7 Mechanical test results

The stress-strain data for all tested categories is provided in Fig. 5-20. The nominal shear stress versus strain graphs for the planar untreated and planar roughened samples are given in Fig. 5-20a. The nominal shear stress values were calculated as the average stress by dividing the measured tensile force data by the nominal area of the interface (7.5 mm x 7.5 mm). Planar untreated samples exhibited an adhesive failure, with the roughened samples typically failing via a mixed adhesive/cohesive failure. As anticipated, the shear strength values obtained for the roughened samples were typically larger

than the untreated tests. The mean maximum shear stress for the untreated samples was 3.96 +/- 0.73 MPa compared to 5.75 +/- 0.77MPa for the roughened specimens. Strain to failure (and hence work to failure) was also manifestly greater for the roughened specimens. Enhanced strength and toughness properties for the abraded specimens are to be expected since the marked increase in surface roughness will naturally increase active bonding surface area (by an average of 1.3 times here). Furthermore, the presence of the randomised micro-structure permits a degree of interlocking with the adhesive and increases the 'effective compliance' of the interface.

The stress-strain graphs for the structured interfaces (at feature depths of 50 and 100µm) are provided in Fig. 5-20b and Fig. 5-20c, respectively, for each of the three clearances tested. The mean joint strength values for all joint types are given in Fig. 5-21 with error bars indicating variability. All structured cases resulted in markedly higher mean strength relative to the planar untreated and planar roughened interfaces. As Fig. 5-21 highlights, for 50 µm feature depth, mean joint strengths were nearly constant over the three clearance cases with increases in the range of 57.2 to 60.8% over the planar roughened joint. For the 100 µm depth, strength increased with reducing clearance ranging from an increase of 23.3% over planar roughened for the 200 µm clearance to 95.8% for the 50 µm clearance.

Throughout the course of testing, there was a degree of variation in the failure modes observed with some samples exhibiting a gradually more ductile load response and others failing in a more brittle fashion at lower strain values – the reason for this is not entirely clear, but is likely to be due to positional variations in the assembly phase of the joints.

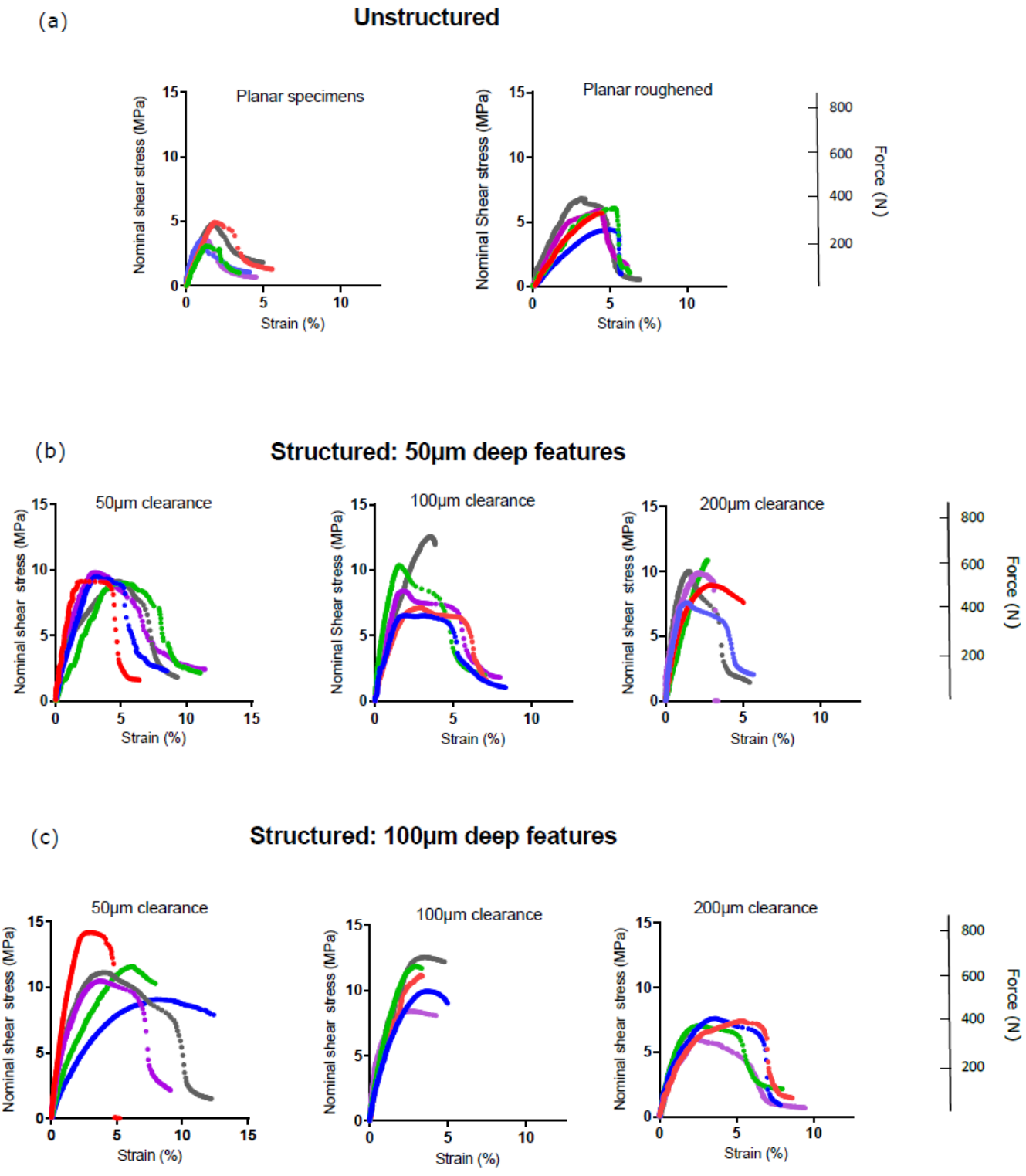

Figure 5-20: Nominal shear stress versus strain data for all tests: (a) unstructured tests (planar untreated and planar roughened); (b) structured with 50 µm deep features having clearances *C* = 50, 100 and 200 µm and (c) structured with 100 µm deep features also having clearances *C* = 50, 100 and 200 µm. Different line colours on each graph represent repeat tests.

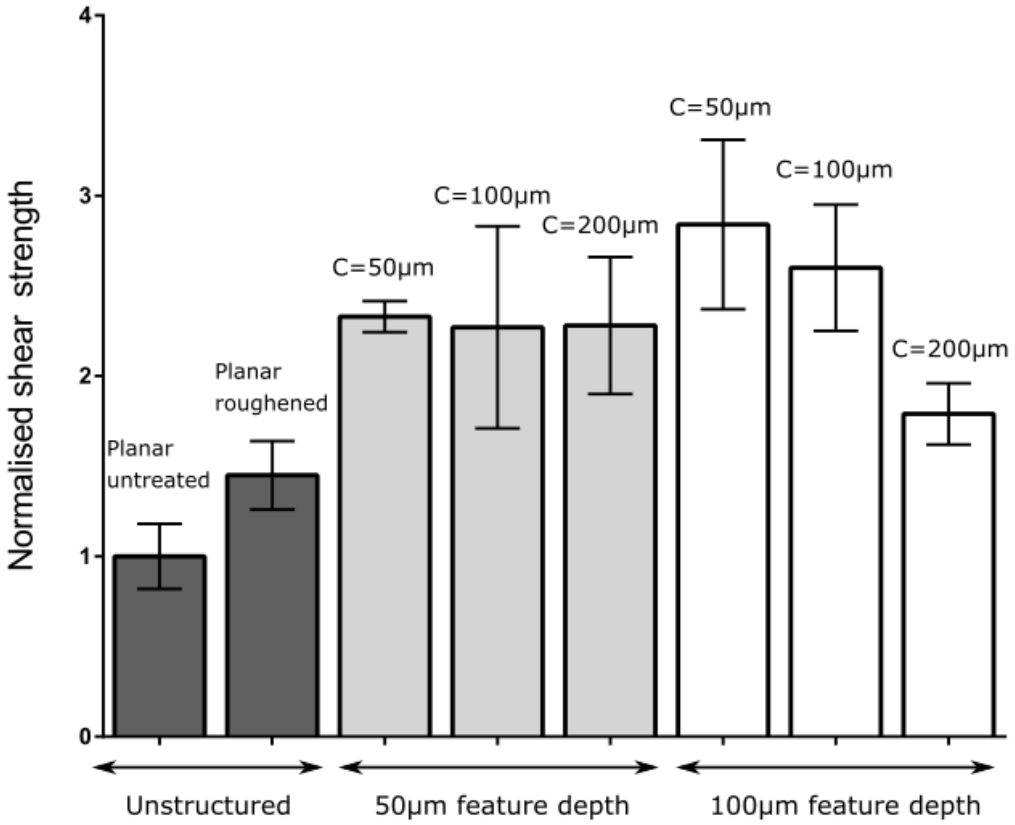

Figure 5-21: Normalised nominal shear strength relative to the planar untreated sample for each test category (+/- SD). Dark grey bars: planar untreated and planar roughened. Light grey bars: structured interfaces with 50 µm deep features. White bars: structured interfaces with 100 µm deep features. For the structured tests, the clearance *C* is labelled above each bar.

The work to failure for each test group was calculated as the total area under the force-extension graphs. The resulting mean values and variability are shown in Fig 5-22. The work-to-failure values were calculated using a script in Matlab software using the trapezoidal integral function.

In general, the structured joints absorbed more energy than the planar roughened case. The narrowest clearance instance (i.e. *C* = 50 µm) gave markedly greater work to failure for both the 50 and 100 µm depth tests. These led to increases in work to failure of 161 and 162 %, respectively, over the planar roughened case. This was explained since the tighter clearance case, in general, permitted both greater maximum load and greater displacement to failure (Fig. 3.21). Considering all the cases studied, Figs. 5-21 and 5-22 indicate the *C* = 50 µm, *D* = 100 µm case is optimum as this exhibits the best combination of both strength and work to failure (95.8% increase in strength and 162% increase in work to failure over the planar roughened case).

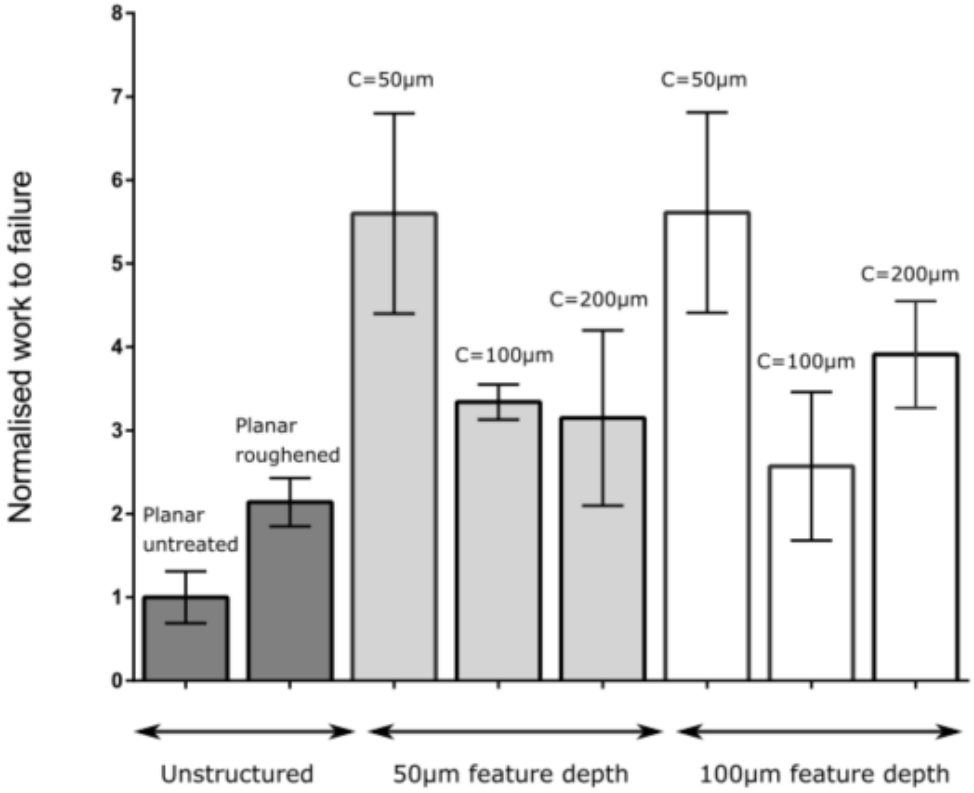

Figure 5-22: Normalised work to failure relative to the planar untreated sample for each test category (+/- SD). Dark grey bars: planar untreated and planar roughened. Light grey bars: structured interfaces with 50 µm deep features. White bars: structured interfaces with 100 µm deep features. For the structured tests, the clearance *C* is labelled above each bar.

Doubling the feature depth from 50 to 100 µm does not seem to have had a conclusive effect: the mean strengths for the 50 and 100 µm clearance increased by 21.7 and 14.5 %, but reduced by 21.5 % for the wider 200 µm case, while the mean work to failure (Fig. 3.22) was similar for the 50 µm clearance, reduced by 23.2% for the 100 µm clearance and increased by 24% for the 200 µm clearance. A definitive trend with a parameter like feature depth may be difficult to observe owing to variability in the results. There are numerous sources of variability identified including the location the features take up within the channels during bonding, the adhesive coverage of the interface surface area, and the true interpenetration depth of one set of features with another.

5.3.8: In-*situ* bond-line imaging

In-situ tests were considered invaluable, through allowing concurrent microscope imaging of the bond-line during testing to be conducted to visually investigate the mechanisms defining the loading behaviour of the interlocking joints. Two tests were conducted: one on the interface with 100 µm

deep features with 50 µm clearance and one on the interface with 100 µm deep features with 200 µm clearance (i.e. the minimum and maximum clearance cases for the 100 µm deep features). One edge of the joint was polished to enable successful imaging of the micro-features within the bond-line. Polishing was performed using a Struers LaboSystem mechanical polisher with silicon carbide paper starting with P280 grade and incremental refinement with P800 and P1200 grade paper. All testing conditions remained constant from the previous testing programme to ensure the results were comparable. Imaging of the polished side of the joint was performed during testing using a Alicona G4 profiler with a x10 objective lens. As testing progressed and the features became excessively deformed, the magnification was increased to x20 to suitably capture the interface.

The *in-situ* test results are given in Fig.5-23 for the 50 µm clearance and Fig.5-24 for the 200 µm clearance case. Figs. 5-23(a-d) and Figs. 5-24(a-d) show images of part of the interface at key stages of joint deformation while Fig. 5-23e and Fig. 5-24e give the associated stress-extension curves with markers denoting the location on the curve corresponding to the images in (a-d). The imaging was conducted near the edges of the bond-line, corresponding to the purple square denoted on the accompanying inset schematic in Fig. 5-23 and Fig 5-24. Note that the bending direction of the features in Figs. 5-23 and 5-24 are opposite from one another. This was due to the two different positions possible when loading the lap joint; this is clarified in the inset schematic.

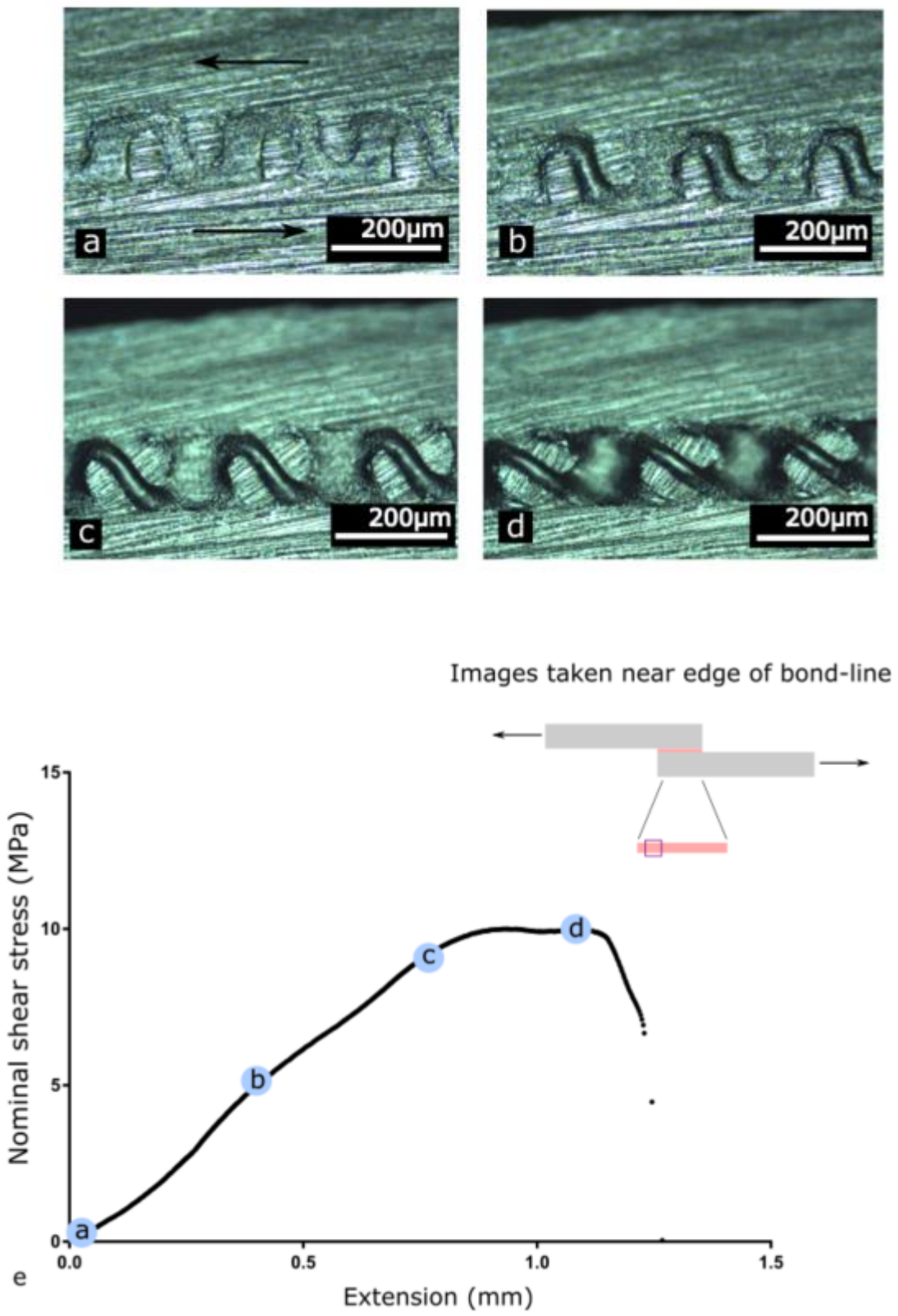

Figure 5-23: Narrow clearance in-situ results, (a) to (d): Side-on microscope images of a portion of the interface at key stages of lap-joint deformation for the structured surface with features having depth *D* = 100 µm and clearance *C* = 50 µm. (e) Nominal shear stress versus extension showing the stages on the loading path corresponding to the images in (a) to (d).

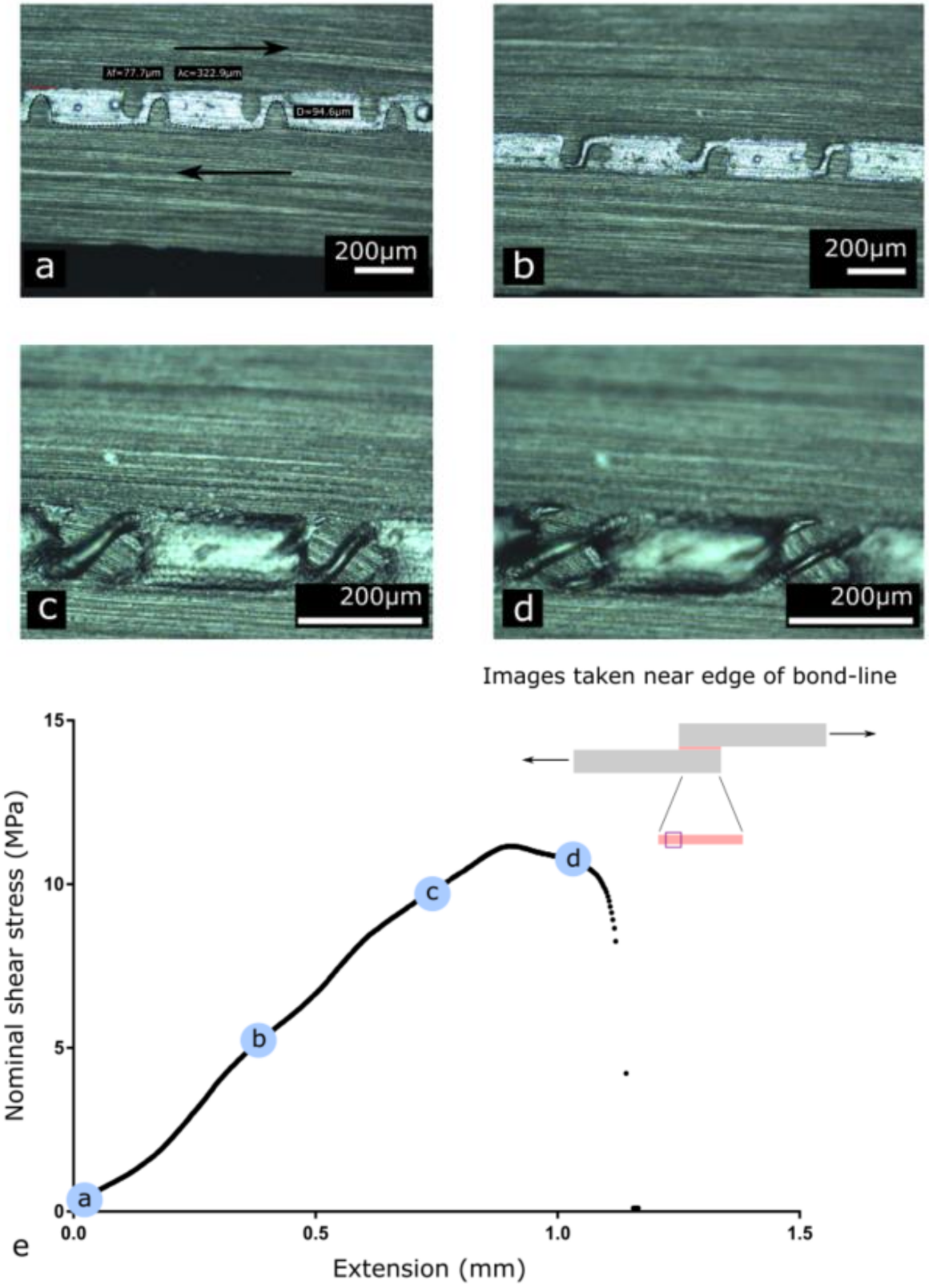

Figure 5-24: Wide clearance in-situ results, (a) to (d): Side-on microscope images of a portion of the interface at key stages of lap-joint deformation for the structured surface with features having depth *D* = 100 µm and clearance *C* = 200 µm. (e) Nominal shear stress versus extension showing the stages on the loading path corresponding to the images in (a) to (d).

Image (a) in Figs. 5-23 and 5-24 shows the unloaded interface. Image (b) shows the interface at a load sufficient to fail the planar roughened samples. From image (b) onwards, there appears to be darker regions around the features – this is caused by movement of the adhesive such that it appears out of focus. After Image (b), the joint is achieving strength and work to failure above that achieved by the planar roughened joint: the reason for this is the mechanical interlocking. Images (c) and (d) illustrate the mechanism: the resistance afforded by the interlocking features is evident in the progressive bending of the features up to the very severe bending apparent in Image (d) which is taken just before failure of the joint. Referring to the simple example of deflection of a cantilevered beam, we note that the force required increases as deflection proceeds. The features in the structured interfaces are analogous to an array of deflecting cantilevered beams each sharing a portion of the increasing resistive load. Thus, the strength of the joint is increased. The mechanism also increases work to failure due to the higher forces achieved. Additionally, the severe feature bending permits further joint displacement prior to failure. At a certain point between (c) and (d), the joint yields and the feature bending is so severe that it can no longer sustain increases in load. There is some further extension before catastrophic failure of the joint and the features then slide over each other. In the latter stages of joint deformation (after the max load is reached), localised ductile ruptures of the adhesive were apparent between the features. These then coalesce to produce complete failure of the joint. Fig. 5-25 shows a side-on microscope image of one half of the post-test interface for the 50 μm clearance case (i.e. corresponding to the test results given in Fig 5-23). Despite the severe feature bending evident during the test, the features remain intact after the test and no adherend failure is apparent. The features in Fig. 5-26 have recovered somewhat from the degree of bending evident in Figs 5-23 (d) and 5-24 (d), but, some plastic deformation is apparent. The residual presence of adhesive in Fig. 5-25 suggests a cohesive failure of the adhesive.

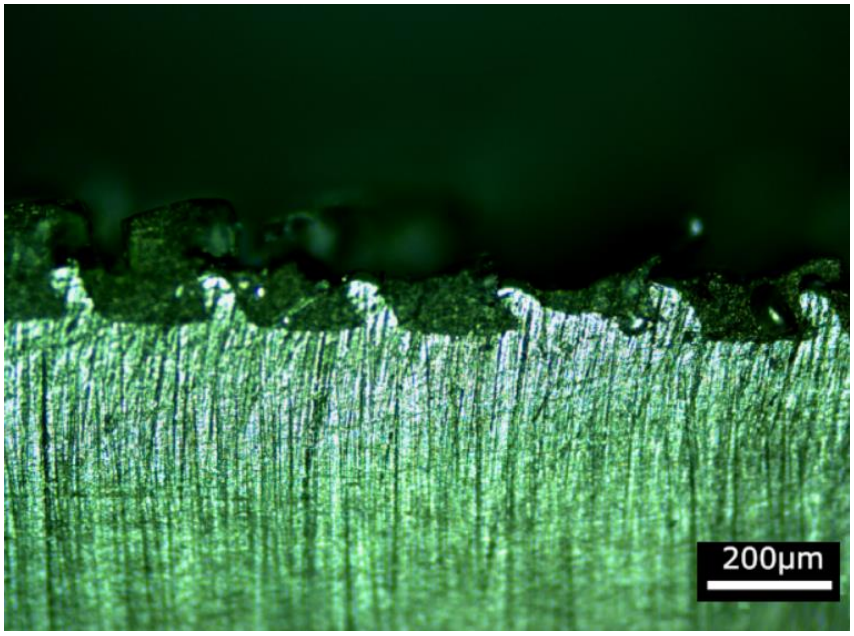

Figure 5-25: Optical side-on microscope image of one half of a failed structured interface. The image was taken at the edge of the joint. The sample had 100 µm deep features with a 50 µm clearance and corresponds to the test in Fig. 3.23.

We can also re-examine the effect of clearance in light of the bending mechanism discussed above. Recall that tighter clearance resulted in greater work to failure (Fig. 5-22). If we imagine a periodic repeating bending unit at the interface consisting of feature and adhesive shown in Fig. 5-26, then the bending stiffness of that unit will be decreased as the adhesive filled clearance between the features reduces – this is explained by recourse to sandwich beam bending theory. Reduced bending stiffness means more displacement is permitted, and thus, more work can be done. For the *in-situ* test on the largest clearance case (C = 200 µm) in Fig. 5-24a, the features happened to be positioned close to each other resulting in rather similar stress-extension graphs for the C = 50 µm and C = 200 µm cases (i.e. Figs 5-23e and 5-24e). However, other attempts at assembling the joint will likely have seen the higher clearance features bonded at a greater separation distance. Indeed, the variation in work to failure with clearance for the D = 50 µm case in Fig 5-22 must be due to greater joint displacement as the loads to failure for this case are almost constant with clearance.

The increase in work to failure with reducing clearance can be explained using engineering sandwich beam theory. Selecting one periodic portion on the adhesive interface, we may use a sandwich beam to approximate this composite periodic structure in bending, see Fig. 5-26. The core and the two face sheets of the sandwich beam are adhesive (thickness $C/2$) and polycarbonate (thickness $\lambda_f/2$), respectively. The flexural stiffness of this sandwich beam is then:

$$K = E_p\left(\frac{1}{12}\lambda_f^3 + \frac{1}{8}\lambda_f^2 C + \frac{1}{16}\lambda_f C^2\right) + \frac{1}{96}C^3 E_{ad} \qquad \text{(Eq5.1)}$$

For a fixed feature depth D, the squarewave width λ_f is also constant. Therefore, as clearance C reduces, the flexural stiffness K also reduces. Thus, we can expect greater displacement (and hence work to failure) for joints having tighter clearances. This is borne out in the experimental results of Fig. 5-23. Note that, in Fig. 5-22, the failure load is roughly constant with clearance for the *D* = 50 µm case and hence displacement must be responsible for the variation of work to failure with clearance apparent in Fig. 5-23. For the *D* = 100 µm case, failure load also increased with decreasing clearance and hence, in this case, failure load, as well as max displacement, will contribute to the variation with clearance. Note: E_p and E_{ad} are the Young's moduli of polycarbonate and adhesive respectively.

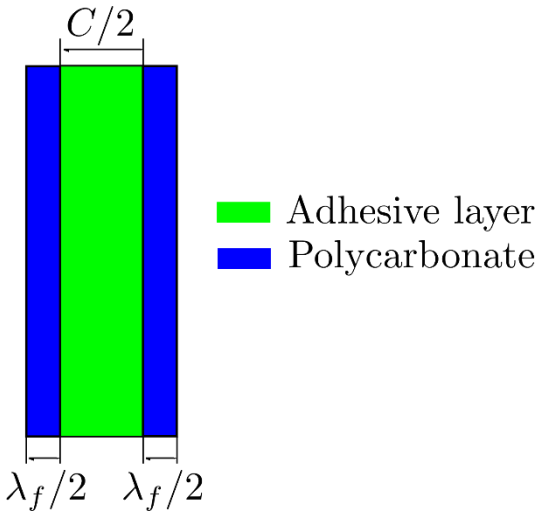

Figure 5-26: Sandwich beam theory analysis of periodic feature-adhesive repeating unit.

From a linear-fracture mechanics perspective, the implications of a micro-structured interface vindicate its usage within the context of localised crack arrestment. The Griffith based fracture criterion specifies that crack growth is stable at small values of crack length, requiring further loading to persist to drive the crack front. It is reasonable to conclude that the localised interlocking enables

the period of crack stability to last for a greater duration, with crack length countered via the presence of the micro-features acting as a barrier to catastrophic failure at lower loads.

It should be noted that the lap-joint in these tests was constrained by the backing fixtures such that out-of-plane movement (driven by the single lap joint bending moment) was restricted (see Fig. 5-19) and it is likely that a free lap-joint would behave somewhat differently. For example, it is not certain that interlocking features on more typical slender (and unconstrained) lap joints would produce as much of an effect as joint rotation may tend to promote a Mode I opening and perhaps less feature bending, but this remains to be investigated further. The fabrication process outlined has applicability for use with typical injection moulding polymers including polystyrene, polypropylene and poly ether ether ketone (PEEK). At present, the process is limited to use with polymers owing to the utilisation of injection moulding to create the final parts. However, micro-structured joints from metal adherends are possible - e.g. nickel electroplating from an etched silicon master. It is anticipated that the feature bending mechanism observed for the polycarbonate adherends would also be present to some degree in an equivalent metallic joint. However, since metallic substrates typically have lower ductility than polycarbonate, it is reasonable to expect less pronounced improvement particularly in work to failure. Another point requiring further investigation is the extent to which the structured interface can redistribute the stress peaks present at the ends of the classical lap joint.

5.3.9 Conclusions

The potential of mechanically interlocking micro-structured adherends to increase the strength and toughness of single lap joints is investigated. A fabrication protocol has been established to enable the manufacture of interlocking (square wave) micro-structured joints in thermoplastic polymer (polycarbonate) adherends. The micron-scale structuring is achieved through microfabrication techniques in tandem with injection moulding to produce replicas in polycarbonate. The parts were then bonded as single lap joints in an interlocked configuration and tensile tested using an adapted micro-tensile tester. Planar untreated and planar roughened joints were also tested to provide a benchmark. Compared to the planar roughened joints (Ra = 2-3 μm), results for the micro-structured joints revealed an increase of up to 95.9% for strength and up to 162% for work to failure. The increase in mechanical properties above that of the planar roughened joint is due to the mechanical interlocking. As applied displacement on the joint is increased, each pair of interlocking features contributes to an increasing resistive load via progressive bending of the feature pair. This proceeds to a severe level of bending until the features are no longer able to sustain increases in load. The

adhesive then fails cohesively, and the features slide past each other. The mechanism facilitates increases (over the planar roughened case) in macroscopic load and displacement owing to the local feature bending mechanics resulting in corresponding increases in both strength and work to failure. Work to failure in the latter stages of joint deformation is also likely to be enhanced by the tortuous crack path required for cohesive failure in the structured interfaces. The effect of feature clearance was examined by testing three clearance options. The tightest clearance gave the optimum mechanical properties, probably because feature pairs separated by smaller distances have lower bending stiffness (thereby increasing displacement and work to failure). Variation and oscillation in strength and work to failure values as the clearance was varied was attributed to variations in the joint assembly such as feature positioning, adhesive coverage and degree of feature interpenetration. The effect of feature depth was also studied using two feature depth options: 50 and 100 μm, but this had little effect on mechanical properties. The mechanical response of the structured joint (with the bending mechanism observed) is likely to notably alter the stress-state relative to the planar lap joint case whereby the presence of the micro-features can potentially nullify the peak stress effects and provide a means to combat premature peel stress-based fractures. Structured interlocking may facilitate a somewhat more even distribution of loading over the joint. In summary, the method has shown significant promise for increasing strength and toughness. Further investigation of the interlocking mechanism will be required to improve understanding and facilitate optimisation using a computational approach.

5.4: Future mechanical testing concepts

This chapter has vindicated the use of micro-structured interlocking within the scope of the single lap joint. This work serves to highlight the applicability of this approach for other joint configurations. Through suitable modification of the micro-test rig setup, the double cantilever beam testing has been outlined as an area of future study. Within the context this thesis, this testing approach was not pursued because of the 1 mm part thickness available from the current injection moulding tooling dimensions. Based on this, it was hypothesised that bulk failure within the adherend was likely under Mode I separation. For this approach to be viable, a shift in manufacturing would be required to produce thicker parts to mitigate this risk.

It is hypothesised that the micro-structuring would enable an improvement in fracture toughness through producing a longer crack path per unit length. This would manifest itself as regions of accelerated crack growth at the ‘top’ and ‘bottom’ of features where load would be carried under

localised tension, countered via slower crack growth at the sidewalls experiencing shear-dominant loading. In this scenario, a staggered load-displacement curve would be expected. DCB testing would be a useful avenue to develop a constitutive cohesive zone law for the micro-structured adhesive joint. Under Mode I loading, the cohesive zone can be developed through various experimental measurements known as the J-integral method; the concept of cohesive-based modelling of bonded joints will be covered in the next chapter.

The starting point for the J-integral method is the measurement of traction. The constitutive cohesive law can be obtained via the elastic calculation for the energy release rate, *J* as a function of the crack tip opening displacement δ. Within this calculation, it is common to account for the large deformation occurring prior to failure of the elastomeric adhesive. Therefore, it is necessary to include the contribution of rotation of the substrates within the vicinity of the crack tip within the expression. Conducting the crack opening test (under Mode I loading), the crack displacement, δ and opening angle, ϕ are obtained from sampling images over the course of the tests. This data is subsequently used in the expression:

$$J = \frac{12}{EH^3}\left(\frac{Pa}{B}\right)^2 + \frac{P}{B}\varphi \qquad \text{(Eq5.2)}$$

This is the same expression as the critical energy release rate equation outlined in Chapter 1 with an additional term to account for the additional rotation of ductile adherends. The energy release rate can then be plotted as a function of crack opening displacement. This value increases and plateaus at a stable value denoted as the steady-state energy release rate, J_{ss}. This curve can then be differentiated with respect to δ to obtain the traction-separation law for the DCB specimen. From literature, it has been shown that this method has good agreement with experimentally determined cohesive laws.

Chapter 6 : Modelling strategies and optimisation of micro-structured interlocking joints

6.1 Chapter outline

To help explore the fundamental load resistance mechanisms of the interlocking joints and to aid in optimising the joints, a finite element model was developed in the present chapter. Three main objectives were identified from the modelling work, these were:

1. To explain the obtained experimental results and give insight into the bond-line stress distribution and the mechanism of load resistance.
2. To provide a means of trialling different joint setups to elucidate the optimal micro-structured geometry for transmitting loads.
3. To enable the testing of different joint configurations without real-life testing based on the constitutive material parameters used for the single lap joint.

6.2 Finite element modelling: Introduction

6.2.1 Principles of FEM

The finite element method (FEM) is useful for engineering problems where analytical techniques become too complex for analysis. This technique enables approximate solutions to be generated through discretising a structure into smaller sub-divisions of elements connected via nodes. Each node has translational and rotational movement governed by the degrees of freedom (DoF). The most commonly utilised solver method within FEM is known as the variational method. This approach entails the solving of the key partial differential equation. For instance, in elasticity-based analyses, the functional used is the total potential energy of the problem. The best values for the field quantity lead to the minimisation of the potential energy of the system, satisfying internal compatibility and essential boundary conditions.

FEM is used across a wide range of engineering sectors with usage for stress analysis, fluid flow and thermal analyses. FEM is useful for determining field variable values (such as stresses). For static analyses, this is achieved through calculating the local displacements within each node. From this information, the force vector for each node can be calculated through the equation given below:

$$\{F\} = k^*\{u\} \quad \text{(Eq6.1)}$$

Where *F* is the nodal force vector, *k* is the stiffness matrix and, *u* is the displacement vector. The number of values within the matrix corresponds to the number of degrees of freedom for the elements utilised within the problem. Through calculating the nodal displacements, interpolation between nodes can determine the values of field variables across the whole structure. For dynamic analyses, such as impact problems FEM can be utilised through solving via integration of the equations describing the motion of the system, whereby acceleration, velocity and overall displacements of elements can be obtained; this approach is particularly useful for non-linear problems whereby convergence of the solution can be challenging.

6.3 Modelling strategies for structured adhesive joints

6.3.1 Linear elastic analysis

An initial starting point for characterising the single lap joint using FEM was the implementation of a simple elastic analyses of the micro-structured joint relative to the planar joint. The rationale behind this decision was to determine whether the presence of the square-wave geometry leads to any clear differences in the values and distribution of stress within the bond-line. Using elastic properties for the polycarbonate and adhesive, a three-part model consisting of the two adherends and an adhesive layer was developed.

Using the same large-scale dimensions as in the experiments presented in Chapter 5, a micro-structured interface consisting of a feature width of 50µm, spacing of 100 µm and height of 50 µm was compared with an unstructured joint. An adhesive layer of 25 µm was used and seeded at a value of 5 µm; this was deemed suitably refined to capture the stress distribution within the adhesive layer. The adhesive layer was tied to the adherends using the 'tie' option within Abaqus. Reduced integration, linear plane strain elements were used in simulations. A pressure load was applied corresponding to a stress level that was elastic for both joint setups, equating to 1.33 MPa (100N) at the distal end of the adherend. The results shown in Fig. 4.1 show the close-up view at one end of the joint for both setups with the Von Mises stress distribution plotted. From Fig 6-1, the stress values obtained for both configurations are relatively similar with peak stresses of 70.9 MPa and 75.5 MPa for the planar and structured respectively. This is a logical result as the adhesive layer is still the route of load transmission with the micro-features serving only to constrain the joint via compressive interlocking. This suggests that in many cases, the structured joint will act analogously to the planar joint at extremely low load, with further loading distinguishing performance.

The scenario where the micro-features are articulating within close proximity (assuming almost intimate contact), the stiffness and stress distribution will be higher although a high proportion of the load will be exerted compressively as opposed to the conventional mechanisms responsible for joint failure. This initial result re-affirms the concept that the non-linear stress distribution is still present, with the incorporation of bulk properties leading to performance enhancement in the presence of elevated peak stress.

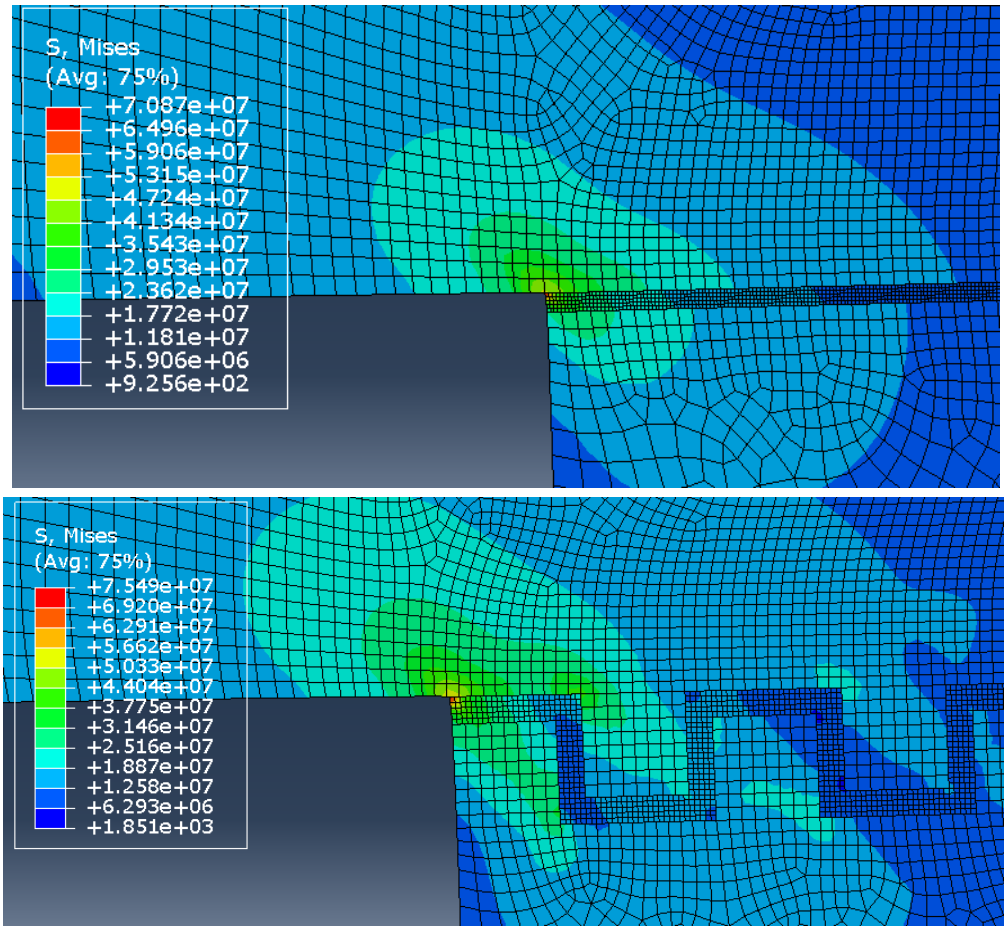

Figure 6-1: Von Mises stress contour plot for the planar model (top) and the micro-structured case (bottom); both images were taken at the left-hand edge of the joint to visualise the peak stresses.

6.4 Cohesive zone modelling approach

The most representative methodology to model an adhesive layer using FEM involves the use of cohesive zone modelling (CZM) to represent the bonded interface. Through employing either cohesive elements representing a finite thickness of adhesive or cohesive surface-based contact between two bulk components. Cohesive zone modelling relies on a traction separation response, where the separation is defined as the relative displacement between elements/surfaces; traction is defined as the load divided by the projected surface normal to the loading direction. Through the defined

traction/separation response, the mechanical response of an adhesive layer can be modelled through the three key stages: A typical bi-linear traction separation law is summarised in Fig. 6-2.

Stage 1 : Initial elastic response up to a critical traction value.

Stage 2: Damage initiation, where the stiffness of the elements begins to degrade with increasing separation, this stage represents the crack initiation within the adhesive layer.

Stage 3: Damage evolution, stiffness is progressively decreased until the material fails.

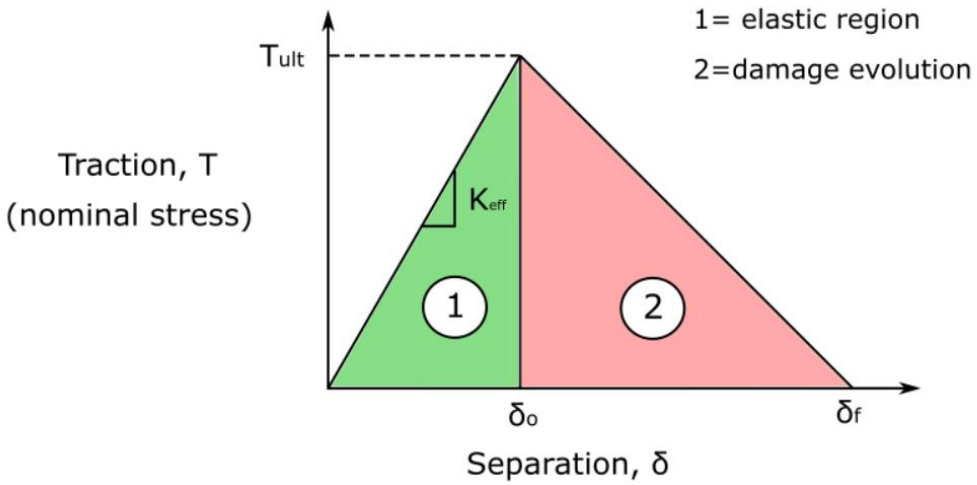

Figure 6-2: Typical bi-linear traction separation response for cohesive elements. The elastic response is denoted up to the critical separation δ_0 and ultimate traction T_{ult}. K_{eff} represents the effective stiffness of the elements during the elastic phase. G_c signifies the energy dissipated through the bond.

In addition to the bi-linear behaviour shown in Fig. 6-2, several other constitutive laws are used within adhesive bonding to simulate the damage initiation and propagation of adhesives. These include trapezoidal and exponential laws.

6.5: Material properties

6.5.1 Adhesive parameters

To obtain a representative model of the experimental test, it was important to determine the material properties of the adhesive used during the tests. Using the cohesive based approach, the mechanical loading behaviour of the joint is determined via the adhesive properties, ensuring suitable material data was defined would enable a representative cohesive model to be built. Previous experimental

data for the Araldite Rapid was used to define the cohesive law. Conventionally, the normal and shear loading regime properties are determined via double cantilever beam testing and either the three-point bend test or thick adherends shear test, respectively. However, due to limitations in relation to testing capabilities, the tensile properties were accounted for via the adhesive dog-bone tests and the shear properties that were based on the SLJ results within Chapter 2. These simulations were largely seen as preliminary in nature to determine the viability to model using cohesive elements. The parameters used for the modelling of the adhesive as a cohesive zone are given in Table 6-1. The Young's modulus value was used for the stiffness in the normal direction, E_n with the shear stiffness value estimated from SLJ testing. All modelling was performed in 2D as it was assumed that the effect of sample thickness was negligible. Different displacement at failure values were estimated accounting for the adhesive failure observed in experimental tests. The displacement at failure value was calculated as the characteristic length of each element at the bond-line multiplied by the strain at failure for the adhesive.

Table 6-1: Key cohesive parameters for the ABAQUS simulations. Element stiffness values of E_{nn}, E_{ss} and E_{tt} are given, as well as traction values for normal and shear loading directions.

E_n (GPa)	0.5
E_s (GPa)	0.3
t_n (MPa)	6.3
t_s (MPa)	3.5
δ_f (mm)	0.01

A quadratic damage initiation criterion was employed in the analysis, where the current values for traction t_n, t_s and t_t are divided by the maximum traction values for pure normal or shear loading, respectively. Damage initiation occurs once the squared product of each term in Eq. 37 summates to a value of unity. With regards to the damage evolution modelling, a bi-linear softening was chosen whereby the propagation of damage is governed via the use of the separation at failure point relative to the critical separation value (see Fig. 6-2).

$$\left\{\frac{\langle t_n \rangle}{t_n^o}\right\}^2 + \left\{\frac{t_s}{t_s^o}\right\}^2 + \left\{\frac{t_t}{t_t^o}\right\}^2 = 1 \qquad \text{(Eq6.2)}$$

6.5.2 Polycarbonate material properties

Characterisation of the material behaviour of the adherends was also required. Therefore, specimens of polycarbonate were tested to determine the elastic properties. Three tests were performed for each sample; an average Young's modulus of 2.8 GPa was calculated. Measuring the lateral strain proved difficult. Based on studying the relevant literature, a Poisson's ratio of 0.32 was used for the modelling. The in-situ imaging of the bond-line illustrates that the polycarbonate undergoes a substantial amount of plastic deformation. In response to this, it was considered imperative to adequately represent the plastic deformation that occurs during testing. Difficulties associated with cutting the moulded polycarbonate into a suitably shaped dog-bone led to reviewing literature to obtain comparable data to model polycarbonate.

A report published by the US Department of Energy included data referencing a polycarbonate known as *Lexan* with a Young's modulus value of 2.6 GPa, which was considered sufficiently close to the measured value for the polycarbonate in the present study [107]. The plastic behaviour was modelled using the Johnson-Cook hardening constitutive equation. The stress equation and associated material parameters are given in the equation below and Table 6-2 respectively.

$$\sigma^o = [(A + B\varepsilon^{pl})^n] \qquad \text{(Eq6.3)}$$

Where parameters *A* and *B* are the initial yield stress of the material and the strain hardening stress coefficient of the material respectively; the term ε^{pl} represents the equivalent plastic strain and the parameter *n* is the strain hardening coefficient. The Johnson-Cook model can account for temperature-effects; however, since the simulations were aimed at modelling loading at room temperature (well below the transition temperature for polycarbonate), this term was omitted from the equation. Likewise, strain rate dependence was not factored into the model.

Table 6-2: Johnson-Cook equation parameters used for the polycarbonate adherends.

A (MPa)	75.8
B (MPa)	68.9
n	1.004

6.6: Cohesive modelling results

A model was created for the conventionally unstructured lap joint through the utilisation of a layer of cohesive elements transmitting load between the bulk polycarbonate components. The cohesive elements were held in place between the upper and lower adherends using a 'TIE' constraint, with 'surface-to-surface contact' implemented to model the interaction between the polycarbonate. The polycarbonate was modelled using the material properties outlined in the previous section with plane stress elements and a mesh seeding of 2.5×10^{-4}. For the adhesive layer, a thickness of 20 µm was selected to model the thickness of the joint. This was deemed an acceptable value based on literature indicating a thickness of 10-20 µm is optimal for joint strength (in tandem with the observed thickness from the in-situ testing performed previously in the project). A mesh seeding of 2×10^{-6} was used, the finer mesh density of the adhesive layer relative to the adherends has been shown to increase overall accuracy of the results [36]. One end of the joint was fixed with a displacement of 1 mm applied at the opposite end. This was deemed a suitably large displacement value that was larger than the theorised maximum displacement of the test. An image of the meshed bond-line is shown in Fig. 6-3. An image of the Von Mises stress distribution just prior to joint failure is given in Fig. 6-4.

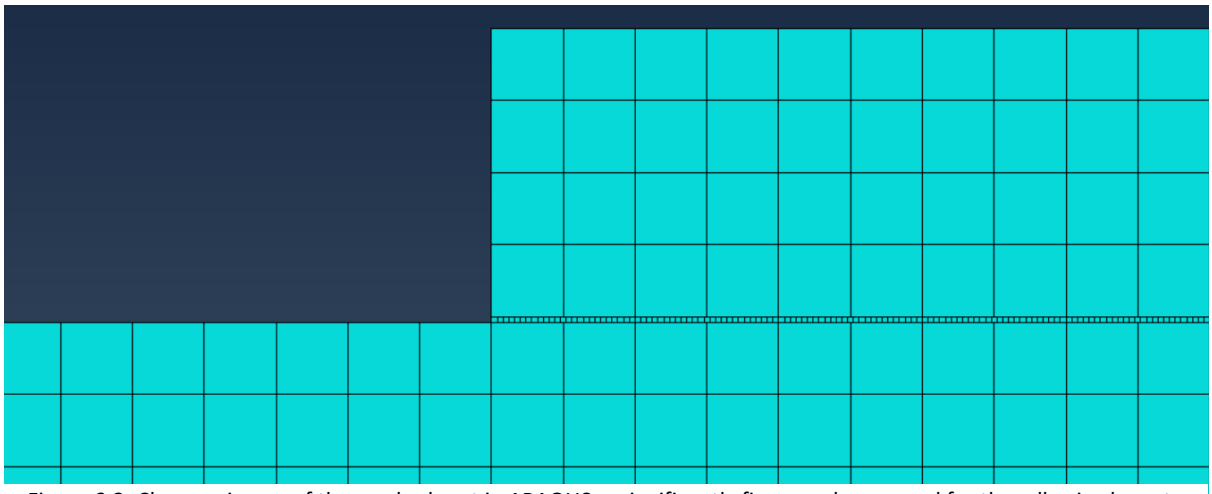

Figure 6-3: Close-up image of the meshed part in ABAQUS, a significantly finer mesh was used for the adhesive layer to capture the stresses at the edges of the bond-line with greater accuracy.

The reaction forces at the fixed end were summed together and plotted against the displacement; this is shown in Fig. 6-5. Reflecting on the measured forces and displacements for the planar tests, there is good agreement with the experimental results, with the peak stress value of 3.23 MPa comparing to 3.96 MPa. Since no measure was taken to account for micron-scale roughness and the associated mechanical interlocking with the adhesive, it is more appropriate to compare the simulations with the untreated samples. In this case, it appears that the modelling underestimates the joint strength.

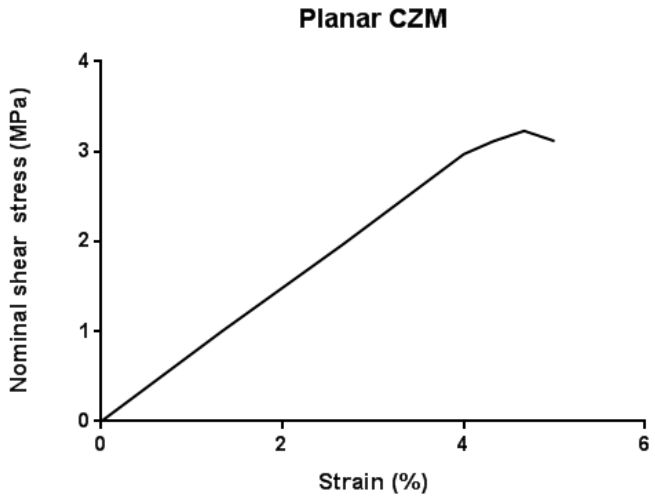

Figure 6-4: Stress-strain data for the planar lap joint using the cohesive zone model

This initial study using cohesive elements highlights the viability of using this approach for planar adhesive joints with a well-defined fracture pathway propagating across the bond-line.

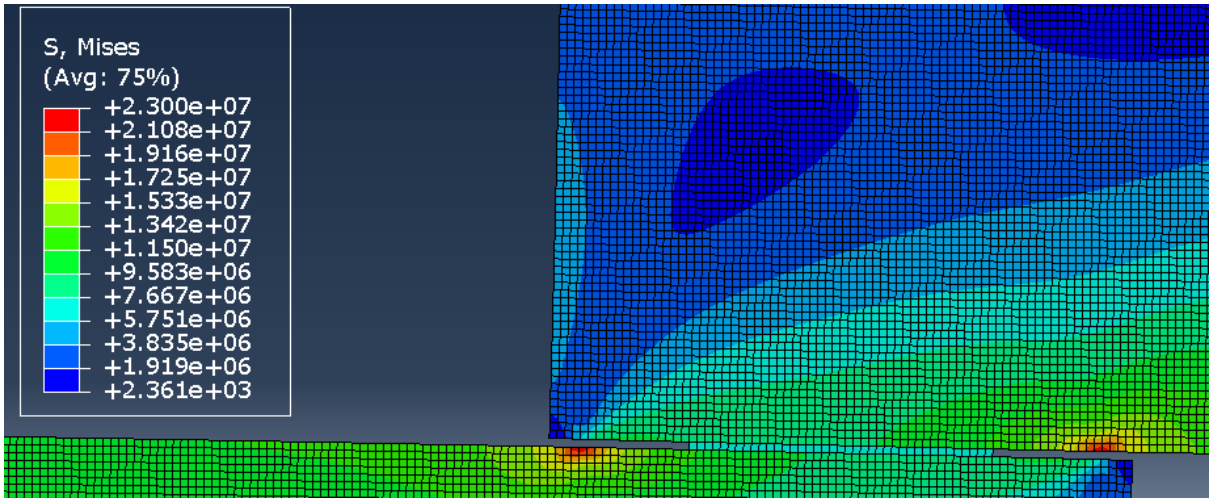

Figure 6-5: Image of the Von Mises stress distribution at the peak stress within the joint, the process of cohesive element deletion is present

6.6.1: Issues and limitations of the cohesive element-based approach

Although cohesive element-based modelling is considered the most effective approach for modelling adhesive joints, the specific scenario of interlocking micro-featured posed an issue to usage within the present work. As outlined, cohesive elements are utilised to simulate an initial elastic point up to critical damage with damage initiation and evolution simulating joint fracture. The failure pathway of cohesive elements is governed via normal and shear loading, however the points of contact within the joint (for the interlocking square wave joint) are primarily loaded in compression, effectively posing a barrier to the use of cohesive elements. Several modelling strategies were undertaken to realise the cohesive based approach; however, it was evident that the mechanics of the micro-structured joint posed a limit on usage. It is anticipated that the cohesive based approach would be more applicable for the DCB testing outlined as future work at the end of the previous chapter. Since the localised compression within the SLJ setup is not present, it is anticipated that cohesive-based modelling of this joint type would be more representative of the mechanism underpinning the experimental results.

Owing to these difficulties and as a means of assessing how much of the load carrying capacity of the joints is due to mechanical interlocking between adherends alone, an adhesive-less model was constructed relying on frictional contact between the square waves.

6.7: Frictional modelling-based approach

6.7.1: Experimental validation

The first step in the modelling procedure was to develop models that supported the experimental findings previously studied. The finite element modelling (FEM) software, Abaqus 2017 Implicit was used for all modelling work. Two separate modelling approaches were developed to simulate the interlocking joint. A 2D-model was constructed as it was assumed that through-thickness effects were negligible. Linear, plane strain elements were used for the adherends with a surface-surface interaction between the micro-features defining the contact relationship. The part mesh was seeded to be coarser at regions distal to the bond-line for computational time-efficiency with the mesh becoming suitably refined at the articulating micro-features to retain accuracy in the results. Part geometries were kept the same as in the experimental study with the adherends designed with dimensions of 40 mm x 10 mm and a bond-line length of 7.5 mm. Boundary conditions implemented replicate the testing conditions with one end of the lap joint fixed and displacement applied at the opposite end. A boundary condition was applied to the top surfaces of the adherends to prevent

vertical displacement to replicate the Mode II loading applied experimentally. Fig. 6-6 summarises the boundary conditions and loading applied in the modelling.

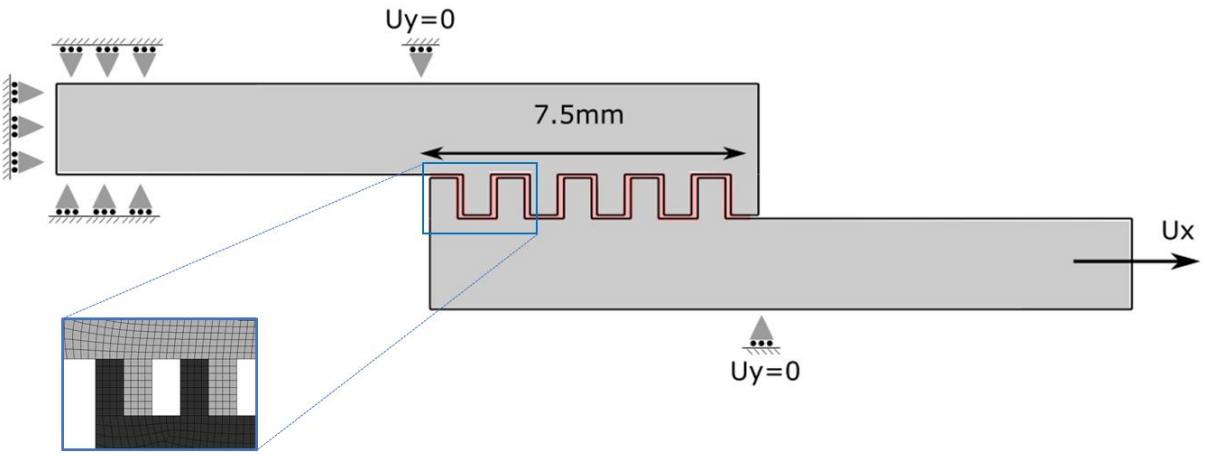

Figure 6-6: Schematic of the FE model indicating the geometry and boundary conditions. The left-hand side was fixed whilst displacement was applied at the right-hand end of the joint. Boundary conditions were applied to constrain vertical displacement on the top and bottom surfaces (as shown) to simulate the experimental testing conditions in Chapter 5. A close-up image of the refined mesh at the micro-features is provided in the bottom left.

The polycarbonate was modelled as an elastic-plastic material with a Young's modulus, E = 2.6 GPa and Poisson's ratio, ν = 0.32. The plastic behaviour was modelled using Johnson-Cook plastic data obtained in the literature [107]. Since no failure of the polycarbonate was observed experimentally, no failure criteria was included. Table 6-2 provides a summary of the mechanical properties defining the polycarbonate adherends.

The first model developed was a purely frictional model between the interlocking polycarbonate adherends. This was done to ascertain the load carrying contribution from mechanical interlocking alone (as opposed to adhesive strength). Since the joint is loaded in localised compression (at each feature) with feature bending permitting eventual delamination, it is likely that the adhesive layer plays a substantially lessened role (in a scenario where the adhesive has significantly lower stiffness and strength than the adherends) with regard to joint strength. Results were then compared with experimental results to verify the applicability of the proposed approach. Suitable values for the coefficient of friction and maximum shear stress for polycarbonate were taken from the literature (values of 0.31 and 30 MPa were selected, respectively).

To enable direct comparison with the model, experiments were conducted to study the effect of feature width on joint performance, with feature widths of 50 µm and 100 µm used for testing. The

micro-structured interfaces were produced using the micro-fabrication and injection moulding protocol utilised in the previous study and polycarbonate was retained as the adherend material. During the micro-fabrication process, anisotropic reactive ion etching was utilised to define the feature height in the silicon master. Through careful selection of the etch time, a height of 50 μm was produced enabling aspect ratios of 1 and 0.5 to be realised for each of the designed feature widths. Channel width was chosen as 1.5 times the feature width for all test samples. Samples were bonded using the 2-part epoxy (Araldite Rapid) and cured for 4 hours according to the manufacturer's guidelines. For each feature width, a total of five repeat tests was performed. Testing was conducted using a Deben micro-tester with a modified test rig (developed in Chapter 5) and designed to prevent wholescale bending and fracture of the thin polycarbonate. Testing was performed under an extension rate of 0.5 mm/min with localised strain for the joints calculated between the outer edges of the bond-line using digital image correlation (DIC) software (Imetrum, UK). The mean failure loads, strain-to-failure and work-to-failure for each group are given in the bar graph plots in Fig. 6-7.

Overall, there is reasonable agreement between model and experiment. For the 0.5 aspect ratio group, the simulations over-predict relative to the experiments by 6.9%, 11.9% and 43.5% for load capacity, strain-to-failure and work-to-failure, respectively. For the 1.0 aspect ratio group, the simulations typically under-predict by 12.7%, 29.8% and 45%, respectively. The frictional model (i.e. no adhesive present) is largely a good predictor of load capacity (results are within +6.9 to -12.7 % of the mean experimental test results). This is an important finding as it validates the concept that the adherends primarily resist the majority of the elevated loading via mechanical interlocking. Hence, in the case of load capacity, we can conclude that the adhesive plays rather a secondary role. In theory, this opens up the possibility of adhesive-less joints as long as sufficient lateral constraint is maintained to hold the joint together (such as by clamping the joint). In the present study, adhesive-less tests were not conducted due to challenges in designing a feasible test rig to ensure that normal loading could be applied to prevent separation underloading, although this approach could be explored in future studies to further validate the model results. Greater discrepancies between model and experiment are apparent for stain-to-failure and work-to-failure. This variability was attributed to the failure modes occurring in the experiments possessing an element of variability on account of the geometric variation during the assembly of the joint. For example, for the AR = 0.5 group (Fig. 6-7b-c), the simulated strain-to-failure and work-to-failure are over-predicted by 11.9% and 43.5%. This finding can largely be attributed to the experimental AR = 0.5 case fracturing at slightly lower displacements via an adhesive dominant failure because effective interlocking was less facile to achieve in practice. On the other hand, for the AR = 1.0 case (Fig. 6-7e-f), the model under predicted strain-to-failure and work-to-failure by 29.8% and 45%, respectively. Here, the micro-structured joints are interlocked to a

greater degree. Under this circumstance, the presence of the adhesive (in the experiments) can act alongside the greater interlocking to offer additional resistance to failure at the later stages of joint elongation, facilitating a more prolonged failure.

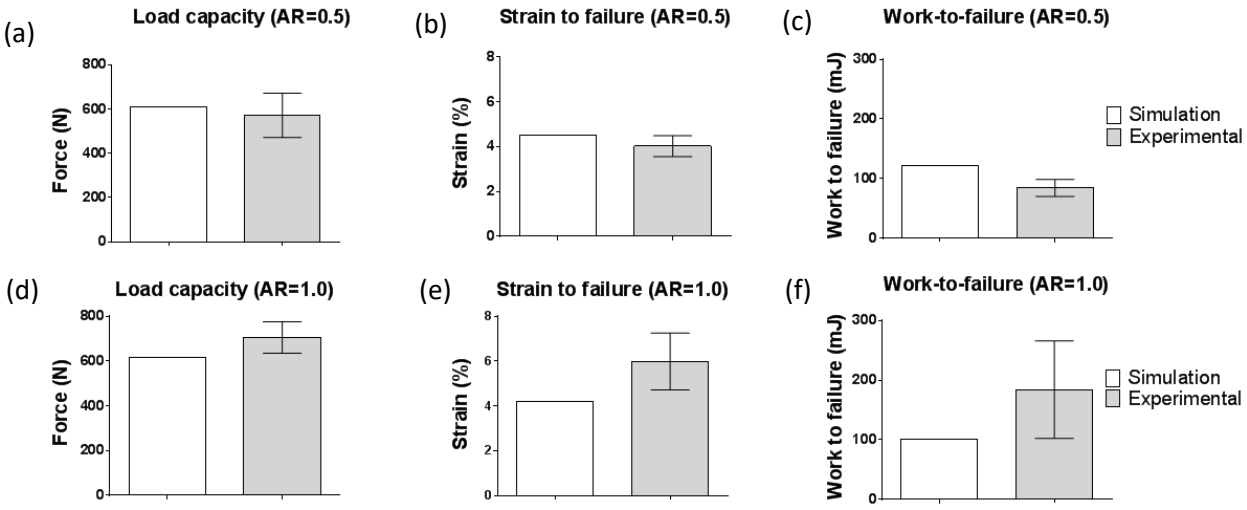

Figure 6-7: Comparison of finite element model (white) with experiments (grey) according to load capacity (left), strain-to-failure (middle) and work-to-failure (right) for: (a-c) Aspect ratio (AR) = 0.5 and (d-f) Aspect ratio (AR) = 1.0, for each experiment the sample size was *n* = 5.

Based on the results, we can conclude that the model is a good predictor of joint load capacity, whereas there is more disagreement associated with the strain-to-failure and work-to-failure values relative to the experiments. However, it is reasonable to conclude that the model will still be an effective predictor of overall trends when geometric parameters of the micro-topography are varied. More accurately modelling stain-to-failure and work-to-failure for the interlocking square-wave setup would not be straightforward with the incorporation of interfacial cohesive elements and remains a prospective challenge for future work. It should be noted that higher aspect ratios (>1.0) were not tested due to complications associated with the micro-fabrication process (i.e. difficulty in creating high fidelity features).

6.7.2: Optimisation of joint design using Design of Experiments approach (DoE)

Experimental results have highlighted the improvements in mechanical strength for micro-structured joints. The main drawback from experimental testing is the relatively low throughput leading to difficulties in testing a wide range of prospective designs. The key advantage of finite element modelling is the ability to perform simulations for a high number of tests, with economical use of time and resources. Therefore, the frictional model outlined in the previous section was taken forward in a

design of experiments protocol to ascertain the relationships between the key geometrical parameters as well as determining the geometries yielding the greatest mechanical strength.

In this study, the Taguchi analysis method was employed to expedite the optimisation process. The Taguchi method is primarily used within the manufacturing sector to optimise processes to increase yield as well as minimise variation in final products [108, 109]. Fundamentally, the process of concern is broken down into the main contributing factors with levels assigned to each factor accordingly. Experiments can be subsequently conducted with a range of factor values tested in an orthogonal array format [110,111]. The response of the dependent variables is assessed for each experiment and the importance of each factor can be identified. Within the context of optimising the structured joint performance, three geometrical variables were assigned as the control factors for the testing: feature width (λ_f), relative channel width (λ_c) and aspect ratio (AR). Two response factors were outlined as maximum load and strain at maximum load. Three feature widths were selected as 50, 75 and 100 µm; widths were chosen as multiples of 1.25, 1.5 and 2.0 relative to the feature width and aspect ratios of 0.5, 1.0 and 2.0 were tested. A table detailing the full schedule of tests is provided in Table 6-3. A total of 27 models were generated and run to fulfil the testing outlined in Table 6-3. Reaction forces were calculated at the fixed end of the single lap joint. The simulation plots are given in Fig. 6-8 with the nine separate plots separated into three rows for each distinct feature width. Each plot contains one set of aspect ratio results containing the three-different channel spacings.

Table 6-3: Orthogonal array of testing for the Taguchi analysis method.

Test no.	Feature width (µm)	Channel width (µm)	Aspect ratio (AR)	Test no.	Feature width (µm)	Channel width (µm)	Aspect ratio (AR)
1	50	63	0.5	15	75	113	2
2	50	63	1	16	75	150	0.5
3	50	63	2	17	75	150	1
4	50	75	0.5	18	75	150	2
5	50	75	1	19	100	125	0.5
6	50	75	2	20	100	125	1
7	50	100	0.5	21	100	125	2
8	50	100	1	22	100	150	0.5
9	50	100	2	23	100	150	1
10	75	94	0.5	24	100	150	2
11	75	94	1	25	100	200	0.5
12	75	94	2	26	100	200	1
13	75	113	0.5	27	100	200	2
14	75	113	1				

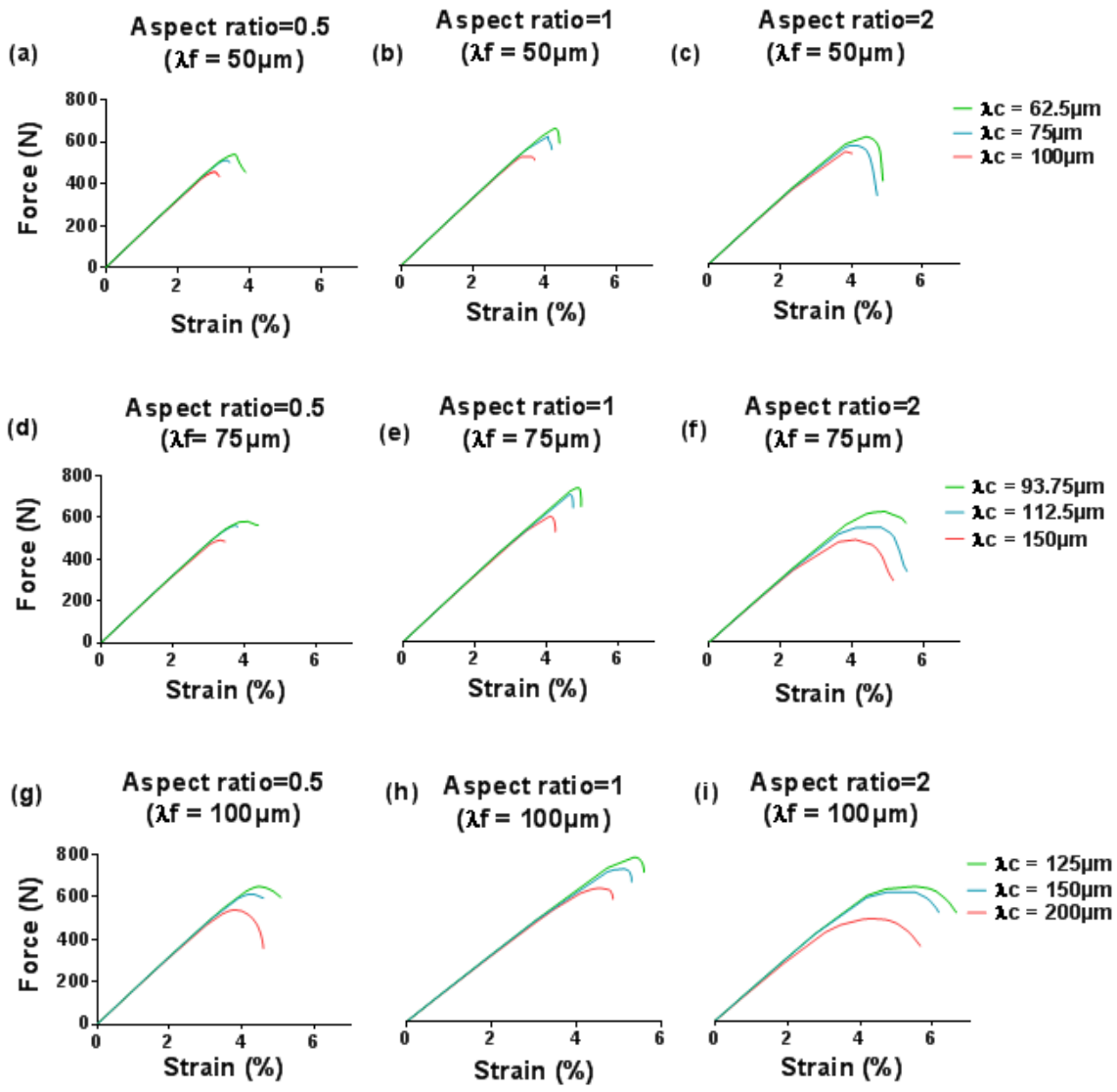

Figure 6-8: Force-strain data for all simulations; (a-c) represents results for the 50 μm feature width group; (d-f) represents the 75 μm feature width group and (g-i) represents the 100 μm feature width group. The values in the legends are channel widths (bracketed values being the multiple of the feature width).

Looking collectively at the data in Fig. 6-8, it is evident that there are key relationships that exist between parameters, although the importance of each cannot be easily determined through observations alone. The Taguchi analysis enables the response variables (maximum load and strain at maximum load to be measured for each factor using the signal to noise equation:

$$\frac{S}{N} = -10\left(\frac{1}{n}\right)\sum_{i=1}^{n}\frac{1}{y_i^2} \qquad \text{(Eq39)}$$

Where *y* is the responses for the given factor level combination and *n* = number of responses in the factor level combination. In this case the, *n* = 1 was used. The statistical analysis was performed using Minitab software. Since the objective is to maximise load capacity strain to failure and work to failure values, higher values obtained for Equation 39 indicate a more optimally performing joint configuration (see Eq39). Within the analyses the S/N ratios are calculated through grouping all tests based on the specific variable of interest and the specific level with the mean signal to noise ratio value calculated for each sub-group, providing a clear indication of the overall effect on the final mechanical response. Hence, the larger values obtained constitute the optimal combination of independent variables. The main effects plots for each independent variable are given in Fig. 6-9.

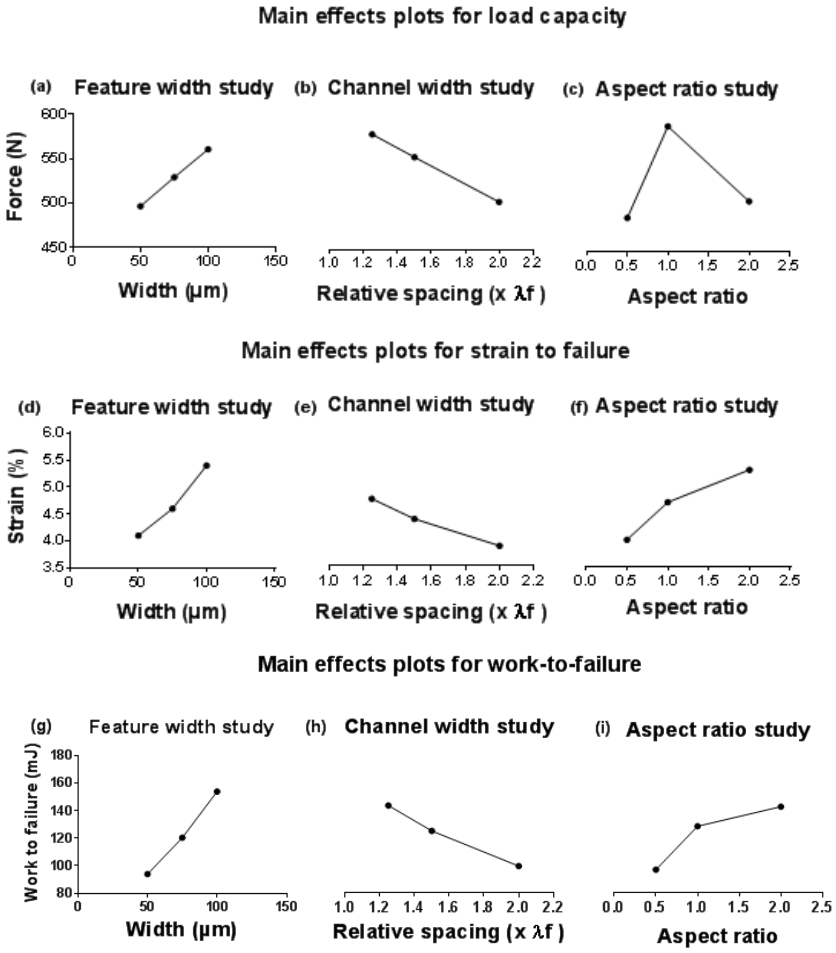

Figure 6-9: Main effects plots for the average loads for each factor level; (a-c) corresponds to the maximum load and (d-f) corresponds to the strain-to-failure and (g-i) corresponds to the work-to-failure results.

These plots represent the maximum load (Fig. 6-9a), maximum strain (Fig. 6-9b) and work to failure (Fig. 6-9c). It should be noted that, within the main effects plots, the channel width values were grouped plotted as a multiple of feature width i.e. 1.25, 1.5 and 2 times the feature widths value.

The main effects plots provide some definitive trends between geometrical parameters. For example, load capacity increases roughly proportional to feature width. This result is intuitive since increases in feature width will lead to a larger bending stiffness associated with each micro-feature - thus allowing greater loads to be transmitted for a given joint displacement. On the other hand, load capacity decreased roughly proportionally to channel width. Again, this result is expected since an increase in channel width leads to a reduction in feature density. Lower feature density leads to less features per unit area, leading to a higher proportion of loading being transmitted through each interlocking unit resulting in premature failure. For aspect ratio (AR), load capacity has an intermediate peak at AR = 1.0 (Fig. 6-9c). At AR = 0.5, the result was lower due to difficulties in achieving effective interlocking, whereby even under vertically constrained boundary conditions, a small element of adherend rotation will have a dramatic effect on how effectively lower depth features can transmit load via compression. This was identified as the primary reason that limited the ability for the lower aspect ratio features to effectively resist higher loads. When aspect ratio is increased to 2.0, load capacity also drops off again and this is likely due to the reduced stiffness of the higher aspect ratio features (i.e. longer thinner features). On the other hand, both strain-to-failure and work-to-failure increase with increasing aspect ratio (Fig. 6-9f and 6-9i). This is because, as the stiffness of the features reduces, they permit more bending deformation. Thus, the optimum result in terms of optimising total load capacity and work-to-failure was found to be the 1.0 aspect ratio case. In summary, the optimal results occurring at the intermediate aspect ratio (AR = 1) can be explained through two conflicting phenomena. Lower aspect ratios will have a greater resistance to bending associated with each feature, whilst the higher aspect ratio features enable greater bending prior to joint separation (so greater strain and work done).

6.7.3: Analysis of variance (ANOVA)

To supplement the optimisation analysis, a three-way ANOVA analysis was performed to successfully quantify the percentage contribution of the control factors as well as determining if there are any significant interaction between parameters [108, 112 ,113]. The ANOVA is a powerful statistical tool with many applications within various sectors although it is typically a tool employed by the manufacturing industry. ANOVA analysis requires the variance to be calculated within each group as well as in between each group, using this information an *F*-ratio was calculated at 95% confidence interval. Additionally, the relative percentage contribution of each factor was calculated as the sum of squares (SS) for the factor divided by the total sum of squares for each measured material property.

Prior to conducting the ANOVA analysis, certain data requirements were to be assessed to ensure that the datasets were suitable to use within this context. The requirements to be satisfied are:

1. The dependent variable must be a continuous value.
2. Independent variables are separated into discrete groups.
3. No significant outliers within the dataset.
4. The dependent variable should be normally distributed across all combinations of the independent variables.
5. No interaction between independent variables.

The first assumption is satisfied since the measured response factors are forces and extension values respectively. The second assumption is satisfied using three different values assigned for the independent variables. The third assumption was assessed using the outlier function within Minitab: using a 95% confidence interval, there were no outliers within either the stress or strain datasets. The data was plotted to assess the normality of the data. The plots showing the distribution for the stress, strain and work to failure data are given in Fig. 6-10. It was observed that the data represents a normal distribution for both response factors. To determine whether there were no interactions between groups, interaction plots were created in Minitab. The interaction plots are given in Fig. 6-11. Interaction plots signify whether variables have a direct effect upon one another. Plots in which the lines intersect illustrate an interaction effect, whereas separate lines indicate variable independence. It was observed that all combination of variables did not lead to any significant intersections indicating that this assumption can be considered satisfied.

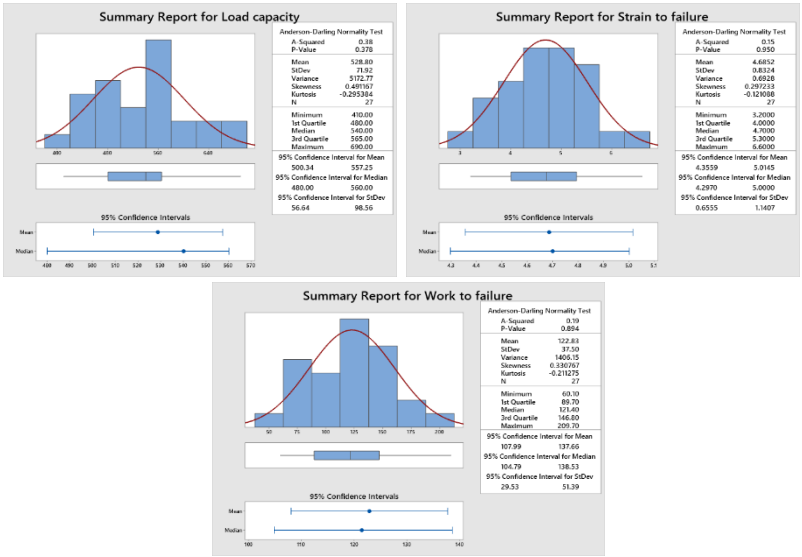

Figure 6-10: Andersson-Darling normality test plots for the maximum load, the maximum strain, and the work to failure.

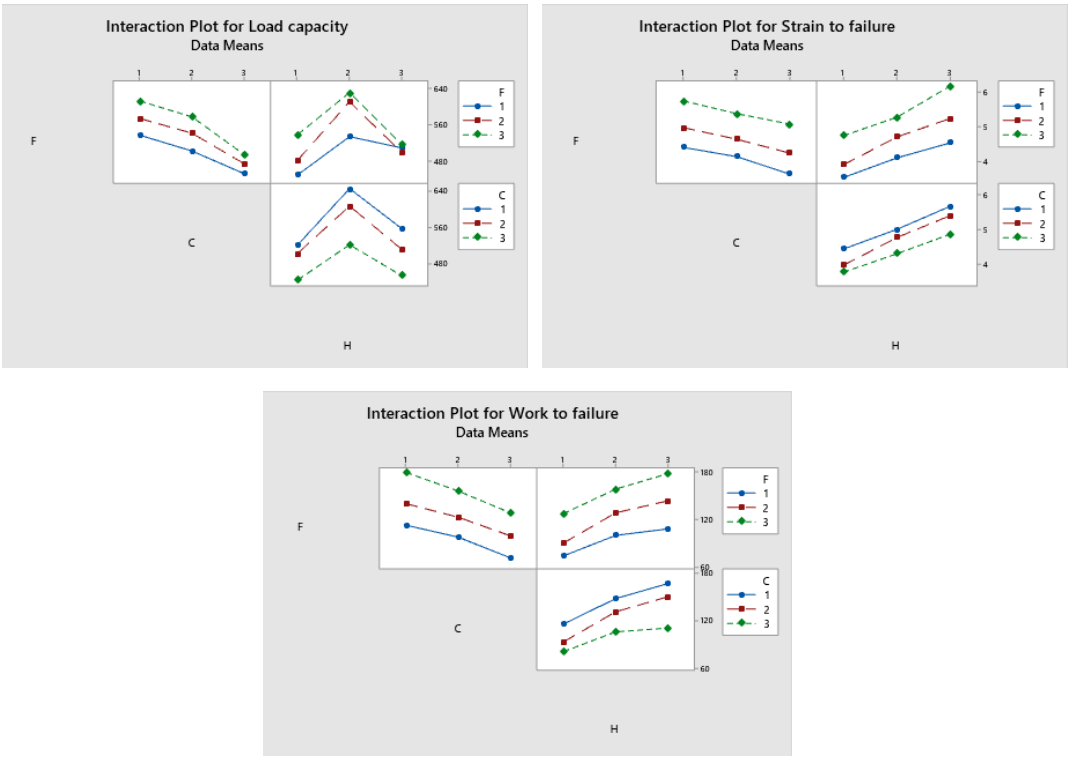

Figure 6-11: Interaction plots for the maximum load measured
(top left), strain to failure (top right) and work to failure (bottom).

Since all the data assumptions were satisfied, a three-way ANOVA analysis was conducted to assess the relative weightings attributed to the independent variables. The results for maximum load capacity, maximum extension and work to failure responses are given in Table 6-4.

Table 6-4: Table with the ANOVA analysis parameters for joint load capacity analysis (top dataset), maximum strain (middle dataset) and work to failure (bottom dataset)

Load Capacity					
Source	**DF**	**SS**	**F-Value**	**P-Value**	**%**
Feature width	2	18370	12.7	3e-4	13.7
Channel width	2	47617	32.8	5e-7	35.4
Aspect ratio	2	53981	37.2	2e-7	40.1
Error	20	14524			10.8
Strain-to-failure					
Source	**DF**	**SS**	**F-Value**	**P-Value**	**%**
Feature width	2	8.1	164.9	3e-13	44.8
Channel width	2	2.4	48.1	2e-8	13.1
Aspect ratio	2	7.1	144.9	1e-12	39.4
Error	20	0.5			2.7
Work-to-failure					
Source	**DF**	**SS**	**F-Value**	**P-Value**	**%**
Feature width	2	16341	114.43	1E-11	44.7
Channel width	2	8823	61.78	2.75E-09	24.1
Aspect ratio	2	9968	69.8	9.5E-10	27.3
Error	20	1428			3.9

Reviewing the p-values associated with each independent variable, it is clear that the very low values close to zero indicate that we can reject the null hypothesis and conclude that each geometrical factor is crucial to the final result. The key variable of percentage contribution is obtained for each geometric parameter by dividing each discrete sum of squares (SS) by the total sum of squares for the dataset.

Considering the contribution of each parameter to load capacity individually, the aspect ratio is the major effecting factor with approximately 40.1% contribution. The channel width is the second most effecting factor with 35.4% contribution with feature width resulting in a smaller relative contribution of 13.7%. These results illustrate that the optimal joint design prioritises an aspect ratio of 1.0 whilst, tighter-fitting, wider features are a secondary design consideration.

The ANOVA analysis results for strain-to-failure are notably different. Again, the low p-values indicate that the null hypotheses can be rejected. Logically, the aspect ratio was a major effecting geometric factor, with 39.4% contribution. This time, feature width was the most prominent factor with a 44.8% contribution and channel width had a 12.4% contribution to the result. The strain results demonstrate that a compromise between load capacity (AR = 1) and strain-to-failure (AR = 2) has to be considered. ANOVA analysis results for the work-to-failure values re-affirm that feature width is the primary factor with approximately 44.7% contribution. Channel spacing and aspect ratio resulted in contributions of 24.1% and 27.3%, respectively. Work-to-failure is influenced by a combination of the load level and the max strain. The improvements in joint load capacity through the optimisation protocol are considerable. Based on the lap joint dimensions and the quoted maximum joint stress for a polycarbonate lap joint using Araldite rapid adhesive, a maximum load of approximately 225 was calculated. In this study, a maximum load capacity of 773.9 N was obtained equating essentially to a 244% increase in load capacity.

It should be emphasised that the substantial improvements in load capacity and toughness exhibited through the presence of the micro-structured interface is likely to be dependent on the mechanical properties of the bulk adherends. In the current analysis, polycarbonate was modelled without a damage criterion as no adherend failure was observed in our previous experimental work. Although not explored here, the elastic modulus of the structured adherend is likely to have an important influence also. Again, higher stiffness features would tend to increase load capacity, but reduce displacement and thereby probably reduce toughness. When considering the wider viability for this micro-structuring approach, it is also important to consider costs, speed of manufacture and versatility. The creation of the tooling required for the micro-fabrication approach is certainly somewhat complex. In addition, using the current mould insert materials, the micro-structured components can only be manufactured in thermoplastic polymers such as polycarbonate, poly ether-ether ketone (PEEK) and polypropylene. To overcome this limitation, it is possible to modify the mould insert fabrication process to create a nickel-based insert via LIGA process, to enable metal-injection moulding to be realised, but this is beyond the scope of this study. We will now explore another and potentially more cost-effective approach – that of 3D printing the micro-structured joints.

Chapter 7 3D printing of structured joints and spatial tailoring

Motivation: 3D printing - a more practical manufacturing approach

The previous sections have studied the ability to fabricate and test structured joints through utilising complex and expensive micro-fabrication and injection moulding machinery. In reality, this would limit the utilisation of the proposed technique to highly developed, well-established companies within industries such as the automotive and aerospace sector. A potentially more cost-effective avenue to achieve micro-structured joints is via 3D-printing techniques. This approach would enable facile joint production requiring relatively simple machinery as opposed to the expensive and complex micro-fabrication and injection moulding tools and processes used in the previous study. 3D-printing can be considered as an emerging technology with the potential to revolutionise engineering in the 21st century with the ability to produce complex structures in a manner than can nullify or even remove the requirement of wholescale assembly of components.

7.1: Background of 3D printing

7.1.1: Additive manufacturing

3D-printing can be considered a sub-division of the branch of engineering commonly termed as additive manufacturing (AM). AM is an emerging technology with profound benefits and applications within engineering. Additive manufacturing can be broadly defined as a method of constructing 3D structures through adding material layer-by-layer to obtain desired geometries. The current materials that have been used predominantly within the field of AM are mainly metals and polymers, with the majority of work focussing on the latter. However, as research expands, applications extending as far as tissue engineering are possibilities for the future [114,115].

There are several advantages of using additive manufacturing that consolidate its relevance as a design tool. A clear benefit of additive manufacturing is the ability to fabricate complex shapes with relative ease. The main arguments supporting a shift in manufacturing processes towards 3D-printing based technologies instead of conventional methods is attributed to multiple advantages including production of complex parts with great precision, economical use of materials, flexibility at the design phase and high customisability [116]. A key benefit is the flexibility factor associated with additive manufacturing. If changes to a part are required, this can be rectified entirely through changing the input CAD file. Moreover, providing the CAD file has been produced, immediate production of the 3D

part enables testing of designs to begin on a drastically shorter timescale compared to traditional manufacturing approaches. Since only the material required for the design is used during the fabricating processes, concerns over material consumption are largely nullified. This contrasts to subtractive manufacturing methodologies where material waste is a pertinent issue. For example, the waste associated with milling can be as high as 95% with waste associated with additive manufacturing equating to around 5%.

7.1.2: Fused deposition modelling

Fused deposition modelling (FDM) is a prominent 3D-printing technique, where filaments of thermoplastic polymer are heated and ejected from a nozzle, whereby layer-to-layer deposition can be achieved. The thermoplastic behaviour of the polymer enables dispensing in a semi-liquid state with solidification upon cooling providing the form for the part. The main factors controlling the quality of printed parts are the layer thickness, width and orientation of the filaments, as well as the presence of air gaps. These air gaps can be present within the same layer or between deposited layers. The key advantages attributed to FDM include its relatively low cost, high production speeds and simple operating mechanism making it a viable option for early phase prototyping. The most prevalent drawbacks associated include relatively poor mechanical properties, reduced surface quality in finished parts and a limited number of available printing materials [117,118,112]. The image in Fig.7-1 highlights the key principles of the FDM process. A solution to improve the mechanical properties of FDM parts has come in the form of fibre-reinforced printing (although ensuring proper fibre orientation, bonding between fibre and matrix phases and nullifying void formation remain issues to address [119],[120]).

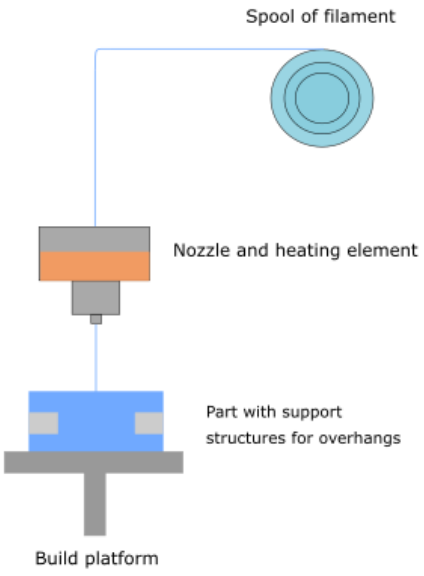

Figure 7-1: Schematic highlighting the FDM process

7.1.3: Powder bed fusion printing

The powder bed fusion process entails the formation of structures via the thermal fusion of thin layers of very fine powders, which are distributed across a build platform. The powder within each discrete layer is joined together using an incident laser beam or via a binder. The layer build-up process progresses through layers continuously being rolled on top of the previous one. The process of powder bed fusion is summarised in Fig. 7-2. Once the full part has solidified, surplus powder deposited is removed via vacuum; post-processing such as coating and sintering typically follow. The main variables dictating part quality are the size of powder and the distribution and packing of powder [121]. The two main sub-divisions of the powder bed fusion process can be categorised as either selective laser sintering (SLS) or selective laser melting (SLM). Selective laser sintering has wide applicability across both polymers and metals whereas selective laser melting is restricted to specific metals like steel and aluminium. The key difference between the processes is that SLS does not fully melt the powder with fusion of layers occurring between molecules [122]. Contrastingly, the powder is fully melted in the SLM process. When compared to FDM, the powder bed fusion process results in increased part quality as well as providing greater resolution. The process boasts great versatility across engineering sectors with usage within high-end applications such as tissue engineered scaffolds and aerospace components. No support structures are required during the design phase as the powder bed itself acts as the support for over-hanging structures. The drawbacks include high cost as well as being considered a slow process [123].

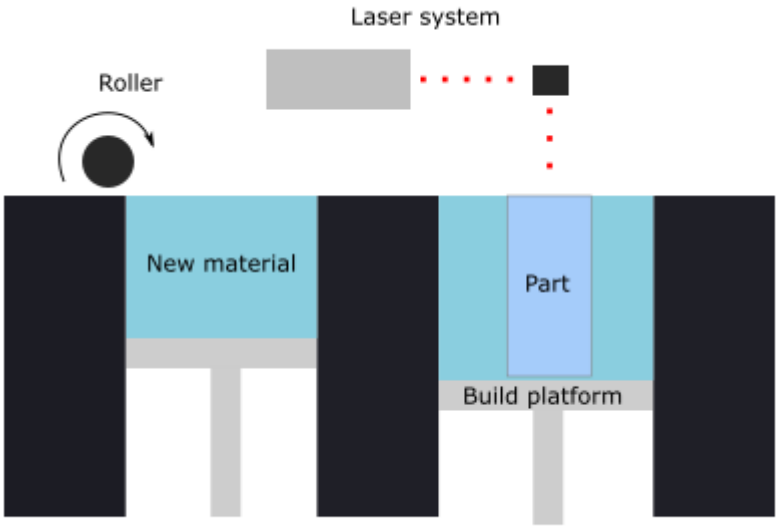

Figure 7-2: Schematic of the powder bed fusion process with a laser-based system used to thermally fuse layers of powder based on part geometry. Additional layers can be achieved through the introduction of new material via the roller system.

7.1.4: Stereolithography (SLA) Printing

The final main branch of 3D-printing is known as stereolithography (SLA) printing. Developed in 1986, this was one of the preliminary printing methods of additive manufacturing [124]. The operating principle relies on the use of ultraviolet (UV) light to initiate the process of photopolymerisation amongst a photosensitive resin. The resin consists of monomers, typically acrylic or epoxy-based, whereby UV-light leads to these monomers forming polymers chains [125]. The resin available for building the part resides within a tank with parts built though the polymerisation process on a layer-by-layer basis. The schematic in Fig. 7-3 highlights the SLA process. Post-process treatments are typically used to clean parts (such as IPA rinses) as well as heating or additional UV-curing to enhance mechanical properties. The two overriding advantages of SLA-printing are the excellent resolution capabilities and the excellent homogeneity in printed parts. Sophisticated 3D-printing setups boast resolutions as low as 10 µm. These attributes have led to usage within nano-engineering and biomedical applications [126]. However, the SLA process is commonly considered a slow and costly printing process. Through consideration of the main techniques outlined above, it was concluded that SLA-based printing was the most viable option for printing of interlocking micro-structured joints. The key benefits of high resolution and strong homogeneity within the printed parts are of paramount importance. A perceived disadvantage of SLA-based printing is the lack of material options, although this issue is becoming increasingly mitigated by developments within the 3D-printing sector.

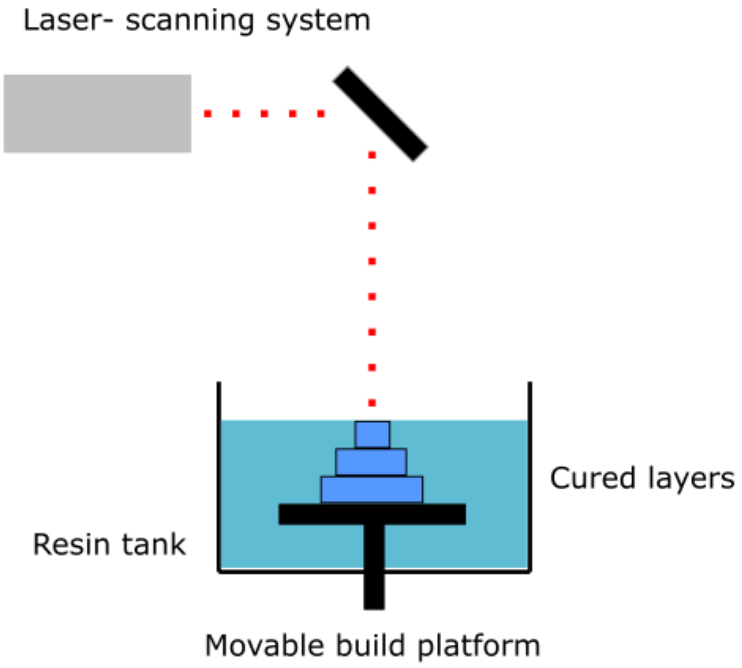

Figure 7-3: Schematic highlighting the key components of the SLA-printing process

7.2 : Form 2 printer overview

The study in the present work was performed using the Form 2 printer, produced by Formlabs. This printer is a high-end commercial printer for producing high fidelity parts with highly isotropic material properties. Although the printer is expensive relative to FDM printers, cost is typically around £2000 illustrating that this approach is economically viable as a cost-effective manufacturing route. A photograph of the 'Form 2' 3D-printer used is given in Fig. 7-4.

Figure 7-4 Photograph of the 'Form 2' 3D-prnting unit. The protective covering (in orange) has been raised to show the interior components.

The 3D-printing is achieved through stereo-lithography (SLA) based curing of layers. Due to the SLA-based operating mechanism, the feature sizes produced can reliably be on the micron scale. The printing process is followed by washing of parts in isopropanol for 10-15 minutes followed by UV curing of the printed parts to enhance the mechanical properties. The operating mechanism underpinning 3D-printing using SLA technique is depicted in Fig. 7-5. The designed part is typically created using computer aided design (CAD) software and subsequently uploaded to the printer in the form of a Stereolithography (STL) file. In this approach, a laser source is directed via galvanometers, hitting mirrors to position the laser perpendicularly to the build platform. Scans are determined in a

pre-defined manner, according to the dimension within the STL design file. The laser photopolymerises the resin (stored within the resin tank), with the part created in a layer-by-layer manner attached to the build platform. As mentioned previously, when compared to other 3D-printing technologies such as fused deposition modelling (FDM) and selective laser sintering (SLS), the SLA-process offers greater resolution.

Figure 7-5: Schematic highlighting the key parts involved in SLA-based 3D printing (image taken from [128])

In this work, a mechanically suitable engineering resin was sourced from Formlabs [128]. This resin was considered a 'tough' resin where a suitable degree of ductility is present. Adherends were printed and bonded together using the same protocols used previously.

7.2.1: Optimising print resolution

The STL design files are uploaded onto the 3D-print software, PreForm. This software enables separate design files to be uploaded into a single assembly to print multiple parts in a single printing job. Within the software, the print resolution can be controlled through defining the print layer thickness, from low resolution (0.1 mm) to high resolution (0.05 mm). Low resolution settings were typically used for structural test fixtures whereas the high-resolution settings were used for the micro-structured interfaces. A less obvious consideration regarding optimising resolution was the orientation of printed

parts on the build platform. 3D-printing conventionally utilises printing supports to enable the successful printing of overhanging structures. These supports are effectively a form of scaffolding to ensure parts do not collapse at an intermediate state when the resin has not sufficiently cured. However, it became apparent that printing in the absence of supports improved the fidelity and maximum resolution of the micro-features substantially. Parts were printed with no overhanging structures. Fig. 7-6 illustrates the two differing print setups.

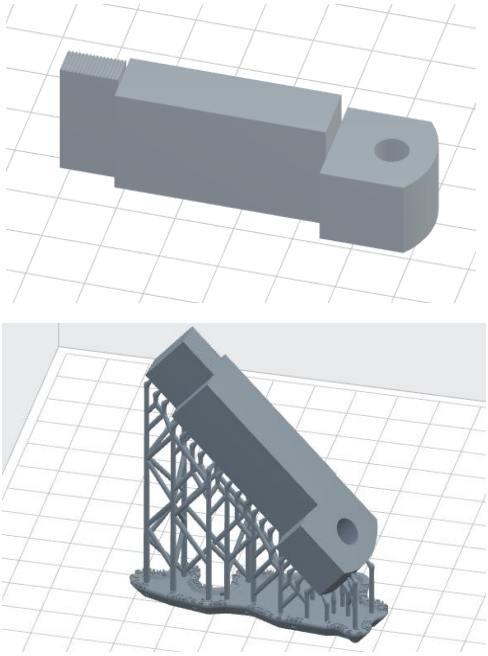

Figure 7-6: Images for the different printing orientations with the PreForm software, top image shows prints with no supports printed directly onto the surface of the build platform (checked white surface), bottom image shows the use of scaffolds to prevent failed prints occurring due to overhanging structures.

7.3 3D printing quantification

A key question to address prior to manufacturing parts was the minimum feature sizes that could be repeatedly produced using the 3D-printing process. The quoted laser spot size was 140 µm, although this figure does not accurately represent the genuine attainable resolution. Feature quantification was conducted for the Grey pro resin to measure the resolution for feature width, channel width and feature height. Based on this data, empirical equations were generated to enable an extrapolation between the designed size and the actual produced size.

7.3.1: Aspect ratio and feature height study

A range of aspect ratios were studied to enable more accurate production of the intended dimensions at the point of testing. A series of 400 µm wide lines were printed with deigned heights equating to aspect ratios of 0.5, 1, 1.5, 2 and 3. Each aspect ratio was repeated three times, with cross-sectional measurements taken using the optical microscopy function within the Alicona Profiler. A representative image for the micro-structures is given in Fig. 7-7. It can be seen that the square-wave features are well defined with periodicity retained. Plots showing the trend between the measured aspect ratios and feature heights are given in Fig. 7-8. The linear best fit equation is also provided alongside the data.

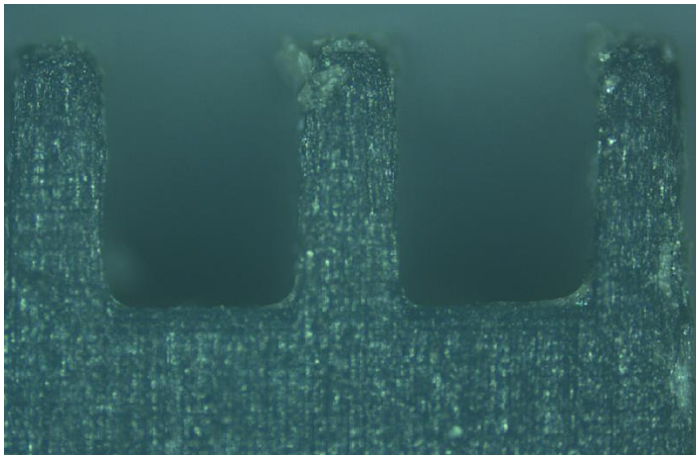

Figure 7-7: Cross-sectional microscope image of 3D-printed micro-structure using the Grey pro resin.

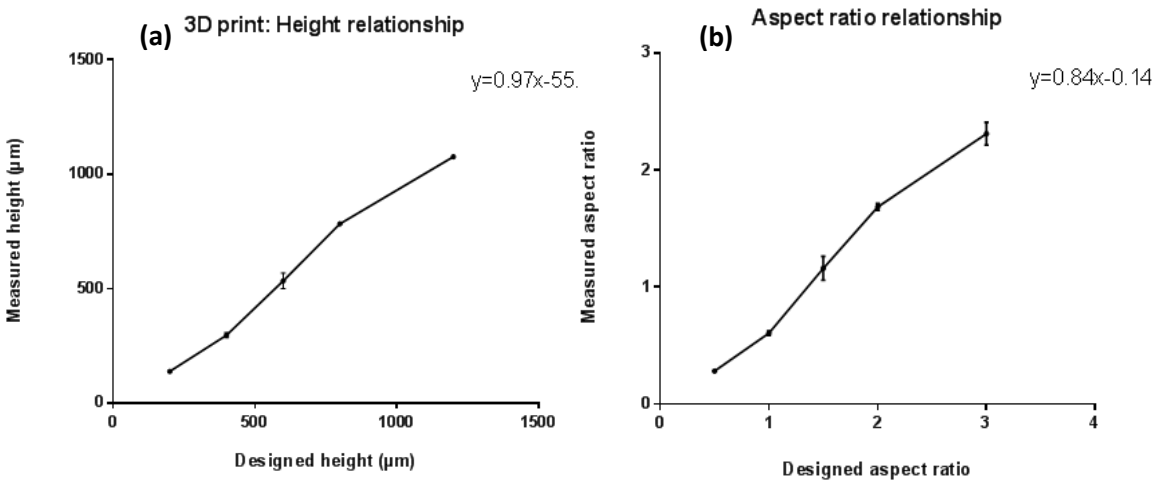

Figure 7-8: Plots showing the trend between: (a) measured feature heights and designed feature heights and (b) measured aspect ratio versus designed aspect ratio. Error bars represent +/-SD.

The data is reasonably linear, with the measured value heights consistently lower than the designed values. This trend was accounted for in the design phase of the micro-structured joints fabrication process.

7.3.2: Feature width study

A series of feature widths of 200 µm, 300 µm, and 400 µm were printed with relative channel widths of 1.5, 2 and 2.5 multiples of the feature width. The lowest value of 200 µm was selected to be a small amount above the quoted laser spot size (140 µm) to ascertain whether the minimum spot size was a true measure of resolution; 400 µm was deemed a suitably large maximum feature size. Again, quantification was done using the Alicona profiler, with measurements performed using ImageJ software. Three measurements were taken at discrete lines on the sample. The plot illustrating the trend between designed and measured feature width is shown in Fig. 7-9, with the mean feature width plotted alongside error bars (+/-SD). The data illustrates that there is a substantial difference between designed width and measured value. The empirical equation has a *y*-offset value of 39.95 indicating that there is effectively an offset value to account for at the design phase. This is a logical finding as the laser spot size of 140 µm imposes a clear limitation on printing at this length scale. Reflecting on the results for the empirical equation, it was observed that a measured width of 300 µm could be achieved through designing a feature size of 239 µm.

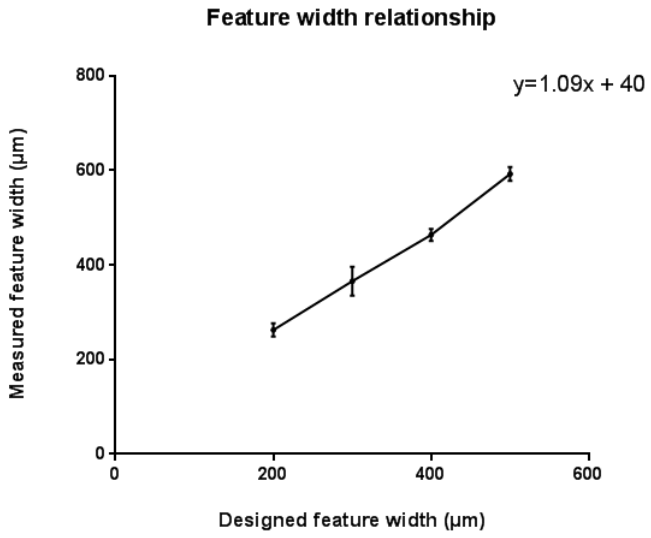

Figure 7-9: Feature width plot for measured feature width versus designed feature width (error bars +/-SD).

7.3.3: Feature spacing study

Feature spacing is of critical importance to realise the goal of positioning features closely to enhance interlocking and increase density. The discrete plots in Fig. 7-10 represent the measured versus designed results for each individual feature width tested. As mentioned previously, each plot contains three data points corresponding to relative spacing of 1.5, 2 and 2.5 multiples of the feature width.

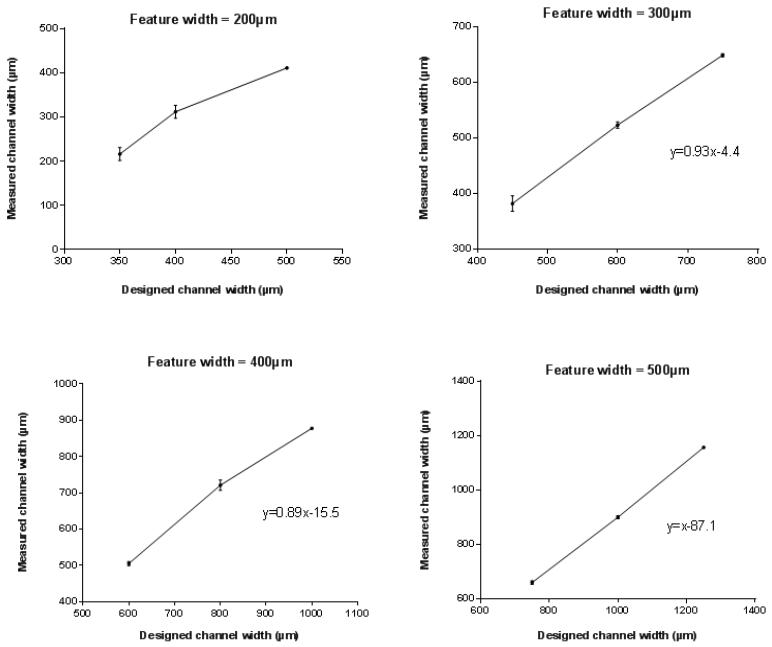

Figure 7-10: Plots showing measured channel spacing versus the designed spacing for each respective feature width studied.

As can be seen from the plots, the 200 µm category had an inherent variability with a markedly different empirical relationship relative to the other groups; this indicates that the resolution limit between features is around the 350 µm to 400 µm value. As the feature width value was increased, there was a strong correlation between the remaining groups. The measured channel widths were consistently lower than the feature width. This indicates that there is a degree of feature enlargement that occurs during the photo-polymerisation process. This information was used in the design process to ensure that designs were appropriate to ensure interlocking of joints was feasible whilst ensuring that relative clearance was not overly high.

7.4: Material testing and test setup

7.4.1: Dog-bone tensile tests

The Formlabs Grey pro resin was selected for testing due to its ideally suited mechanical strength properties, with a quoted ultimate tensile strength of (61 MPa) and reasonable extension to failure (13%). It was hypothesised that the combination of strength and moderate toughness would enable the bending phenomena observed in polycarbonate testing to be repeated to provide a mechanism for substantial improvements in joint performance. Although the grey pro resin has mechanical properties provided via the company, it was recognised that there can be some variability in these values based on the part geometry, print orientation and curing protocols used post-printing. A dog-bone specimen was printed and tested using the Deben micro-tester. Post-processing for the dog-bone was conducted in accordance with the manufacturer's guidelines with a rinse in IPA bath for 15 minutes followed by UV-curing at 80^{o}C for 30 minutes. An extension rate of 0.5mm/min was used during testing with the local strain recorded using the Imetrum DIC software used previously in Chapter 3. A table summarising the mechanical properties for the grey pro resin is given in Table 7-1. These values were used in elastic-plastic simulation in Abaqus to accurately compare experimental and simulation results.

Table 7-1: Material properties for the tough Grey Pro resin from Formlabs obtained via dog-bone tests.

Young's Modulus (GPa)	UTS (MPa)	Failure strain (%)
2.6	65	19.4

7.4.2: 3D printing test rig design

The mechanical testing was performed using the Deben micro-tester used previously in Chapter 3. The steel fixtures used during the previous round of tests were used again enabling the single lap joint to be connected to the micro-tester via pins. To mitigate out-of-plane bending of the lap joint, fixtures were bonded to the lap joint to provide additional support. These were bonded to the adherends. To ensure the interface fails prior to the supports, a substantially longer bonding area was employed. The CAD design image in Fig. 7-11 illustrates the test rig design used.

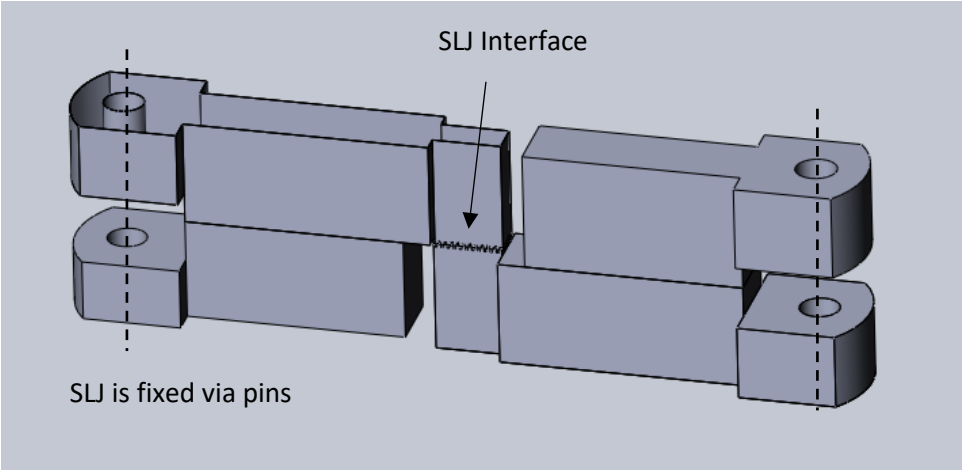

Figure 7-11: CAD image of the 3D-printed single lap joint setup. Additional fixtures are bonded to the lap joint to mitigate eccentric bending that could lead to premature bulk failure.

7.4.3 Mechanical testing setup

Prior to testing, the samples were bonded using a similar pre-processing protocol to the one documented in Chapter 5. Supporting fixtures were roughened using P80 sandpaper, washed and dried within an oven at 80°C. This ensured that the supporting fixtures would confer enough adhesive strength to mitigate premature failure as well as ensuring the interface was perfectly dry. Supporting fixtures were assembled for each 'half' of the joint with the interface bonded afterwards. To ensure intimate bonding was achieved between each interlocking feature, careful alignment of the joint was performed with downward pressure from a weight used to ensure features were bonded close together. From quantification work outlined in the previous section, it was deemed that printing resolution was limited to around 200 µm. A mechanical testing study on the effect of aspect ratio was performed with λf = 300 µm and λc =600 µm used throughout with feature depths of 150 µm, 300 µm and 600 µm used to produce aspect ratios of 0.5, 1 and 2, respectively. A control experiment with no structuring was included with the adherend surfaces roughened (P80 sandpaper) prior to assembly to provide a fair benchmark for comparison. A novel investigation was performed with feature widths varied as a function of the bond-line with narrower, more compliant features (AR = 2) at the edges and stiffer, more mechanically strong features (AR = 1) positioned centrally. It was hypothesised that the greater compliance introduced at the edges of the joint could lead to a re-distribution of stress within the joint, forcing a higher proportion of load to be carried at the centre of the joint and holding potential for higher strength performance. A schematic illustrating the structure of the interface is given in Fig. 7-12. Simulations were also conducted for comparison with the experimental results. The

same FE modelling approach (i.e. interlocking joint with frictional contact) as outlined in Chapter 6 was used again here with the elastic-plastic properties for the Grey Pro resin obtained from the tensile test data.

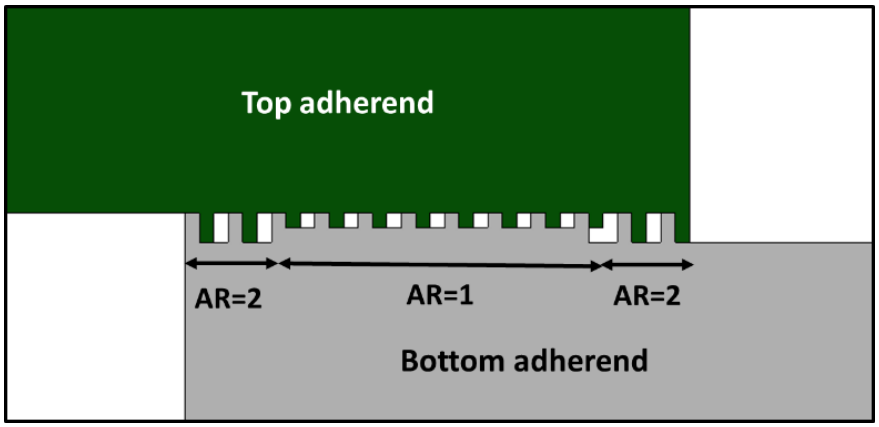

Figure 7-12: Schematic of the 3D printed joint offering variable hybrid feature options (in this case, two feature types) along the bond line. Here, the more compliant 'Aspect Ratio 2' is placed near the edges and the stiffer 'Aspect Ratio 1' is used in the central region.

7.4.4: Mechanical test results

The experimental force versus strain results for the 3D printed joints are plotted in Fig. 7-13. As expected, the structured joints (Fig. 7-13b-e) perform better than the planar roughened joint (Fig. 7-13a) in terms of load capacity (up to three times better). The mean experimental results are shown in Fig. 7-14 together with the corresponding simulation results, the force strain plot shown in Fig7.15 also illustrates the varying load responses for the AR=1, AR=2 and hybrid joint configurations.

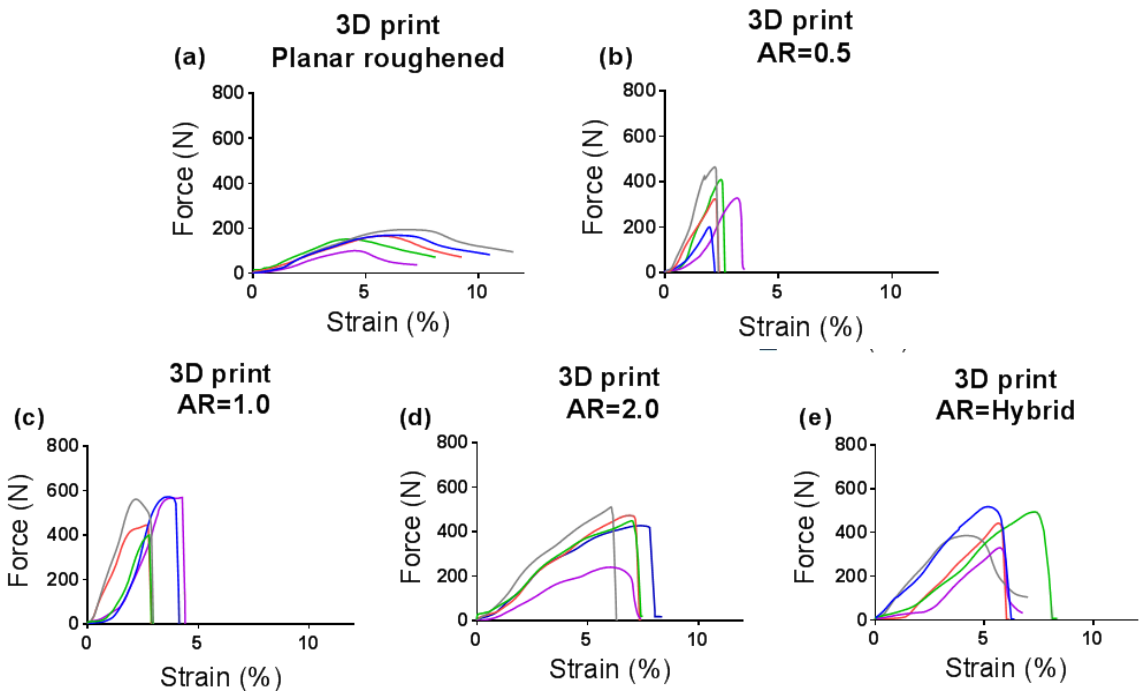

Figure 7-13: Force versus strain for all 3D printed joints: (a) unstructured, planar roughened, (b) all features at AR = 0.5, (c) all features at AR = 1, (d) all features at AR = 2, and (e) hybrid with AR = 2 at edges and AR = 1 in the centre. Different line colours represent repeat tests under identical conditions.

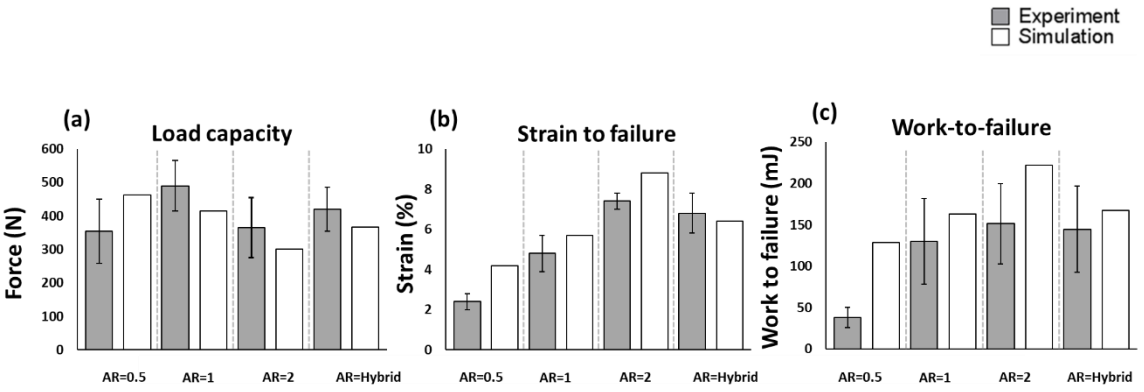

Figure 7-14: Bar plots comparing mean experimental results (grey) with simulation (white) for the 3D printed joints: (a) load capacity, (b) strain-to-failure and (c) work-to-failure. Error bars represent (+/-SD).

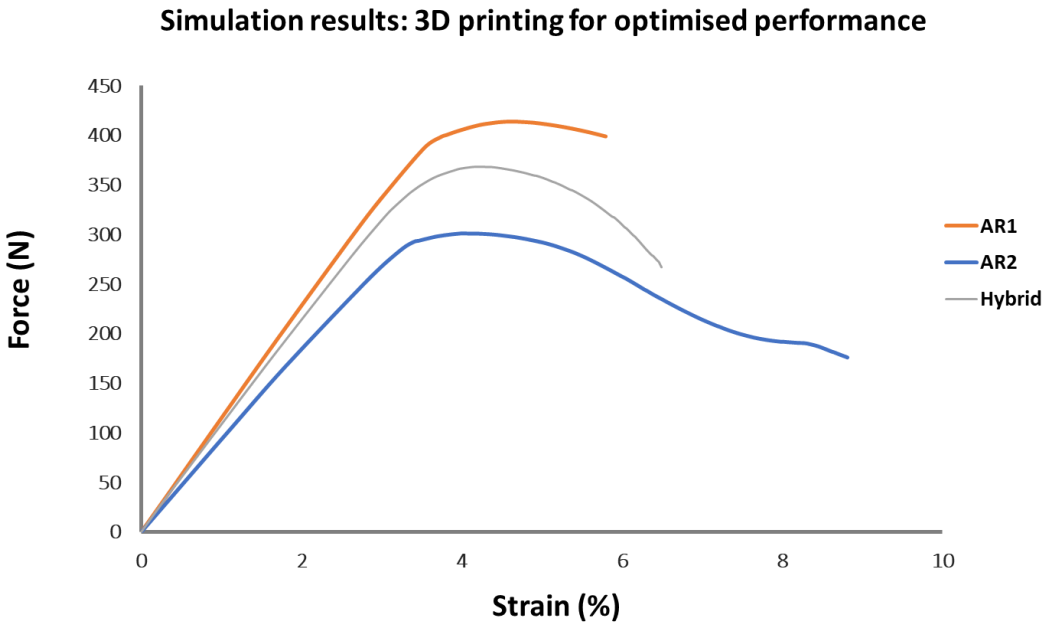

Figure 7-15: Force strain data for the AR1, AR=2 and AR=Hybrid joint designs

The experimental results for the structured joints (in Fig. 7-13 and Fig. 7-14) again illustrate that aspect ratio has a clear effect on load capacity, as well as, strain-to-failure and work-to-failure. The AR = 0.5 test group results in lower values of load capacity and strain-to-failure. This is again likely due to reduced interlocking associated with the lower feature depth and issues upon joint assembly. Load capacity then increases as we move to the AR = 1.0 group as the feature depth is now sufficient to facilitate effective interlocking and compressive loading as well as enabling effective bending interaction of features. Increasing the aspect ratio further to AR = 2.0 causes the load capacity to drop off as these longer, thinner features are significantly less stiff. For strain-to-failure (Fig. 7-14b) and work-to-failure (Fig. 7-14c), a progressive increase was noted with increasing aspect ratio. This is likely to be simply because higher aspect ratios are less stiff (in bending) and lead to more joint displacement resulting in greater strain and greater work done. Recall that the hybrid feature case (with AR = 2.0 at the edges and AR = 1.0 in the central region), was designed to tailor the joint to have a desirable compromise between load capacity and energy absorption (toughness). Indeed, we can see clearly from the results in Fig. 7-14 that the experimental results for the hybrid aspect ratio case (with AR = 1.0 & AR = 2.0) has load capacity, strain-to-failure and work-to-failure that are intermediate between the AR =1.0 and AR = 2.0 results. Thus, the hybrid aspect rstio yields an improvement in the toughness properties (work-to-failure) relative to the AR = 1.0 group, whilst retaining greater load capacity than the AR = 2.0 category, this in re-affirmed when observing the load-strain curves given in Fig.7.15

whereby the hybrid joint configuration provides intermediate strength and strain to failure results relative to the AR=1 and AR=2 tests.

Broadly speaking, the FE results in Fig. 7-14 exhibit the same key trends as the experiments although there are some discrepancies in the magnitudes predicted. A source of difference between experiment and model in this particular case might be attributed to the inherent variation in 3D printed feature geometry relative to the more precise micro-fabrication strategies used earlier, with the printed features having a propensity to be printed slightly wider than designed. Reflecting on the strain-to-failure simulation data, it appears that the simulations generally over-predict joint extension (Fig. 7-14b), apart from the variable feature width group. A corresponding over-prediction is present for work-to-failure in Fig. 7-14c. The over-prediction here can be accounted for due to the contact definitions within the model assuming perfect contact for each interlocking site. Under these idealised conditions, full feature bending is realised leading to elevated strain values. A further limitation associated with the model was the lack of fracture data implemented for the grey pro resin. This would explain the disparity for the AR = 1.0 group where failure was primarily driven through a bulk failure (as we shall see later in Fig. 7-15c) at comparably lower strain values (~4% - see Fig. 7-13c). On the other hand, greater bending and extension were permitted in the simulations. During real experimental tests the presence of adhesive and slight variation in depth of interlocking profiles as well as horizontal clearance likely provided greater extension for the hybrid model than the frictional contact model utilised in the present study.

In summary, the strain-to-failure and work-to-failure values were consistently lower in experiments compared to the simulation data and this is attributed to the rapid failure/facture typically observed during the tests (with bulk fracture observed especially for AR = 1.0). This contrasts with the experimental findings for the more ductile polycarbonate testing presented earlier, re-affirming the requirement of ductile adherends for optimal loading response. Through the course of testing, different failure mechanisms were observed (Fig. 7-16), with adhesive failure observed commonly for the samples failing at lower loads such as the AR = 0.5 group (Fig. 7-16a), indicating that reduced interlocking suppressed the constraining effect that yields the mechanical improvement. For samples that failed at higher loads, the predominant failure mechanism was via mixed adhesive/bulk adherend failure (Fig. 7-16b) and bulk failure (Fig. 7-16c), emanating at the edges of the bond-line and propagating across the entirety of the bonded joint. This (bulk) failure mechanism was not observed for the lower aspect ratio results. For AR = 1.0, failure typically occurred through fracture of the bulk grey pro resin first (Fig. 7-16c) indicating that the mechanical properties at the interface exceed the mechanical properties of the grey pro resin used. The hybrid joint type, on the other hand, tended to exhibit a consistent cohesive-based failure pathway (without bulk failure). This is likely due to the

more compliant AR = 2.0 features near the edges permitting more displacement and reducing peak stresses.

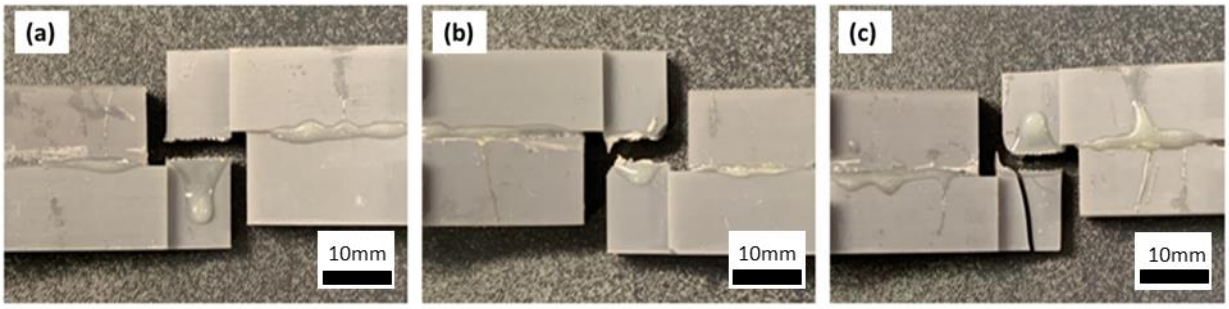

Figure 7-16 :Typical observed joint failures: (a) Conventional adhesive-based failure typical of the weaker joints with AR = 0.5, (b) mixed-failure with partial bulk failure observed for intermediate strength joints with AR = 2, and (c) complete bulk failure was exhibited for the stronger, better performing joints with AR = 1.

Therefore, we have demonstrated that the hybrid joint can give a compromise of properties between the high load capacity of AR = 1.0 and the high energy absorption of AR = 2.0 while also avoiding the detrimental bulk fracture observed for the AR = 1.0 case. This suggests that the 3D printing approach has good potential to be used in spatially tailoring joints for optimum mechanical properties (as well as being more rapid and cost effective). This is a preliminary study and further improvement is possible. For instance, the main drawback of the SLA-based 3D printing route used here is the minimum feature size being limited to 200-300 µm. It is likely that reducing the feature size further would increase the capability of the method by increasing the accuracy with which specific features could be deployed in particular regions – such as at the near-edge parts of the bond-line where the peak stresses occur and through introducing a substantially greater number of high density, high aspect ratio features at the very edges of the joint.

7.4.5: Conclusions

The viability of micro-structured interlocking joints has been highlighted through both experimental testing and numerical modelling-based analyses. A frictional adhesive-less modelling approach, simulating contact between adherends has been shown to represent the interlocking joint effectively and localised feature bending was shown to be principally responsible for mechanical performance. The majority of the load carrying capacity of the joints was shown to arise from the mechanical interlocking of the adherends – an idea that opens up the possibility of adhesive-less joints. An optimisation protocol was established to determine the trends associated with different micro-feature geometries, with Taguchi analysis used to visualise performance. Increasing feature width led to

increase in strength and toughness whereas it was found that channel width was inversely proportional to both strength and toughness. It was observed that micro-features with an aspect ratio of 1 were optimal. Lower aspect ratios did not possess sufficient compliance to enable progressive bending. Contrastingly, higher aspect ratios did not provide sufficient resistance to bending leading to reduced strength. A three-way ANOVA analysis confirmed that aspect ratio was the primary factor contributing 39.5% to the strength of the joint. A cost-efficient route to produce micro-structured adhesive joints was showcased through the use SLA-based 3D printing. A study was performed to investigate the ability to increase joint strength through varying feature width across the bond-line, leading to a reduction in peak stress. Experimental results illustrate that varying feature width led to improvements in joint extension whilst retaining joint strength as well as mitigating bulk failure within the micro-structured lap joint.

7.5 Butt joint testing

7.5.1: Hypothesis

Throughout the thesis so far, the single lap joint setup has been the focus of the mechanical testing owing to its simple configuration and ubiquitous presence within engineering structures. Following on from this work, it was deemed worthwhile to investigate the implication of micro-structuring on a rather different type of joint scenario: the tensile loading of butt joints. The schematic in Fig. 7-17 summarises the key loading mechanisms that are hypothesised prior to testing.

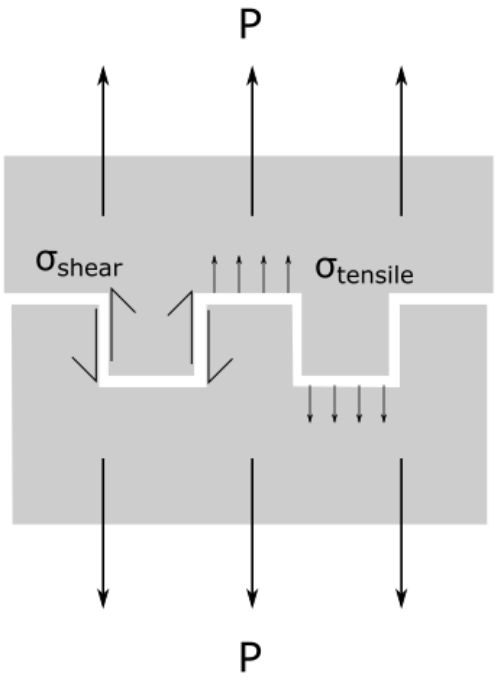

Figure 7-17: Schematic highlighting the predicted mixed-mode response within the structured butt joint.

As mentioned in the introduction chapter, work by Maloney and Fleck [44,45] highlighted that repeatable square-wave geometries can lead to enhancement in joint strength through introducing a mixed-mode loading within butt joints. Essentially, the shear mode is stronger than that of normal separation and the sidewalls of the square wave features serve to introduce shear resistance. The key feature of this work was the millimetre length-scales employed. In the current study, the intention is to enhance the contribution of Mode II shearing at the sidewalls of the features which will in turn increase the peak load within the joint whilst delaying crack propagation within the joint as Mode I failure is more likely to emanate at the horizontal section of the bond-line compared to the areas subjected to shear forces. The idea being that, smaller features lead to greater density of features and hence, more shear resistance.

7.5.2: Butt joint test rig

A custom rig was designed and created through using Formlabs 3D-printing equipment. This rig was designed to integrate directly into the mechanical testing jaws within the Deben Micro-tester. The butt joint was fixed via adhesive to the test fixtures. To ensure that interfacial failure occurs prior to failure of the area used to fix the joint, the fixture contact area was substantially larger (35 mm x 20

mm) than the interface contact area used for the tests (8.5 mm x 7 mm). A photograph of the butt joint test rig integrated within the Deben micro-tester is given in Fig. 7-18.

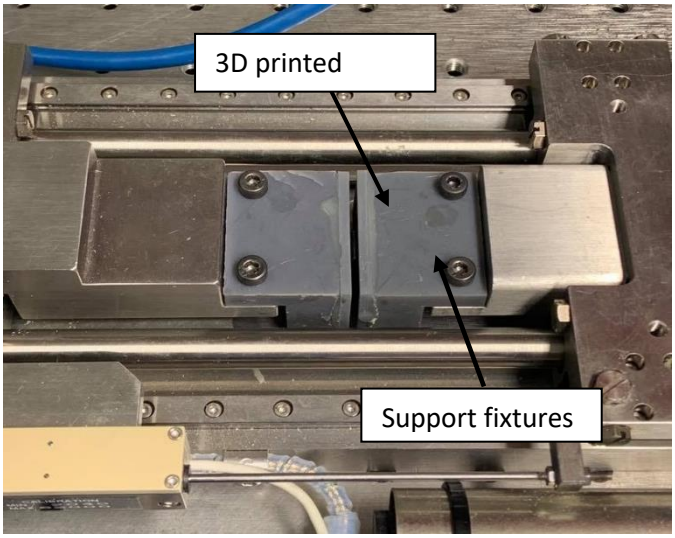

Figure 7-18: Photograph of butt joint test rig integrated within the Deben micro tensile tester. Support fixtures are fixed via screws into the main clamping jaws with the 3D-printed specimens fixed via adhesive.

7.5.3: Mechanical test results

The same adhesive bonding protocols were utilised as in previous experimental work. Two experiments were conducted with 3D-printed joints with AR = 2 micro-features (300 µm feature width, 600 µm height and 600 µm spacing) compared to roughened planar specimens. It was hypothesised that the greater aspect ratio will yield a larger active bonding area as well as providing a greater proportion of Mode II loading per unit length. Nominal stress was calculated from the contact area of the interface; the extension data was tracked using Imetrum digital image correlation software. The

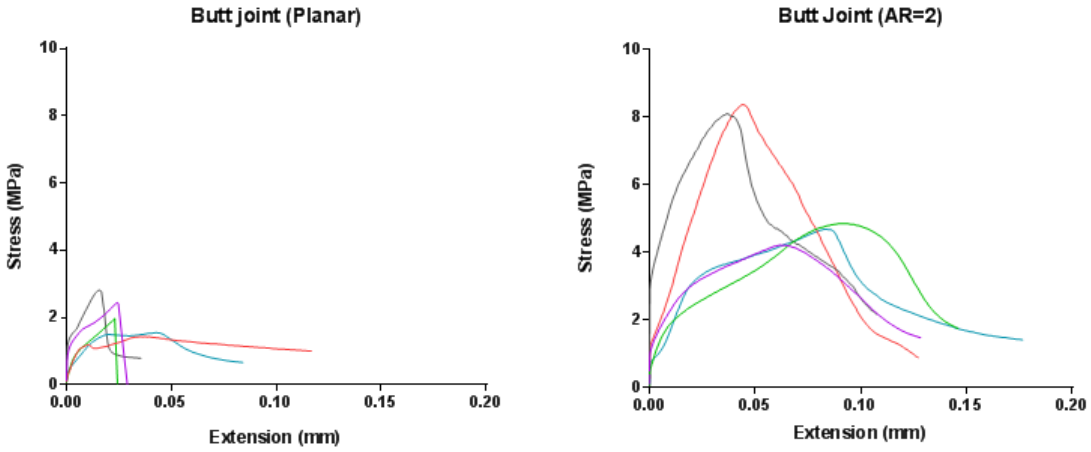

Figure 7-19: Stress-extension data for planar roughened butt joints (left) and structured butt joints (right).

stress-extension data is given in Fig. 7-19. The maximum strain at failure and maximum stress data are summarised within the bar graph plots given in Fig. 7-20 and Fig. 7-21 respectively.

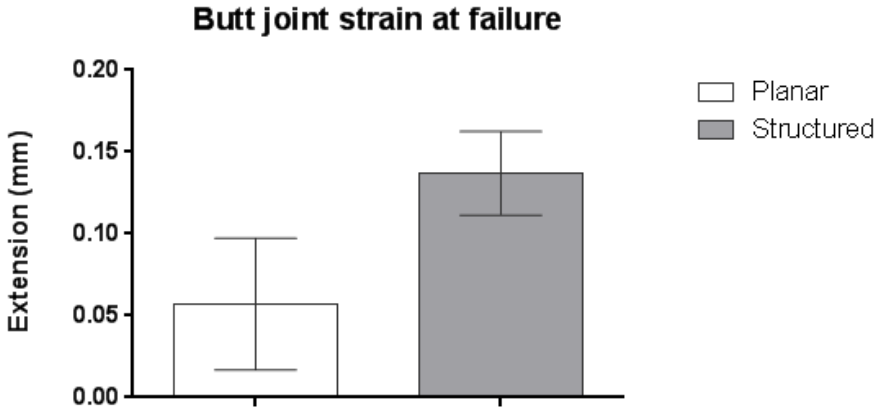

Figure 7-20: Mean strain at failure plots for planar (white) and structured (grey) specimens +/- SD

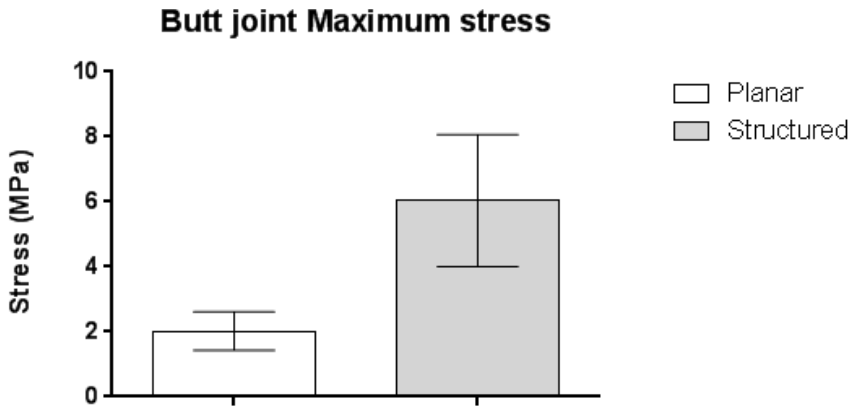

Figure 7-21: Mean maximum stress plots for the planar (white) and structured (grey) specimens +/-SD.

The results reinforce the potential to improve strength and toughness within butt joints utilising interlocked micro-structuring. Average joint strength was increased by approximately 199% and extension at failure was increased by around 140.4%. Images of the failed interfaces for the planar and structured specimens are given in Fig. 7-22. It can be seen from the stress-extension graphs that some tests failed in a gradual manner. It was determined that a small section of adhesive at the edges of the interface remained intact, providing a small degree of load-carrying capacity (around 2-3 MPa). This was observed most predominantly for the lower strength cases, where debonding occurred less

rapidly. This finding is exemplified in the high degree of variability ascribed to strain at failure for the planar joint setup, where some samples had a small load-carrying ability at elevated extension values, whilst others exhibited a rapid failure at much lower extensions. Although, it was concluded that this limitation did not significantly impact on the validity of the results. As can be seen from the photographs, both samples had a cohesive-based failure. This indicates that the role performed via the micro-structuring does not change the state of the eventual interfacial failure.

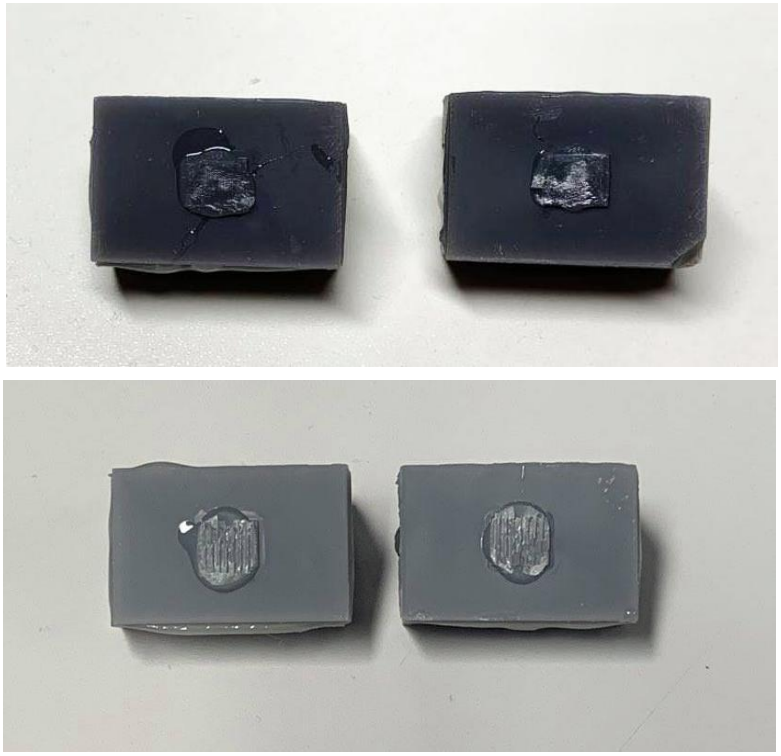

Figure 7-22: Failed interfaces for planar butt joints (top) and micro-structured tests (bottom). Both exhibited a cohesive-based interfacial failure.

The substantial improvements in joint strength can be attributed to a higher active bonding area and the shear resistance introduced on the sides of the features. For each 300 µm wide feature, there is 600 µm of sidewall length available for bonding. The presence of sidewalls for bonding equates to an additional 6 mm of bonding length available, resulting in an active bonding area increase of 120% in the longitudinal direction. This value compares positively with the increase in strength of 178%, suggesting that favourable geometric design is the principal factor in strength improvement. The incorporation of shear-based loading was identified as the secondary mechanism behind greater strength and joint extension. The mixed-mode loading enables a high proportion of loading to occur via shear stress emanating at the interlocked sidewalls as depicted in Fig 7-17. The marked improvement in strength can be accounted for due to the mixed-mode loading response. Since

adhesives are more susceptible to failure under Mode I loading, the introduction of Mode II response within the joint provides a source of partial crack arrestment. This work serves as a proof-of-concept within the area of butt joint testing and reinforces the results of Maloney and Fleck [44,45]. Further work is needed to explore this and other test geometries using mechanical interlocking.

7.5.4: In-situ testing

To gain further insight into the mechanisms underpinning the butt joint response, in-situ testing was utilised to image the micro-features in real-time). The process used for in-situ lap joint imaging was repeated, with the imaging face polished to enable imaging of the bond-line. Polishing was conducted using a Struers LaboSystem mechanical polisher with silicon carbide papers starting with P280 grade and further refining to P600. On account of the larger feature size used, a less refined polished was required than used previously. The images below in Fig. 7-23 represent the interface prior to loading (Fig. 7-23a) and at the onset of failure where the stress within the joint has begun reducing (Fig.7-23b).

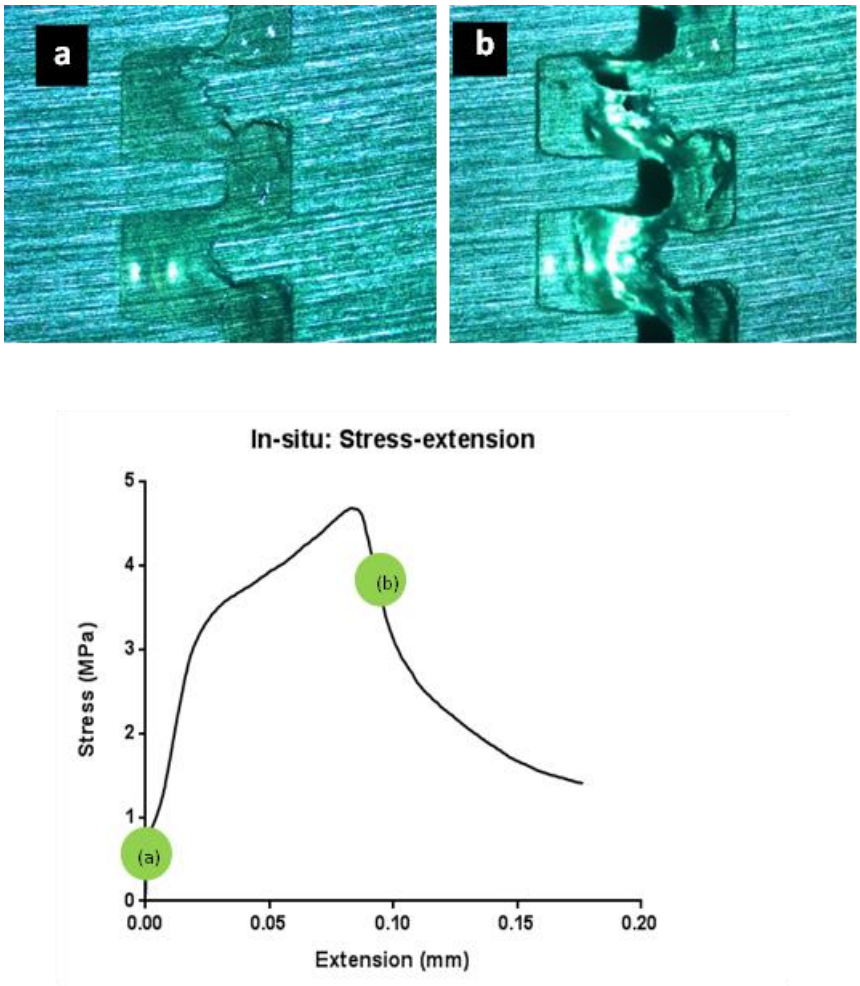

Figure 7-23: In-situ test images and corresponding points on stress-extension curve for structured butt joint test

From the in-situ images, it should be noted that the interlocking depth was not at an ideal depth to maximise strength properties, with the test failing at approximately 4.7 MPa (at the lower end of the strength values recorded for the butt join tests). Other test results using the same test configuration resulted in substantially greater failure stresses on the order of 8 MPa (see Fig 7-19) It appears highly probable that a greater degree of interlocking is the predominant driving factor, leading to a greater surface area subjected to Mode II loading and, thus leading to higher peak stress values. Although, even for the current testing, the inherent increase in active bonding surface area leads to a substantial increase in strength.

7.6: Future improvements and design concepts

This thesis has illustrated the feasibility and advantages of adhesive bonding assisted by mechanical interlocking of micro-structured interfaces. Results have illustrated that the fundamental loading mechanics of the single-lap joint can be altered leading to joint strength being conferred via the adherends with the micro-features resisting load by bending. As was the case with single lap joints, micro-structuring of butt joints also yielded substantial improvements in joint strength and toughness through incorporation of a large proportion of shear loading into the interface. The logical next steps to pursue within this field would be to expand within the field of butt joint testing with several different feature geometries. It is hypothesised that the utilisation of higher aspect ratios will lead to the greatest improvements although further experimentation is needed. Additional in-situ testing would also provide greater insight into the mechanisms underpinning the improvements in strength and toughness. As discussed previously in Chapter 5, there is further scope to study the micro-structured double cantilever beam (DCB) test. The test results obtained for the butt joint, subjected to tensile forces indicate the DCB setup would also benefit from a micro-structured interface with the micro-structuring providing a greater barrier to crack propagation across the bond-line. Another avenue to explore is the fatigue properties of micro-structured joints. This would help explore whether the micro-structuring approach would be viable for safety-critical applications such as the automotive and aerospace industry. It is hypothesised that the micro-structured interface fatigue strength will be intrinsically linked to the adherend material. As seen experimentally, AR = 1 and AR = 2 were the key results with optimal strength and toughness respectively.

Chapter 8 : Conclusions and Future Work

8.1: Concluding remarks

Successful fabrication of micro-structured interfaces has been demonstrated using conventional cleanroom techniques using silicon as the initial adherand material and moving to structured polymer interfaces as the more viable option. Initial testing results for silicon highlighted the need to pursue an alternative testing material whilst retaining silicon as the starting point of the process. After trialling several promising avenues, this project was successful in developing a novel micro-imprinting/injection moulding strategy perfectly suited for the medium/large-scale production of micro-structured polymer surfaces. Geometric fidelity was retained for all samples with results illustrating that the process has excellent lateral resolution (below 20 μm). A key outcome was the ability to injection mould from samples possessing a nanometre scalloped sidewall providing greater flexibility for prospective designs. Although the micro-fabrication work was focussed on obtaining micro-structured adherends, the process that was developed has substantial applications within microfluidics and the MEMS field in general. The viability of the micro-fabrication processes has been demonstrated for a range of engineering materials through employing additional manufacturing processes e.g. injection moulding based production. Injection moulding was conducted primarily using polycarbonate (owing to the excellent mechanical properties), although other polymers such as polystyrene and polypropylene were also moulded illustrating a high degree of flexibility when selecting materials. The work then moved to fabricating lap joints using the structured surfaces. The project has confirmed that interlocking of specimens with micro-scale structuring is possible and consistently achievable at the point of joint assembly. Crucially, the ability to effectively interlock adherends was fine-tuned by experience during the bonding stage and confirmed via optical microscopy. When interlocking the samples, there was a noticeable ability for the features to provide a load-carrying ability even in the absence of adhesive. Interlocking was confirmed through polishing the bond-line using silicon carbide paper and imaging using optical microscopy. The work has also ascertained the implications and potential mechanical benefits associated with micro-structuring of adherends for adhesive bonding relative to un-structured, planar joints. Significant improvements in the strength and work to failure of micro-structured joints have been achieved with experimental results indicating that optimal setups lead to an enhancement of 95.9% and 162% in mechanical strength and work to failure respectively compared to unstructured, roughened joints. Although it was expected that the increase in active bonding area would have a significant positive impact, the mechanical interaction of the features (via bending) was the dominant factor driving improvement.

Through varying key geometrical parameters and in-situ imaging, the experimental work has explained the underlying mechanisms that underpin the results. In-situ testing was performed to determine the loading mechanics within the bond-line. Results for this confirmed the hypothesis that the interlocking features provide most of the resistance, with progressive feature bending responsible for the elevated loads sustained within the structured joint configurations. These results indicate that the mechanical properties of the adherends largely define the mechanical response as opposed to the adhesive properties for conventional, planar joints. Modelling of the structured joints through finite element analysis techniques has been employed to expedite the testing of various microscale geometries. To effectively represent the loading behaviour within the structured joint, a frictional adhesive-less model was implemented for the polycarbonate-polycarbonate interlocking interface. This approach was utilised to capture the feature bending efficiently during the simulations as the typical cohesive zone modelling approach does not account for this mechanism. Results compared well with the experimental results indicating that the frictional model captures the key behaviour of the joint (i.e. mechanical interlocking alone was responsible for the majority of load carrying capacity). This opens up the possibility of adhesive-less joints as long as normal separation can be prevented (perhaps by clamping of the joint). Statistical analyses was conducted using Taguchi analysis and ANOVA analysis to find the relationships for key micro-feature geometry. Results indicate that feature aspect ratios of 1 lead to optimal strength with higher aspect ratios proportional to maximum extension. The work has also studied the viability of using 3D-printing based manufacturing as a route for adherend production to enable the fabrication of structured interfaces as a more cost-effective option for real-world engineering applications. The final chapter highlights the viability of 3D-printing structured joints, providing a more economical alternative to the more expensive micro-fabrication/injection moulding route established previously. A novel test varying feature width was conducted to modify the stress distribution within the joint, with AR = 2 (more compliant) features at the edges and AR = 1 features positioned centrally. Experimental results confirmed that this approach ultimately led to an optimum compromise in strength and toughness between the two aspect ratio results, encouraging a more gradual failure mechanism than the AR = 1 tests.

In summary, a new route to the fabrication of micro-structured surfaces using injection moulding has been developed by pioneering a flexible mould insert produced by adopting a nanoimprint process. The approach is rapid and more versatile. For example, Bosch process produced masters having sidewall scalloping can even be used as the flexibility of the mould insert permits ejection of the part. The approach was then used to successfully fabricate microstructured mechanically interlocking joints in polycarbonate. Mechanical interlocking of adherands was found to produce significant increases in single lap joint strength and work-to-failure. Improvements were also briefly demonstrated for the

tensile loading of butt joints. The load carrying mechanism was found to be predominantly via bending of the interlocked features. 3D printing was then demonstrated as a more rapid and cost-effective approach to fabricating the interlocking joints and includes the possibility of altering feature geometry along the bond-line.

8.2: Future Work

Reflecting on the work, there is scope to extend the research presented to additional areas that were not explored during the research period. Key examples areas that could be explored include:

- **Microfabrication for injection moulding:** A potential area to explore could be the alteration etch and passivation phases of the dry etch process to test various different nanometre scalloping profiles and the overall durability and replication quality obtained during the injection moulding process. Initial results presented in Chapter 4 illustrated a proof of concept with different scalloping profiles leading to an increase in mould insert durability. It is hypothesised that different scallop profiles could yield a smoother separation of the insert/moulded part. Further the incorporation of additional mould release agents could be implemented within the process to further improve the injection moulding from BOSCH process produced silicon masters.
- **Double cantilever beam and double lap joint testing:** The testing work presented in this thesis was limited to 1mm thick polycarbonate specimens on account of the limited tooling depths available for injection moulding. A potential research route could focus on increasing part thicknesses to enable Mode I crack opening tests for micro-structured joints to ascertain the potential improvements in crack resistance conferred by the mixed mode loading imparted by the square wave features. A further testing avenue could utilised double lap joints whereby the eccentric loading profile of the single lap joint would be nullified leading to a substantially greater Mode II driven loading response to fully understand the load transmission capabilities of the square-wave interface.
- **3D printed joints in different materials and spatial tailoring of stiffness:** Within the present work, injection moulded samples in polycarbonate were utilised alongside resin-based 3D printed adherends. Further work extending the material options through the use of LIGA based manufacturing and metal-based 3D printing would be prospective options to test additional materials useful for bonded interfaces in engineering applications. Furthermore, the prospect of tailoring the stiffness of parts as a function of the feature height as well as horizontal distribution across the bond-line would be a promising area to explore, leading to the potential reduction of peak stresses and the alteration of load transmission within the joint.

References

[1] D. Olsen, “History Of Metal Casting,” 2020. https://www.metaltek.com/blog/history-of-metal-casting/ (accessed Feb. 14, 2020).

[2] “History of the development of iron-carbon diagrams,” *Met. Sci. Heat Treat.*, vol. 10, pp. 344–350, 1968.

[3] “Injection Moulding History & Facts,” 2021. http://www.avplastics.co.uk/njection-moulding-history (accessed Mar. 04, 2021).

[4] G. G. Fuentes, *In Micro and Nano Technologies, Micromanufacturing Engineering and Technology*, Second edi. William Andrew Publishing, 2015.

[5] A. la Monaca *et al.*, “Surface integrity in metal machining - Part II: Functional performance,” *Int. J. Mach. Tools Manuf.*, vol. 164, no. December 2020, p. 103718, 2021, doi: 10.1016/j.ijmachtools.2021.103718.

[6] S. Bin Jaber, A. Hamilton, Y. Xu, M. E. Kartal, N. Gadegaard, and D. M. Mulvihill, “Friction of flat and micropatterned interfaces with nanoscale roughness,” *Tribol. Int.*, vol. 153, no. July 2020, p. 106563, 2021, doi: 10.1016/j.triboint.2020.106563.

[7] N. Yamada, T. Ijiro, E. Okamoto, K. Hayashi, and H. Masuda, “Characterization of antireflection moth-eye film on crystalline silicon photovoltaic module,” *Opt. Express*, vol. 19, no. S2, p. A118, 2011, doi: 10.1364/oe.19.00a118.

[8] R. Brunner, O. Sandfuchs, C. Pacholski, C. Morhard, and J. Spatz, “Lessons from nature: Biomimetic subwavelength structures for high-performance optics,” *Laser Photonics Rev.*, vol. 6, no. 5, pp. 641–659, 2012, doi: 10.1002/lpor.201100011.

[9] H. J. Ensikat, P. Ditsche-kuru, C. Neinhuis, and W. Barthlott, “Superhydrophobicity in perfection : the outstanding properties of the lotus leaf,” pp. 152–161, 2011, doi: 10.3762/bjnano.2.19.

[10] -Jooyoun Kim *et al.*, “Effects of micro- and nano-structures on the self- cleaning behaviour of lotus leaves Exploring Factors for Uniformly Distributing Liquid Droplets in a Bifurcation Tree Microfluidic Chip Pin- Effects of micro-and nano-structures on the self-cleaning behaviour of lotus leaves,” 2006, doi: 10.1088/0957-4484/17/5/032.

[11] T. Sullivan and F. Regan, “The characterization, replication and testing of dermal denticles of

Scyliorhinus canicula for physical mechanisms of biofouling prevention," *Bioinspiration and Biomimetics*, vol. 6, no. 4, 2011, doi: 10.1088/1748-3182/6/4/046001.

[12] Y. Liu and G. Li, "A new method for producing 'Lotus Effect' on a biomimetic shark skin," *J. Colloid Interface Sci.*, vol. 388, no. 1, pp. 235–242, 2012, doi: 10.1016/j.jcis.2012.08.033.

[13] H. Gao, X. Wang, H. Yao, S. Gorb, and E. Arzt, "Mechanics of hierarchical adhesion structures of geckos," *Mech. Mater.* , vol. 37, pp. 275–285, 2005, doi: 10.1016/j.mechmat.2004.03.008.

[14] A. K. Geim, S. V. Dubonos, I. V. Grigorieva, K. S. Novoselov, A. A. Zhukov, and S. Y. Shapoval, "Microfabricated adhesive mimicking gecko foot-hair," *Nat. Mater.*, vol. 2, no. 7, pp. 461–463, 2003, doi: 10.1038/nmat917.

[15] W. C. Wake, "Adhesion and adhesives: Science and technology A. J. Kinloch, Chapman and Hall, London, 1987. pp. xii + 441, price £35.00. ISBN 0-412-27440-X," *Br. Polym. J.*, vol. 20, no. 3, pp. 300–300, Jan. 1988, doi: 10.1002/pi.4980200326.

[16] G. Michalos, S. Makris, N. Papakostas, D. Mourtzis, and G. Chryssolouris, "Automotive assembly technologies review: challenges and outlook for a flexible and adaptive approach," *CIRP J. Manuf. Sci. Technol.*, vol. 2, no. 2, pp. 81–91, Jan. 2010, doi: 10.1016/J.CIRPJ.2009.12.001.

[17] A. Higgins, "Adhesive bonding of aircraft structures," *Int. J. Adhes. Adhes.*, vol. 20, no. 5, pp. 367–376, 2000, doi: 10.1016/S0143-7496(00)00006-3.

[18] Lucas F M Silva, A.Öchsner, and D. A. Robert, *Handbook od Adhesion Technology*, vol. 53, no. 9. 2011. doi: 10.1017/CBO9781107415324.004.

[19] M. H. Pahoja, "AD-753 469 STRESS ANALYSIS OF AN ADHESIVE LAP JOINT SUBJECTED TO TENSION, SHEAR FORCE AND BENDING MOMENTS," 1972.

[20] L. F. M da Silva, R. J. C Carbas, G. W. Critchlow, M. A. V Figueiredo, and K. Brown, "Effect of material, geometry, surface treatment and environment on the shear strength of single lap joints", [Online]. Available: http://creativecommons.org/licenses/by-nc-nd/2.5/

[21] S. Ebnesajjad, *Material Surface Preparation Techniques*. 2014. doi: 10.1016/b978-0-323-26435-8.00006-x.

[22] A. C. Marques *et al.*, "Review on adhesives and surface treatments for structural applications: Recent developments on sustainability and implementation for metal and composite substrates," *Materials (Basel).*, vol. 13, no. 24, pp. 1–43, 2020, doi: 10.3390/ma13245590.

[23] P. Fabbri and M. Messori, “Surface Modification of Polymers: Chemical, Physical, and Biological Routes,” *Modif. Polym. Prop.*, pp. 109–130, 2017, doi: 10.1016/B978-0-323-44353-1.00005-1.

[24] S. Kitova, M. Minchev, G. Danev, and B. Academy, “Rf plasma treatment of polycarbonate substrates,” *J. Optoelectron. Adv. Mater.*, vol. 7, no. 5, pp. 2607–2612.

[25] N. V Bhat and D. J. Upadhyay, “Plasma-Induced Surface Modification and Adhesion Enhancement of Polypropylene Surface,” *J. Appl. Polym. Sci.*, vol. 86, no. 4, pp. 925–936, doi: 10.1002/app.11024.

[26] J. Comyn, L. Mascia, G. Xiao, I. E, and B. M. Parker, “Corona-discharge treatment of polyetheretherketone (PEEK) for adhesive bonding,” *Int. J. Adhes. Adhes.*, vol. 16, no. 4, pp. 301–304, 1996.

[27] G. Singh and A. Verma, “A Brief Review on injection moulding manufacturing process,” *Mater. Today Proc.*, vol. 4, no. 2, pp. 1423–1433, 2017, doi: 10.1016/j.matpr.2017.01.164.

[28] J. . J. L. Sanders, “On the Griffith-Irwin Fracture Theory,” *J. Appl. Mech.*, vol. 27, no. 2, pp. 3352–353, 1960.

[29] C. T. Sun and Z.-H. Jin, “Griffith Theory of Fracture,” *Fract. Mech.*, pp. 11–24, 2012, doi: 10.1016/b978-0-12-385001-0.00002-x.

[30] M. J. Mullins, D. Liu, and H.-J. Sue, “Mechanical properties of thermosets,” *Thermosets*, pp. 28–61, 2012, doi: 10.1533/9780857097637.1.28.

[31] L. F. M. Da Silva, R. F. T. Lima, R. M. S. Teixeira, and A. Puga, “Closed-form solutions for adhesively bonded joints”.

[32] O. Volkersen, “Die Niektraftverteiling in Zugbeanspruchten mit Konstanten Laschenquerschritten.,” *Luftfahrtforschung*, vol. 15, pp. 41–47, 1938.

[33] R. Q. Rodríguez, P. Sollero, and M. B. Rodrigues, “Stress analysis and failure criteria of adhesive bonded single lap joints,” *21st Int. Congr. Mech. Eng.*, pp. 1–9, 2011.

[34] E. Goland, M. and Reissner, ““The stresses in cemented joints,” *J. Appl. Mech.*, vol. 11, pp. A17–A27., 1944, Accessed: May 03, 2018. [Online]. Available: http://www.abcm.org.br/anais/cobem/2011/PDF/191001.pdf

[35] L. J. Hart-Smith, “Adhesive-Bonded Double-Lap Joints,” p. 114, 1973, doi: NAS1-11234.

[36] L. F. M. da Silva and R. D. S. G. Campilho, *Advances in Numerical Modeling of Adhesive Joints*. 2012. doi: 10.1007/978-3-642-23608-2.

[37] T. Diehl, “Modeling Surface-Bonded Structures with ABAQUS Cohesive Elements : Beam-Type Solutions,” *2004 ABAQUS Users’ Conf.*, pp. 1–27, 2004.

[38] X. M. Zhang, T. M. Yue, and H. C. Man, “Enhancement of ceramic-to-metal adhesive bonding by excimer laser surface treatment,” *Mater. Lett.*, vol. 30, no. April, pp. 327–332, 1997.

[39] E. G. Baburaj, D. Starikov, J. Evans, G. A. Shafeev, and A. Bensaoula, “Enhancement of adhesive joint strength by laser surface modification,” *Int. J. Adhes. Adhes.*, vol. 27, no. 4, pp. 268–276, 2007, doi: 10.1016/j.ijadhadh.2006.05.004.

[40] M. Alfano *et al.*, “Surface Patterning of Metal Substrates Through Low Power Laser Ablation for Enhanced Adhesive Bonding,” *J. Adhes.*, vol. 90, no. 5–6, pp. 384–400, 2014, doi: 10.1080/00218464.2013.871538.

[41] E. Hernandez, M. Alfano, G. Lubineau, and U. Buttner, “Improving adhesion of copper/epoxy joints by pulsed laser ablation,” *Int. J. Adhes. Adhes.*, 2016, doi: 10.1016/j.ijadhadh.2015.10.003.

[42] J. Byskov-Nielsen and P. Balling, “Laser structuring of metal surfaces: Micro-mechanical interlocking,” *Appl. Surf. Sci.*, 2009, doi: 10.1016/j.apsusc.2008.07.118.

[43] F. A. Cordisco, P. D. Zavattieri, L. G. Hector, and B. E. Carlson, “Mode i fracture along adhesively bonded sinusoidal interfaces,” *Int. J. Solids Struct.*, vol. 83, pp. 45–64, 2016, doi: 10.1016/j.ijsolstr.2015.12.028.

[44] K. Maloney and N. Fleck, “Damage tolerance of an architected adhesive joint,” *Int. J. Solids Struct.*, vol. 1, no. 0, pp. 1–11, 2017, doi: 10.1016/j.ijsolstr.2017.06.010.

[45] K. Maloney and N. Fleck, “Tear resistance of a square-wave joint: Experiment versus cohesive zone model,” *Int. J. Adhes. Adhes.*, vol. 84, pp. 9–17, 2018, doi: 10.1016/j.ijadhadh.2018.02.008.

[46] M. C. Corbett, P. A. Sharos, M. Hardiman, and C. T. McCarthy, “Numerical design and multi-objective optimisation of novel adhesively bonded joints employing interlocking surface morphology,” *Int. J. Adhes. Adhes.*, vol. 78, pp. 111–120, 2017, doi: 10.1016/j.ijadhadh.2017.06.002.

[47] M. O’Brien, D. J. Mortell, M. C. Corbett, R. M. O’Higgins, and C. T. McCarthy, “Mechanical

performance and failure behaviour of miniature aluminium joints with novel interlocking reinforcement," *Int. J. Adhes. Adhes.*, vol. 95, no. August, 2019, doi: 10.1016/j.ijadhadh.2019.102431.

[48] B. Haghpanah, S. Chiu, and A. Vaziri, "Adhesively bonded lap joints with extreme interface geometry," *Int. J. Adhes. Adhes.*, vol. 48, pp. 130–138, 2014, doi: 10.1016/j.ijadhadh.2013.09.041.

[49] E. D. Reedy *et al.*, "Effect of Nanoscale Patterned Interfacial Roughness on Interfacial Toughness," 2007. [Online]. Available: http://infoserve.sandia.gov/sand_doc/2007/075990.pdf

[50] W. S. Kim, I. H. Yun, J. J. Lee, and H. T. Jung, "Evaluation of mechanical interlock effect on adhesion strength of polymermetal interfaces using micro-patterned surface topography," *Int. J. Adhes. Adhes.*, 2010, doi: 10.1016/j.ijadhadh.2010.05.004.

[51] R. MATSUZAKI and T. SUZUKI, "Surface Modification by Nanoimprint Lithography for Improvement of the Joint Strength of Composites," *J. Solid Mech. Mater. Eng.*, vol. 4, no. 7, pp. 963–973, 2010, doi: 10.1299/jmmp.4.963.

[52] Y. Hikosaka, R. Matsuzaki, A. Todoroki, and Y. Mizutani, "Enhancement of interfacial fracture toughness of carbon/epoxy composite adhesive joints by in-mold surface preparation," *Express Polym. Lett.*, vol. 7, no. 3, pp. 293–303, 2012, doi: 10.3144/expresspolymlett.2013.26.

[53] R. Matsuzaki, N. Tsukamoto, and J. Taniguchi, "Mechanical interlocking by imprinting of undercut micropatterns for improving adhesive strength of polypropylene," *Int. J. Adhes. Adhes.*, vol. 68, pp. 124–132, 2016, doi: 10.1016/j.ijadhadh.2016.03.002.

[54] S. Franssila, *Introduction to Microfabrication*. J. Wiley, 2010. doi: 10.1002/9781119990413.

[55] D. H. Lee and N. G. Cho, "Assessment of surface profile data acquired by a stylus profilometer," *Meas. Sci. Technol.*, vol. 23, no. 10, 2012, doi: 10.1088/0957-0233/23/10/105601.

[56] G. T. Smith, *Industrial Metrology: Surfaces and Roundness*. London: Springer, 2002.

[57] R. Leach, *Optical Measurement of Surfacte Topography*.

[58] M. Omidi *et al.*, "Characterization of biomaterials," *Biomater. Oral Dent. Tissue Eng.*, pp. 97–115, 2017, doi: 10.1016/B978-0-08-100961-1.00007-4.

[59] S. Sturm and B. Jančar, "Microstructure Characterization of Advanced Ceramics," *Adv. Ceram.*

Dent., pp. 151–172, 2014, doi: 10.1016/B978-0-12-394619-5.00008-0.

[60] M. K. Hooda, M. Wadhwa, S. Verma, M. M. Nayak, P. J. George, and A. K. Paul, "A systematic study of DRIE process for high aspect ratio microstructuring," *Vacuum*, vol. 84, no. 9, pp. 1142–1148, 2010, doi: 10.1016/j.vacuum.2010.01.052.

[61] F. Laermer, S. Franssila, L. Sainiemi, and K. Kolari, *Deep Reactive Ion Etching*, Second Edi. William Andrew Publishing, 2015. doi: 10.1016/B978-0-323-29965-7.00021-X.

[62] "SU-8: Thick Photo-Resist for MEMS," 2020. https://memscyclopedia.org/su8.html (accessed Aug. 16, 2020).

[63] H. Lorenz, M. Despont, N. Fahrni, J. Brugger, P. Vettiger, and P. Renaud, "High-aspect-ratio, ultrathick, negative-tone near-UV photoresist and its applications for MEMS," *Sensors Actuators, A Phys.*, vol. 64, no. 1, pp. 33–39, 1998, doi: 10.1016/S0924-4247(98)80055-1.

[64] P. Rezai, W.-I. Wu, and P. R. Selvaganapathy, "Microfabrication of polymers for bioMEMS," *MEMS Biomed. Appl.*, pp. 3–45, 2012, doi: 10.1533/9780857096272.1.3.

[65] W. G. Frizelle, *10 Injection Molding Technology*, Second Edi. Elsevier Inc., 1968. doi: 10.1016/B978-0-323-39040-8/00010-9.

[66] N. Gadegaard, S. Mosler, and N. B. Larsen, "Biomimetic polymer nanostructures by injection molding," *Macromol. Mater. Eng.*, vol. 288, no. 1, pp. 76–83, 2003, doi: 10.1002/mame.200290037.

[67] M. Matschuk and N. B. Larsen, "Injection molding of high aspect ratio sub-100 nm nanostructures," *J. Micromechanics Microengineering*, vol. 23, no. 2, 2013, doi: 10.1088/0960-1317/23/2/025003.

[68] S. Yoon, C. Srirojpinyo, J. S. Lee, J. L. Mead, S. Matsui, and C. M. F. Barry, "Evaluation of novel tooling for nanoscale injection molding," *Smart Struct. Mater. 2005 Smart Electron. MEMS, BioMEMS, Nanotechnol.*, vol. 5763, no. May 2005, p. 107, 2005, doi: 10.1117/12.599959.

[69] J. Zhao *et al.*, "Development of rapid manufacturing technology of polymer microfluidic devices by micro moulding using silicon mould inserts," *Proc. 6th Int. Conf. Nanochannels, Microchannels, Minichannels, ICNMM2008*, no. PART B, pp. 1187–1194, 2008, doi: 10.1115/ICNMM2008-62232.

[70] S. H. Yoon, P. Palanisamy, P. Padmanabha, J. L. Mead, and C. M. F. Barry, "Comparison of tooling materials in injection molding of microscale features," *ASME Int. Mech. Eng. Congr.*

Expo. Proc., vol. 12, no. PART A, pp. 745–752, 2010, doi: 10.1115/IMECE2009-13346.

[71] T. S. Hansen, D. Selmeczi, and N. B. Larsen, "Fast prototyping of injection molded polymer microfluidic chips," *J. Micromechanics Microengineering*, vol. 20, no. 1, 2010, doi: 10.1088/0960-1317/20/1/015020.

[72] S. H. Park, W. I. Lee, S. N. Moon, Y. E. Yoo, and Y. H. Cho, "Injection molding micro patterns with high aspect ratio using a polymeric flexible stamper," *Express Polym. Lett.*, vol. 5, no. 11, pp. 950–958, 2011, doi: 10.3144/expresspolymlett.2011.93.

[73] N. Zhang, C. J. Byrne, D. J. Browne, and M. D. Gilchrist, "Towards nano-injection molding," *Mater. Today*, vol. 15, no. 5, pp. 216–221, 2012, doi: 10.1016/S1369-7021(12)70092-5.

[74] J. M. Stormonth-Darling and N. Gadegaard, "Injection moulding difficult nanopatterns with hybrid polymer inlays," *Macromol. Mater. Eng.*, vol. 297, no. 11, pp. 1075–1080, 2012, doi: 10.1002/mame.201100397.

[75] I. Mochi, K. A. Goldberg, B. La Fontaine, A. Tchikoulaeva, and C. Holfeld, "Proceedings of SPIE," *Extrem. Ultrav. Lithogr.*, no. September 1996, pp. 76361A-76361A–9, 2021, doi: 10.1117/12.251203.

[76] R. Greener, J. and Wimberger-Friedl, *Precision Injection Molding: Process, Material, and Applications*. Munich: Carl Hanser Verlag, 2006.

[77] C. K. Huang, "Polymeric nanofeatures of 100 nm using injection moulding for replication," *J. Micromechanics Microengineering*, vol. 17, no. 8, pp. 1518–1526, 2007, doi: 10.1088/0960-1317/17/8/014.

[78] K. Mnkknen *et al.*, "Replication of sub-micron features using amorphous thermoplastics," *Polym. Eng. Sci.*, vol. 42, no. 7, pp. 1600–1608, 2002, doi: 10.1002/pen.11055.

[79] H. Schift *et al.*, "Nanoreplication in polymers using hot embossing and injection molding," *Microelectron. Eng.*, vol. 53, no. 1, pp. 171–174, 2000, doi: 10.1016/S0167-9317(00)00289-6.

[80] M. Yoshii, H. Kuramoto, and Y. Ochiai, "Experimental study of the transcription of minute width grooves by injection molding (II)," *Polym. Eng. Sci.*, vol. 38, no. 9, pp. 1587–1593, 1998, doi: 10.1002/pen.10329.

[81] D. Masato, M. Sorgato, and G. Lucchetta, "Analysis of the influence of part thickness on the replication of micro-structured surfaces by injection molding," *Mater. Des.*, vol. 95, pp. 219–224, 2016, doi: 10.1016/j.matdes.2016.01.115.

[82] A. C. Liou and R. H. Chen, “Injection molding of polymer micro- and sub-micron structures with high-aspect ratios,” *Int. J. Adv. Manuf. Technol.*, vol. 28, no. 11–12, pp. 1097–1103, 2006, doi: 10.1007/s00170-004-2455-2.

[83] A. K. Holthusen, O. Riemer, J. Schmütz, and A. Meier, “Mold machining and injection molding of diffractive microstructures,” *J. Manuf. Process.*, vol. 26, pp. 290–294, 2017, doi: 10.1016/j.jmapro.2017.02.014.

[84] C. A. Griffiths, S. S. Dimov, S. G. Scholz, G. Tosello, and A. Rees, “Influence of injection and cavity pressure on the demoulding force in micro-injection moulding,” *J. Manuf. Sci. Eng. Trans. ASME*, vol. 136, no. 3, 2014, doi: 10.1115/1.4026983.

[85] V. Bellantone, R. Surace, G. Trotta, and I. Fassi, “Replication capability of micro injection moulding process for polymeric parts manufacturing,” *Int. J. Adv. Manuf. Technol.*, vol. 67, no. 5–8, pp. 1407–1421, 2013, doi: 10.1007/s00170-012-4577-2.

[86] Y. Zhang, H. N. Hansen, and S. Sørensen, “Replication of micro-pillars by PEEK injection moulding with CrN-coated Ni tool,” *Int. J. Adv. Manuf. Technol.*, vol. 80, no. 1–4, pp. 383–388, 2015, doi: 10.1007/s00170-015-6991-8.

[87] C. A. Griffiths *et al.*, “Investigation of polymer inserts as prototyping tooling for micro injection moulding,” *Int. J. Adv. Manuf. Technol.*, vol. 47, no. 1–4, pp. 111–123, 2010, doi: 10.1007/s00170-009-2038-3.

[88] S. D. Moon, N. Lee, and S. Kang, “Fabrication of a microlens array using micro-compression molding with an electroformed mold insert,” *J. Micromechanics Microengineering*, vol. 13, no. 1, pp. 98–103, 2003, doi: 10.1088/0960-1317/13/1/314.

[89] Y. C. Su, J. Shah, and L. Lin, “Implementation and analysis of polymeric microstructure replication by micro injection molding,” *J. Micromechanics Microengineering*, vol. 14, no. 3, pp. 415–422, 2004, doi: 10.1088/0960-1317/14/3/015.

[90] J. M. Stormonth-Darling, R. H. Pedersen, C. How, and N. Gadegaard, “Injection moulding of ultra high aspect ratio nanostructures using coated polymer tooling,” *J. Micromechanics Microengineering*, vol. 24, no. 7, 2014, doi: 10.1088/0960-1317/24/7/075019.

[91] H. N. Hansen, R. J. Hocken, and G. Tosello, “Replication of micro and nano surface geometries,” *CIRP Ann. - Manuf. Technol.*, vol. 60, no. 2, pp. 695–714, 2011, doi: 10.1016/j.cirp.2011.05.008.

[92] N. Zhang *et al.*, “Manufacturing microstructured tool inserts for the production of polymeric

microfluidic devices," *J. Micromechanics Microengineering*, vol. 25, no. 9, 2015, doi: 10.1088/0960-1317/25/9/095005.

[93] J. Giboz, T. Copponnex, and P. Mélé, "Microinjection molding of thermoplastic polymers: A review," *J. Micromechanics Microengineering*, vol. 17, no. 6, 2007, doi: 10.1088/0960-1317/17/6/R02.

[94] M. D. Henry, "Icp Etching of Silicon for Micro and Nanoscale Devices," *Caltech*, p. 219, 2010, [Online]. Available: http://resolver.caltech.edu/CaltechTHESIS:05262010-152815609

[95] J. Steigert *et al.*, "Rapid prototyping of microfluidic chips in COC," *J. Micromechanics Microengineering*, vol. 17, no. 2, pp. 333–341, 2007, doi: 10.1088/0960-1317/17/2/020.

[96] J. C. Mcdonald, D. C. Duffy, J. R. Anderson, and D. T. Chiu, "Review General Fabrication of microfluidic systems in poly (dimethylsiloxane)," *Electrophoresis*, vol. 21, no. 1, pp. 27–40, 2000, [Online]. Available: http://www.ncbi.nlm.nih.gov/pubmed/10634468

[97] P. Kim, K. W. Kwon, M. C. Park, S. H. Lee, S. M. Kim, and K. Y. Suh, "Soft lithography for microfluidics: A Review," *Biochip J.*, vol. 2, no. 1, pp. 1–11, 2008.

[98] P. J. Hung, P. J. Lee, P. Sabounchi, N. Aghdam, R. Lin, and L. P. Lee, "A novel high aspect ratio microfluidic design to provide a stable and uniform microenvironment for cell growth in a high throughput mammalian cell culture array," *Lab Chip*, vol. 5, no. 1, pp. 44–48, 2005, doi: 10.1039/b410743h.

[99] N. Palina, T. Mueller, S. Mohanti, and A. G. Aberle, "LASER ASSISTED BORON DOPING OF SILICON WAFER SOLAR CELLS USING NANOSECOND AND PICOSECOND LASER PULSES," *2011 37th IEEE Photovolt. Spec. Conf.*, pp. 2193–2197, 2011, doi: 10.1109/PVSC.2011.6186392.

[100] "Araldite rapid datasheet: Hunstaman advanced materials," 2011.

[101] W. H. P. and W. F. Ranson, "Digital imaging techniques in experimental stress analysis," *Opt. Eng.*, vol. 21, no. 3, pp. 427–431, 1982.

[102] M. Sebastiani, C. Eberl, E. Bemporad, and G. M. Pharr, "Depth-resolved residual stress analysis of thin coatings by a new FIB-DIC method," *Mater. Sci. Eng. A*, vol. 528, no. 27, pp. 7901–7908, 2011, doi: 10.1016/j.msea.2011.07.001.

[103] T. Sadowski and M. Knec, "Application of DIC technique for monitoring of deformation process of SPR hybrid joints," *Arch. Metall. Mater.*, vol. 58, no. 1, pp. 119–125, 2013, doi: 10.2478/v10172-012-0161-x.

[104] P. Sztefek, M. Vanleene, R. Olsson, R. Collinson, A. A. Pitsillides, and S. Shefelbine, “Using digital image correlation to determine bone surface strains during loading and after adaptation of the mouse tibia,” *J. Biomech.*, vol. 43, no. 4, pp. 599–605, 2010, doi: 10.1016/j.jbiomech.2009.10.042.

[105] N. McCormick and J. Lord, “Digital image correlation,” *Mater. Today*, vol. 13, no. 12, pp. 52–54, 2010, doi: 10.1016/S1369-7021(10)70235-2.

[106] M. Tekieli, S. De Santis, G. de Felice, A. Kwiecień, and F. Roscini, “Application of Digital Image Correlation to composite reinforcements testing,” *Compos. Struct.*, vol. 160, pp. 670–688, 2017, doi: 10.1016/j.compstruct.2016.10.096.

[107] S. Roy *et al.*, “Plastic Deformation of Steel Plates under High Impact Loading,” 2013.

[108] A. Sethuramiah and R. Kumar, *Statistics and Experimental Design in Perspective*. 2016. doi: 10.1016/b978-0-12-804533-6.00006-8.

[109] J. A. Ghani, I. A. Choudhury, and H. H. Hassan, “Application of Taguchi method in the optimization of end milling parameters,” *J. Mater. Process. Technol.*, vol. 145, no. 1, pp. 84–92, 2004, doi: 10.1016/S0924-0136(03)00865-3.

[110] K. S. Taguchi G, *Orthogonal arrays and linear graphs: tools for quality engineering*. American Supplier Institute, Allen Park, 1987.

[111] E. E. and H. T. Taguchi G, *Quality Engineering in Production Systems*. McGraw-Hill College, 1989.

[112] J. S. Chohan, R. Singh, K. S. Boparai, R. Penna, and F. Fraternali, “Dimensional accuracy analysis of coupled fused deposition modeling and vapour smoothing operations for biomedical applications,” *Compos. Part B Eng.*, vol. 117, pp. 138–149, 2017, doi: 10.1016/j.compositesb.2017.02.045.

[113] S. R. Rao and G. Padmanabhan, “Application of Taguchi methods and ANOVA in optimization of process parameters for metal removal rate in electrochemical machining of Al/5% SiC composites,” *Int. J. Eng. Res. …*, vol. 2, no. 3, pp. 192–197, 2012, [Online]. Available: http://scholar.google.com/scholar?hl=en&btnG=Search&q=intitle:Application+of+Taguchi+methods+and+ANOVA+in+optimization+of+process+parameters+for+metal+removal+rate+in+electrochemical+machining+of+Al+/+5+%25+SiC+composites#0

[114] L. S. Y. Wen, S. Xun, M. Haoye, S. Baichuan, C. Peng, L. Xuejian, Z. Kaihong, Y. Xuan, P. Jiang, “3D printed porous ceramic scaffolds for bone tissue engineering: a review,” *Biomater. Sci.*,

vol. 5, no. 9, pp. 1690–1698, 2017.

[115] J. W. Stansbury and M. J. Idacavage, “3D printing with polymers: Challenges among expanding options and opportunities,” *Dent. Mater.*, vol. 32, no. 1, pp. 54–64, 2016, doi: 10.1016/j.dental.2015.09.018.

[116] T. D. Ngo, A. Kashani, G. Imbalzano, K. T. Q. Nguyen, and D. Hui, “Additive manufacturing (3D printing): A review of materials, methods, applications and challenges,” *Compos. Part B Eng.*, vol. 143, no. February, pp. 172–196, 2018, doi: 10.1016/j.compositesb.2018.02.012.

[117] A. K. Sood, R. K. Ohdar, and S. S. Mahapatra, “Parametric appraisal of mechanical property of fused deposition modelling processed parts,” *Mater. Des.*, vol. 31, no. 1, pp. 287–295, 2010, doi: 10.1016/j.matdes.2009.06.016.

[118] O. A. Mohamed, S. H. Masood, and J. L. Bhowmik, “Optimization of fused deposition modeling process parameters: a review of current research and future prospects,” *Adv. Manuf.*, vol. 3, no. 1, pp. 42–53, 2015, doi: 10.1007/s40436-014-0097-7.

[119] P. Parandoush and D. Lin, “A review on additive manufacturing of polymer-fiber composites,” *Compos. Struct.*, vol. 182, pp. 36–53, 2017, doi: 10.1016/j.compstruct.2017.08.088.

[120] X. Wang, M. Jiang, Z. Zhou, J. Gou, and D. Hui, “3D printing of polymer matrix composites: A review and prospective,” *Compos. Part B Eng.*, vol. 110, pp. 442–458, 2017, doi: 10.1016/j.compositesb.2016.11.034.

[121] B. Utela, D. Storti, R. Anderson, and M. Ganter, “A review of process development steps for new material systems in three dimensional printing (3DP),” *J. Manuf. Process.*, vol. 10, no. 2, pp. 96–104, 2008, doi: 10.1016/j.jmapro.2009.03.002.

[122] C. Y. Yap *et al.*, “Review of selective laser melting: Materials and applications,” *Appl. Phys. Rev.*, vol. 2, no. 4, 2015, doi: 10.1063/1.4935926.

[123] H. Lee, C. H. J. Lim, M. J. Low, N. Tham, V. M. Murukeshan, and Y. J. Kim, “Lasers in additive manufacturing: A review,” *Int. J. Precis. Eng. Manuf. - Green Technol.*, vol. 4, no. 3, pp. 307–322, 2017, doi: 10.1007/s40684-017-0037-7.

[124] F. P. W. Melchels, J. Feijen, and D. W. Grijpma, “A review on stereolithography and its applications in biomedical engineering,” *Biomaterials*, vol. 31, no. 24, pp. 6121–6130, 2010, doi: 10.1016/j.biomaterials.2010.04.050.

[125] A. Bagheri and J. Jin, “Photopolymerization in 3D Printing,” *ACS Appl. Polym. Mater.*, vol. 1,

no. 4, pp. 593–611, 2019, doi: 10.1021/acsapm.8b00165.

[126] J. Z. Manapat, Q. Chen, P. Ye, and R. C. Advincula, “3D Printing of Polymer Nanocomposites via Stereolithography,” *Macromol. Mater. Eng.*, vol. 302, no. 9, pp. 1–13, 2017, doi: 10.1002/mame.201600553.

[127] “Formlabs: SLA printer guide,” 2022. https://formlabs.com/uk/blog/ultimate-guide-to-stereolithography-sla-3d-printing/ (accessed Jul. 01, 2022).

[128] “Formlabs Grey pro resin datasheet.” https://formlabs-media.formlabs.com/datasheets/Grey_Pro_Technical.pdf